In Vivo Assessment of Metabotropic Glutamate Receptor Type 5 Abnormalities in Patients with Focal Cortical Dysplasia

Jonathan DuBois

Integrated Program in Neuroscience

McGill University, Montreal

July, 2017

A thesis submitted to McGill University in partial fulfillment of the requirements of the degree of Doctor of Philosophy

Table of contents

Abstract

Rationale: Focal cortical dysplasia (FCD) is a malformation of cortical development, which is characterized histologically by cortical dyslamination and the presence of dysmorphic neurons, including balloon cells. Metabotropic glutamate receptor type 5 (mGluR5) is a postsynaptic G-protein coupled receptor that modulates neuronal excitability and plays a key role in cortical development. In addition to several lines of evidence that support a role of mGluR5 in epileptogenesis, surgical specimens resected from patients with FCD show mGluR5 abnormalities in dysmorphic neurons and balloon cells. However, it is unknown whether mGluR5 abnormalities could be a diffuse cortical characteristic of patients with FCD or limited within the boundaries of the epileptogenic lesion.

Methods: In order to characterize whole-brain mGluR5 abnormalities in patients with FCD, we utilized the positron emission tomography (PET) ligand [^{11}C]ABP688, which binds selectively to the mGluR5 allosteric site. In addition, we developed a surface-based analysis and data-driven partial volume correction method to ensure accurate comparisons between the FCD lesion and healthy control cortex. Using these methods, we carried out the following projects: 1) Evaluation of regional differences related to mGluR5 availability in healthy controls; 2) Assessment of *in vivo* mGluR5 abnormalities in patients with FCD; 3) Characterization of the mGluR5 network in patients with FCD.

Results: In study 1, we observed a heterogeneous distribution of mGluR5 availability across cortical and subcortical structures, with the highest binding in

association cortices. In addition, we found that mGluR5 availability was stable across the healthy adult lifespan and between sexes. In study 2, we demonstrated that mGluR5 availability was reduced within the MRI positive dysplastic lesion. In the majority of patients, mGluR5 abnormalities were also found in perilesional and remote areas of the cortex. In study 3, patients with FCD showed reduced mGluR5 network efficiency and resilience in both the ipsilateral and contralateral hemispheres, suggesting widespread reorganization of the mGluR5 network.

Conclusions: First, we developed methods to accurately measure mGluR5 availability and provided a detailed assessment of the distribution throughout the brain in a large sample of healthy control subjects. In patients with FCD, we demonstrated for the first time, *in vivo* evidence of abnormal mGluR5 availability both within the dysplastic lesion and at the network level. These findings may suggest a role of mGluR5 in the epileptogenicity attributed to FCD. In addition, this work may provide novel insights into the distribution of mGluR5 availability in healthy controls and patients with FCD, which may contribute to future diagnostic and therapeutic applications targeting the mGluR5 pathway.

Résumé

Justification: La dysplasie corticale focale (DCF) est une malformation du développement cortical caractérisée histologiquement par une dyslamination corticale et la présence de neurones dysmorphiques, incluant les cellules ballonisées. Le récepteur de glutamate métabotropique de type 5 (mGluR5) est un récepteur post-synaptique couplé à une protéine G qui module l'excitabilité neuronale et joue un rôle clé dans le développement cortical. En plus d'éléments de preuve multiples en soutien d'un rôle de mGluR5 dans l'épileptogenèse, des spécimens chirurgicaux réséqués de patients atteints de DCF ont démontré qu'il existe des anomalies de mGluR5 dans les neurones dysmorphiques et les cellules ballonisées. Cependant, on ignore si les anomalies de mGluR5 pourraient être une caractéristique corticale diffuse des patients atteints de DCF, ou bien si elles seraient limitées aux démarcations de la lésion épileptogénique.

Méthodes: Afin de caractériser les anomalies du récepteur mGluR5 dans l'intégralité du cerveau chez les patients atteints de DCF, nous avons utilisé le ligand de tomographie par émission de positons (TEP) [^{11}C] ABP688. Ce ligand se lie sélectivement au site allostérique du récepteur mGluR5. De plus, afin d'assurer une comparaison précise entre la lésion DCF et le cortex sain, nous avons développé une procédure d'analyse de surfaces et une méthode de correction des effets de volumes partiel axée sur les données. En utilisant ces méthodes, nous avons réalisé les projets suivants: 1) Évaluation des différences régionales liées à la disponibilité de mGluR5 dans des contrôles sains; 2) Évaluation des anomalies mGluR5 in vivo dans un groupe

de patients atteints de DCF; 3) Caractérisation du réseau mGluR5 chez les patients atteints de DCF.

Résultats: Dans l'étude 1, nous avons observé une répartition hétérogène de la disponibilité de mGluR5 dans les structures corticales et sous-corticales, avec la plus forte liaison observé dans le cortex associatif. De plus, nous avons constaté que la disponibilité de mGluR5 était stable pour l'ensemble de la vie adulte en bonne santé et entre sexes. Dans l'étude 2, nous avons démontré que la disponibilité de mGluR5 était réduite dans la lésion dysplasique visible sur IRM. Dans la majorité des patients, des anomalies de mGluR5 ont également été observées dans les zones périlésionnelles et certaines régions éloignées. Dans l'étude 3, les patients atteints de DCF ont montré une efficacité et une résilience du réseau mGluR5 réduite dans les hémisphères ipsilatérales et contralatérales, ce qui suggère une réorganisation généralisée du réseau mGluR5 chez les patients atteints de DCF.

Conclusions: Premièrement, nous avons développé des méthodes pour mesurer avec précision la disponibilité de mGluR5 et nous avons fourni une évaluation détaillée de sa répartition dans le cerveau dans un large échantillon de sujets témoins sains. Chez les patients atteints de DCF, nous avons démontré, pour la première fois in vivo, évidence de la disponibilité anormale de mGluR5, à la fois dans la lésion dysplasique et au niveau du réseau. Ces résultats pourraient suggérer un rôle de mGluR5 dans l'épileptogénicité attribuée à la DCF. De plus, ce travail ajoute de nouvelles connaissances sur le sujet de la distribution de la disponibilité de mGluR5 dans les contrôles sains et les patients atteints de DCF, ce qui pourrait contribuer à de futures applications diagnostiques et thérapeutiques ciblant le système mGluR5.

Acknowledgements

First, I would like to wholeheartedly thank all the patients and healthy volunteers who participated in this research. Without their contribution, this work would not have been possible. In addition, I would like to thank the funding agencies that supported me throughout my PhD: The Savoy Foundation for Epilepsy and the McGill University Faculty of Medicine.

I would like to express my immense gratitude to my supervisor Dr. Eliane Kobayashi. While maintaining an extremely demanding clinical schedule, she has shown constant support and has allowed me the freedom to find unique solutions to problems, often involving analyses that neither of us fully understood at first. A special thank you to my advisor Dr. Pedro Rosa-Neto for his passionate enthusiasm for my work and for introducing me to the exciting world of PET. Additionally, I would like to thank my committee member Dr. Jean Gotman for his honest critiques, which made me a better researcher and presenter.

These projects were only possible because of the tremendous work of many collaborators from several labs. Thank you to all my collaborators (in alphabetical order): François Dubeau, Marie-Christine Guiot, Jeffery Hall, Aurelie Labbe, Gassan Massarweh, Sulantha Mathotaarachchi, Manuel Porras-Betancourt, Andrew J. Reader, Jared Rowley, Jean-Paul Soucy. Thank you especially to Dr. Olivier Rousset, whom I have yet to meet in person, but generously provided the initial framework for the partial volume correction analysis and continued advice as it was developed. Also, I appreciate Jeremy Moreau helping me to translate the abstract of this thesis into French.

Thank you to all my colleagues and friends who made Montreal feel like home: Marcel Heers, Jackie Lam, Kangjoo Lee, Sara Mohades, Antoine Leuzy, Eduardo Zimmer, Alex Zangor, Mehdi Belgnaoui, and Marie Dubenska.

Last and most importantly, thank you to my family for their love and support throughout this long and challenging process, this degree would not have been possible without you.

Contribution of authors

All the work presented in this thesis was authored by myself, in collaboration with my supervisor **Eliane Kobayashi, MD, PhD**[1] and close advisor **Pedro Rosa-Neto, MD**[1,2]**, PhD**. We designed the studies, developed and performed the analyses, and wrote the manuscripts. The contributions of each co-author are summarized below (in alphabetical order).

François Dubeau, MD[1]

Assisted in patient recruitment and description of clinical characteristics for studies 2-3

Marie-Christine Guiot, MD[1,3]

Provided histopathological diagnosis for studies 2-3, and performed mGluR5 immunohistochemistry in the specimens for study 2

Jeffery A. Hall, MD, MSc, FRCPS[1]

Performed surgical treatment and intracranial EEG investigations for studies 2-3

Aurelie Labbe, PhD[4,5]

Advised on statistical analyses for study 1

Gassan Massarweh, PhD[1]

Developed and produced the radioligand [^{11}C]ABP688 for studies 1-3

Sulantha Mathotaarachchi, MSc[2]

Assisted in development of graph theoretical analysis for study 3

Manuel Porras-Betancourt, MD[1]

Assisted in data collection of studies 1-3

Andrew J. Reader, PhD[6,7]

Assisted in PET image reconstruction analyses for studies 1-3

Olivier G. Rousset, PhD[8]

Assisted in development of partial volume correction method for studies 1-3

Jared Rowley, MD, MSc[2]
Assisted in image analyses for study 1

Jean-Paul Soucy, MD, MSc[1,6,9]
Assisted in development the radioligand [^{11}C]ABP688 for studies 1-3.

1. Department of Neurology and Neurosurgery, Montreal Neurological Institute, McGill University, Montreal, Canada
2. Translational Neuroimaging Laboratory, McGill Center for Studies in Aging, Douglas Mental Health University Institute, McGill University, Montreal, Canada
3. Department of Pathology, McGill University, Montreal, Canada
4. Department of Epidemiology, Biostatistics and Occupational health, McGill University, Montreal, Canada
5. Department of Psychiatry, Douglas Mental Health University Institute / Douglas Institut Universitaire en Santé Mentale, Montreal, Canada
6. PET Unit, McConnell Brain Imaging Center, Montreal Neurological Institute, McGill University, Montreal, Canada
7. Division of Imaging Sciences and Biomedical Engineering, King's College London, St. Thomas' Hospital, London, UK
8. Division of Nuclear Medicine and Molecular Imaging, Johns Hopkins University, Baltimore, United States of America
9. Bio-Imaging Group, PERFORM Centre, Concordia University, Montreal, Canada

Funding: The Savoy Foundation for Epilepsy (pilot project grant to E.K. and P.R.N. and Ph.D. studentship to J.M.D.); The American Epilepsy Society (Early Career Physician Scientist Award to E.K.); Canadian Institutes of Health Research (MOP-115131 to P.R.N. and MOP-93614 to E.K.); The Fonds de la recherche en santé du Québec (www.frqs.gouv.qc. ca) (P.R.N., chercheur boursier).

Contributions to original knowledge

Study 1. Characterization of age/sex, and the regional distribution of mGluR5 availability in the healthy human brain measured by high-resolution [^{11}C]ABP688 PET

1) We developed surface-based methods for partial volume correction and statistical comparisons that allowed for more accurate assessment of mGluR5 abnormalities; 2) we characterized the cortical distribution of mGluR5 availability in far greater detail than previous studies, showing high mGluR5 availability in association cortices such as the anterior cingulate, lateral parietal, and superior frontal regions; 3) In a large group of healthy controls, with a broader age distribution of male and female participants than prior studies, we demonstrated that mGluR5 availability is stable across the lifespan and does not differ between sexes. These findings, along with the methods that were developed, provided a framework that was utilized throughout my thesis research and in additional studies.

Study 2. mGluR5 cortical abnormalities in focal cortical dysplasia identified in vivo with [11C]ABP688 PET imaging

1) Using [^{11}C]ABP688 PET with the methods described in study 1, we demonstrated for the first time, *in vivo* evidence of reduced mGluR5 availability within the dysplastic lesion of patients with FCD; 2) We also observed areas of extra-lesional mGluR5 abnormalities that were not associated with a structural lesion or poorer surgical

outcome. Overall these results suggest that patients with FCD may have focal glutamatergic alterations that extend beyond the seizure focus.

Study 3. Reduced efficiency of the mGluR5 network in patients with focal cortical dysplasia: a graph-theoretical analysis of [^{11}C]ABP688 PET

1) We developed novel analyses to create individual-level network graphs based on the inter-regional similarity of [^{11}C]ABP688 PET; 2) We showed reduced network efficiency and network resilience in the ipsilateral and contralateral hemispheres in patients with FCD. This is one of the first studies, of any modality, to describe network-wide alterations in patients with FCD. To our knowledge, this is also the first application of graph theoretical analysis to neuroreceptor PET imaging.

Common abbreviations

[^{11}C]ABP688	3-(6-methyl-pyridin-2-ylethynyl)-cyclohex-2-enone-O-^{11}C-methyloxime
AUC	area under the curve
BP_{ND}	binding potential non-displaceable
EEG	electroencephalography
FCD	focal cortical dysplasia
FDG	^{18}F-fluorodeoxyglucose
FDR	False discovery rate
FLAIR	fluid attenuated inversion recovery
fMRI	functional magnetic resonance imaging
FWHM	full width at half maximum
HRRT	high resolution research tomograph
iGluR	ionotropic glutamate receptors
KLS	Kullback-Leibler similarity
mGluR	metabotropic glutamate receptor
mGluR5	metabotropic glutamate receptor type 5
mMG-PVC	Muller-Gartner partial volume correction
MRI	magnetic resonance imaging
mTOR	mammalian target of rapamycin
NMDA	N-methyl-D-aspartate
OP-OSEM	ordinary Poisson ordered subsets expectation maximization
PET	positron emission tomography
PVC	partial volume correction
PVE	partial volume effects
RBV-PVC	region-based voxel-wise partial volume correction

List of figures

List of tables

Chapter 1

Introduction

Epilepsy is the most common neurological condition among children, and the third most common among adults (Jones et al., 2008). Approximately one-third of patients with epilepsy experience seizures that are not controlled by antiepileptic drugs (Mohanraj and Brodie, 2006; Brodie, 2013). In such cases, malformations of cortical development, specifically focal cortical dysplasia (FCD), are increasingly recognized as an underlying cause (Frater et al., 2000; Sisodiya, 2000; Harvey et al., 2008; Lerner et al., 2009).

Ex vivo tissue specimens resected from patients with FCD have shown mGluR5 abnormalities in dysmorphic neurons and balloon cells (Aronica et al., 2003). In addition, several lines of evidence support a role of mGluR5 in epileptogenesis, including studies showing that mGluR5 antagonism has an anticonvulsant effect in hippocampal slice preparations, while mGluR5 agonism initiated persistent epileptiform activity (Merlin, 2002; Catania et al., 2007). However, it remains unknown whether mGluR5 abnormalities could be a diffuse cortical characteristic of patients with FCD or limited to the boundaries of the dysplastic lesion.

The recently developed radiopharmaceutical 3-(6-methyl-pyridin-2-ylethynyl)-cyclohex-2-enone-O-11C-methyloxime ([^{11}C]ABP688) allows for *in vivo* quantification of

mGluR5 availability using positron emission tomography (PET) (Ametamey, 2006). Previous *in vivo* studies of [^{11}C]ABP688 PET in healthy subjects confirmed *post mortem* data showing high binding in known mGluR5 dense regions such as the striatum, the hippocampus, and the anterior cingulate cortex, with low binding in the thalamus and the cerebellum (Ametamey et al., 2007; Treyer et al., 2007). However, thus far studies have not investigated the age and sex effects on mGluR5 availability in healthy volunteers, which may be necessary to ensure accurate comparisons between patients with FCD and healthy controls.

The primary aims of this thesis are first, to characterize mGluR5 availability in healthy individuals, including an assessment of age and sex effects as well as a detailed analysis of the cortical distribution. Second, we aim to investigate *in vivo* mGluR5 abnormalities in patients with FCD, both within the dysplastic lesion and throughout the cortex. Lastly, we aim to investigate the characteristics of the mGluR5 network using a graph theoretical framework. In addition, we developed several methodologies that allowed for accurate comparison of patients with FCD to healthy controls.

The thesis is organized as follows: Chapter 2 reviews the background literature concerning malformations of cortical development, FCD, mGluR5, and [^{11}C]ABP688. Chapters 3 to 5 comprise a series of manuscripts that describe the studies carried out as part of my PhD research. Chapter 6 highlights the key findings and discusses future directions.

Chapter 2

Background

2.1 MALFORMATIONS OF CORTICAL DEVELOPMENT

Cortical development is a complex and precisely organized process that when disrupted, causes malformations of cortical development (Guerrini and Dobyns, 2014; Desikan and Barkovich, 2016). Epilepsy is thought to occur in approximately 75% of patients with a malformation of cortical development (Leventer et al., 1999), while cognitive dysfunction is more common in diffuse malformations originating in early cortical development (Guerrini and Dobyns, 2014). Malformations of cortical development are classified into 1 of 3 groups based on the developmental stage at which the disruption occurred: cell proliferation, neural migration, and cortical organization and connectivity (Figure 2.1) (Barkovich et al., 2012). Below, we broadly review the stages of healthy cortical development and the corresponding malformations of cortical development, followed by detailed discussion of FCD.

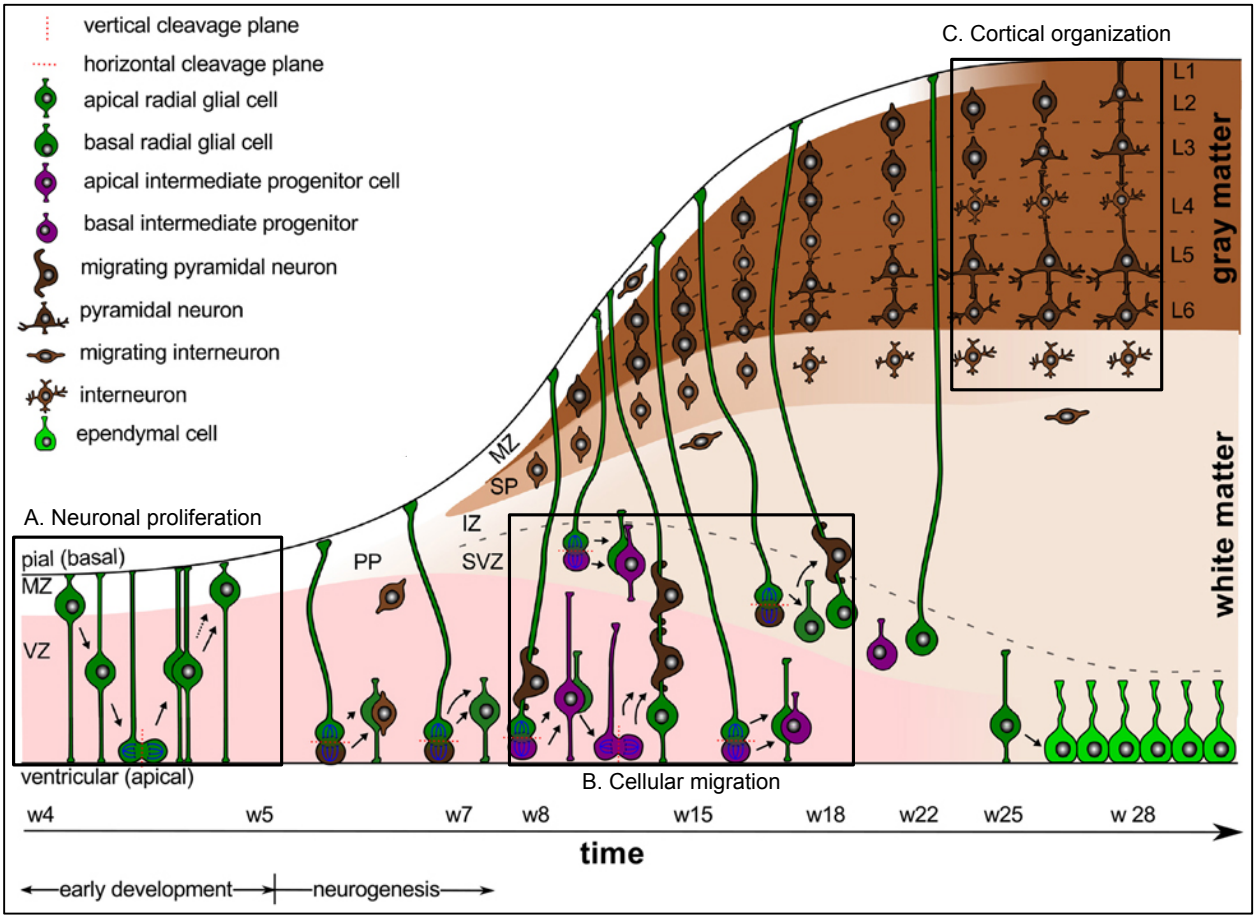

Figure 2.1 Cortical development. Displays the three primary phases of cortical development from gestational week 4-28. Proliferation of progenitor cells in the ventricular zone (VZ) begins at week 4 (A), followed by migration of mitotic neurons along radial glia, from the VZ to the gray matter of the cortex (B). Radial migration of pyramidal neurons is capped at the marginal zone (MZ) to ensure that this region becomes cortical layer 1. At approximately week 22, laminar organization is fully established and dendrites are begin extending to form intracortical connections (C). This figure was adapted with permission from (Budday et al., 2015).

2.1.1 *Malformations secondary to abnormal cell proliferation or apoptosis*

Cortical development originates in the germinal matrix along the lateral ventricles (i.e. ventricular zone), where progenitor cells proliferate and develop into radial glia and post mitotic neurons (Figure 2.1A) (Kandel, 2012; Budday et al., 2015). Malformations at this stage of development include microcephalies and megalencephalies, which are due to reduced proliferation/increased apoptosis and increased proliferation/reduced

apoptosis, respectively (Figure 2.2A and B). In addition, abnormal proliferation can result in FCDs (Figure 2.2C and D) (Barkovich et al., 2012; Guerrini and Dobyns, 2014). Genes associated with microcephaly affect a broad spectrum of proteins for progenitor cell division, neuronal maturation, and microtubule formation (Desikan and Barkovich, 2016). Megalencephalies and FCDs however, are primarily associated with mutations of genes affecting the mammalian target of rapamycin (mTOR) pathway (Jansen et al., 2015; Moller et al., 2016), which is a central regulator of several cellular mechanisms, including activity dependent postsynaptic protein synthesis (Laplante and Sabatini, 2012).

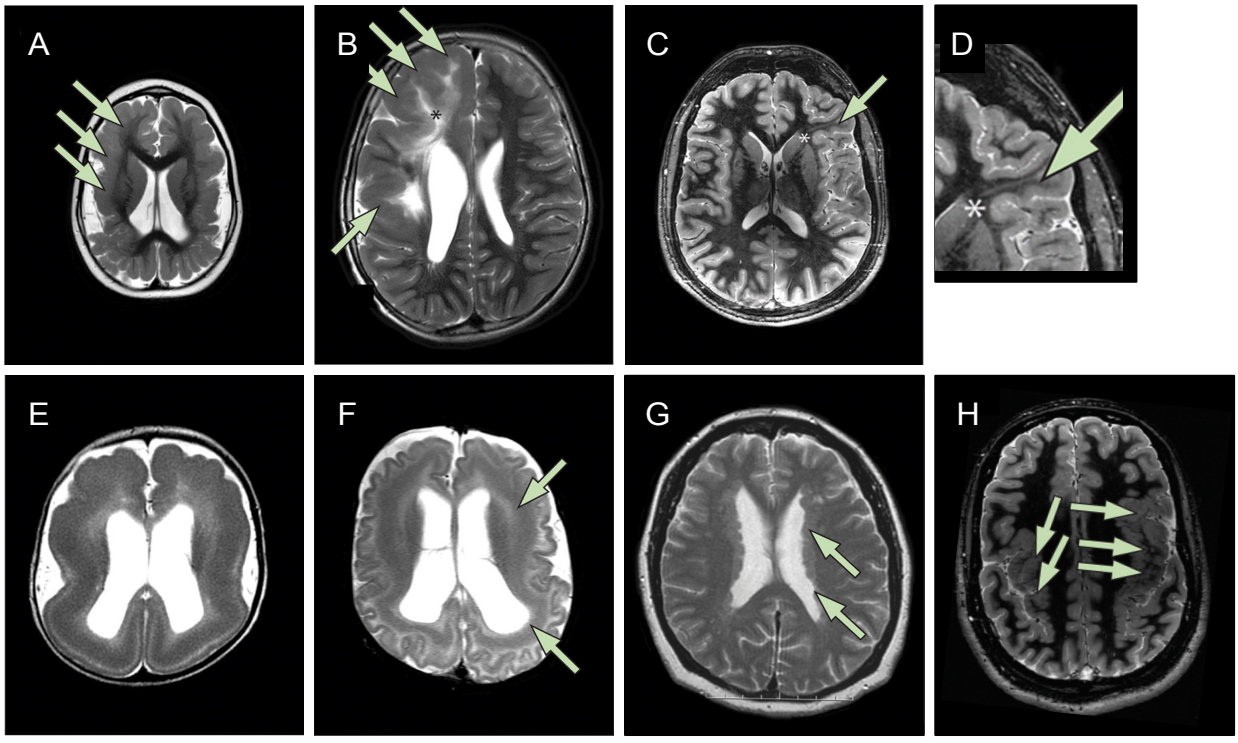

Figure 2.2 Malformations of cortical development. Malformations of cortical development including microcephaly with a polymicrogyria-like malformation (A), right frontal megalencephaly (B), left frontal FCD Type 2B (C), inflated image of FCD in image C (D), grade 3 classic lissencephaly (E), subcortical band heterotopia (F), periventricular nodular heterotopia (G), perisylvian polymicrogyria. This figure was adapted with permission from (Guerrini and Dobyns, 2014).

2.1.2 *Malformations secondary to abnormal cell migration*

At approximately gestational week 7, post-mitotic neurons begin migrating along radial glial cells from the ventricular zone to the appropriate layer of the cortex (Figure 2.1B) (Kandel, 2012; Budday et al., 2015). Malformations of cell migration include lissencephalies (Figure 2.2E), in which too few neurons migrate to the cortex, and heterotopia (Figure 2.2F and G), in which neuronal migration is improperly arrested in the white matter (Desikan and Barkovich, 2016). Lissencephalies are associated with reduced gyrification or complete agyria and diffuse, often asymmetrical, disorganization of the cortical lamina (Figure 2.2E) (Guerrini and Dobyns, 2014). Heterotopia encompass a spectrum of abnormalities ranging from rudimentary laminar organization (subcortical band heterotopia), to disorganized groupings of neurons and glia in the deep white matter (subcortical nodular heterotopia) or adjacent to the lateral ventricles (periventricular nodular heterotopia) (Barkovich and Kuzniecky, 2000; Kakita et al., 2002). Although the molecular pathways associated with migrational malformations are not fully understood, recent studies suggest that some lissencephalies and heterotopia may be due to mutations encoding microtubule-associated proteins (Bahi-Buisson et al., 2014; Watrin et al., 2015). Microtubule-associated proteins play a critical role in neuronal development, neuronal attachment to radial glia, and migration (Valiente and Marin, 2010). However, due to their broad effects, microtubule-associated protein genes are also associated with malformations at each stage of cortical development, including microcephaly and polymicrogyria (Bahi-Buisson et al., 2014).

2.1.3 *Malformations Secondary to Abnormal Postmigrational Development*

Following migration to the cortex, pyramidal neurons begin to elongate and extend dendrites, which later form intracortical connections (Figure 2.1C) (Budday et al., 2015). Polymicrogyria is the primary malformation of abnormal cortical organization (Figure 2.2H). It is characterized by an increased number of small convolutions and disorganized cortical lamina, most commonly in the perisylvian region (Desikan and Barkovich, 2016). Studies have suggested that polymicrogyria may be caused by prenatal damage to the marginal zone, resulting in sporadic over-migration of pyramidal neurons (Jansen et al., 2016). However, there is also evidence of genetic mutations in some forms of polymicrogyria, related to both microtubule-associated proteins and the mTOR pathway (Bahi-Buisson et al., 2014; Stutterd and Leventer, 2014).

Overall, malformations of cortical development comprise a broad spectrum of anatomical abnormalities, likely caused by overlapping molecular mechanisms. Further research is needed to delineate the molecular pathways disrupted, as well as to facilitate therapeutic and diagnostic tools targeting these systems.

2.2 FOCAL CORTICAL DYSPLASIA

When first described by Taylor et al. in 1971, FCDs were found in only 3% of operative cases (Taylor et al., 1971). Today, due to advances in neuroimaging, FCD is the second most common etiology identified in adult surgical candidates with epilepsy (Harvey et al., 2008; Lerner et al., 2009). Despite technological advances, post-operative histopathological studies show that between 50% and 80% of FCDs are not detected by routine magnetic resonance imaging (MRI) (Besson et al., 2008). Amongst

refractory epilepsies treated with surgical resection, FCD is found in 20-25% of adults and up to 42% of pediatric patients (Tassi et al., 2002; Harvey et al., 2008).

Seizure presentation in patients with FCD can vary widely depending on the location and extent of the lesion, as well as the age of the patient. Infantile spasms are common in early onset cases of FCD, while patients beyond infancy often have focal seizures with or without secondary generalization (Palmini et al., 1991; Sisodiya et al., 2009). However, partial seizures may arise from multiple epileptic foci and show fast propagation to local and distant gray matter regions, suggesting that a diffuse abnormality may be present in some cases (Duchowny et al., 2000; Tyvaert et al., 2008). Interictal neurophysiological studies, have consistently shown rhythmic fast epileptiform discharges in patients with FCD, suggesting an intrinsic epileptogenicity of dysplastic cortex (Palmini et al., 1995; Bast et al., 2004; Tyvaert et al., 2008).

FCDs encompass a range of histopathological abnormalities including excessive neuroglial proliferation and disorganized cortical lamina, with giant (cytomegalic) neurons, dysmorphic neurons, and balloon cells (Figure 2.3) (Prayson et al., 2002; Palmini et al., 2004; Barkovich et al., 2005; Blumcke et al., 2011). Due to neuroimaging appearance and likely distinct developmental pathways, FCD with balloon cells (FCD type IIB) is distinguished from FCD without balloon cells in the malformation of cortical development classification (Palmini et al., 2004; Barkovich et al., 2005; Blumcke et al., 2011). Dysplastic neurons and balloon cells may originate from radial glia progenitor cells in the periventricular matrix (Ying et al., 2005; Lamparello et al., 2007; Guerrini et al., 2008).

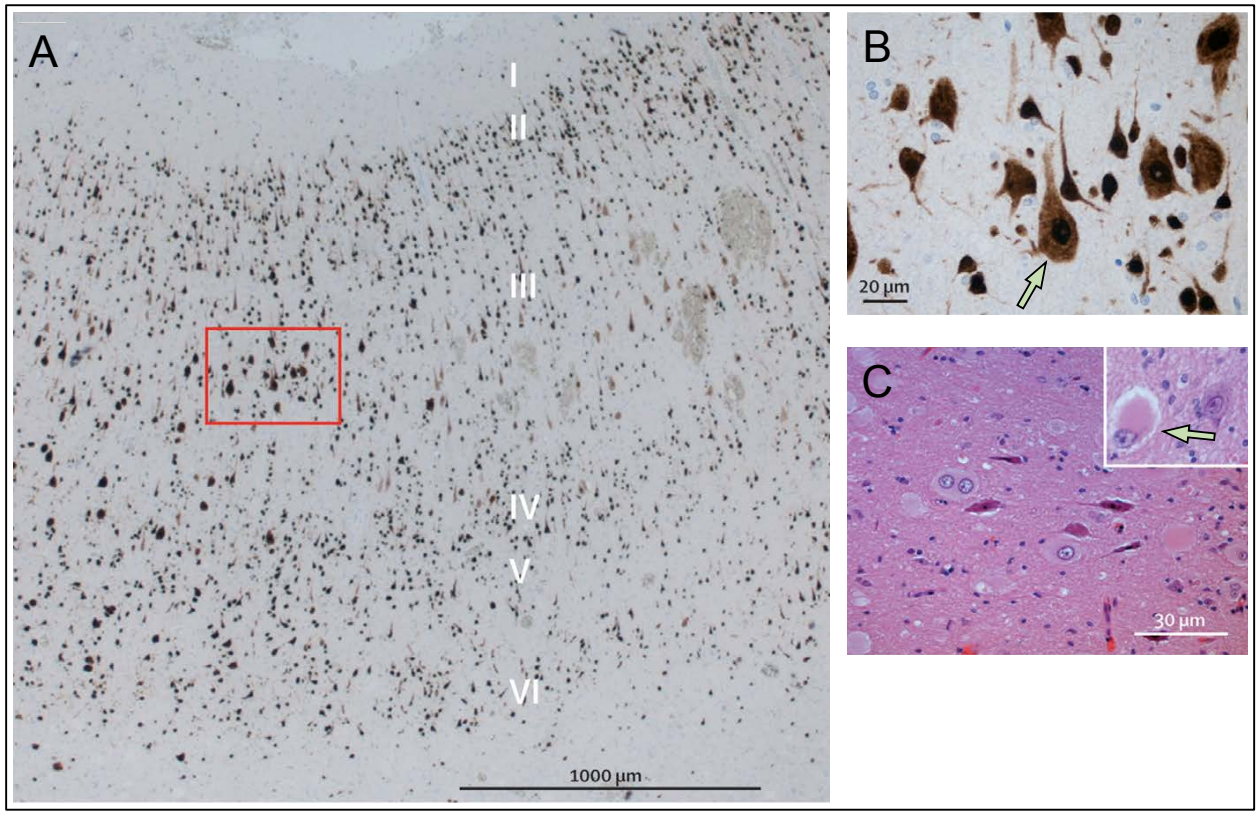

Figure 2.3 Pathological features of FCD. FCD type IIB lesion section immunostained with neuronal nuclei (NeuN), showing disorganized cortical layers and a cluster of dysmorphic neurons (A; red box). NeuN immunostained region highlighted in (A), showing dysmorphic neurons (arrow) intermingled with normally sized neurons (B). Haematoxylin and eosin section from FCD type IIB lesion, showing dysmorphic neurons and balloon cells (C; arrow). This figure was adapted with permission from (Sisodiya et al., 2009).

Structural imaging findings in FCD include thickening of the cortex (Figure 2.4A) and blurring of the gray/white matter boundary (Figure 2.4E) on T1-weighted MRI (Barkovich et al., 2001). Using T2 and fluid attenuated inversion recovery (FLAIR) MRI sequences, hyperintensities may be found within the lesion (Figure 2.4B) or in a band of signal extending from the cortex toward the lateral ventricle (Figure 2.4C and D), known as a transmantle sign (Barkovich, 1995; Wang et al., 2013). Transmantle signs may be

more common in patients with small lesions located at the bottom of a sulcus (Wang et al., 2013). While the heterogeneous distribution of neuroanatomical abnormalities within the FCD lesion can often make it difficult to discern dysplastic cortex from healthy cortex, improved detection has been found with quantitative analysis of morphological features such as cortical thickness, gray/white matter contrast, and gyrification (Thesen et al., 2011; Hong et al., 2014).

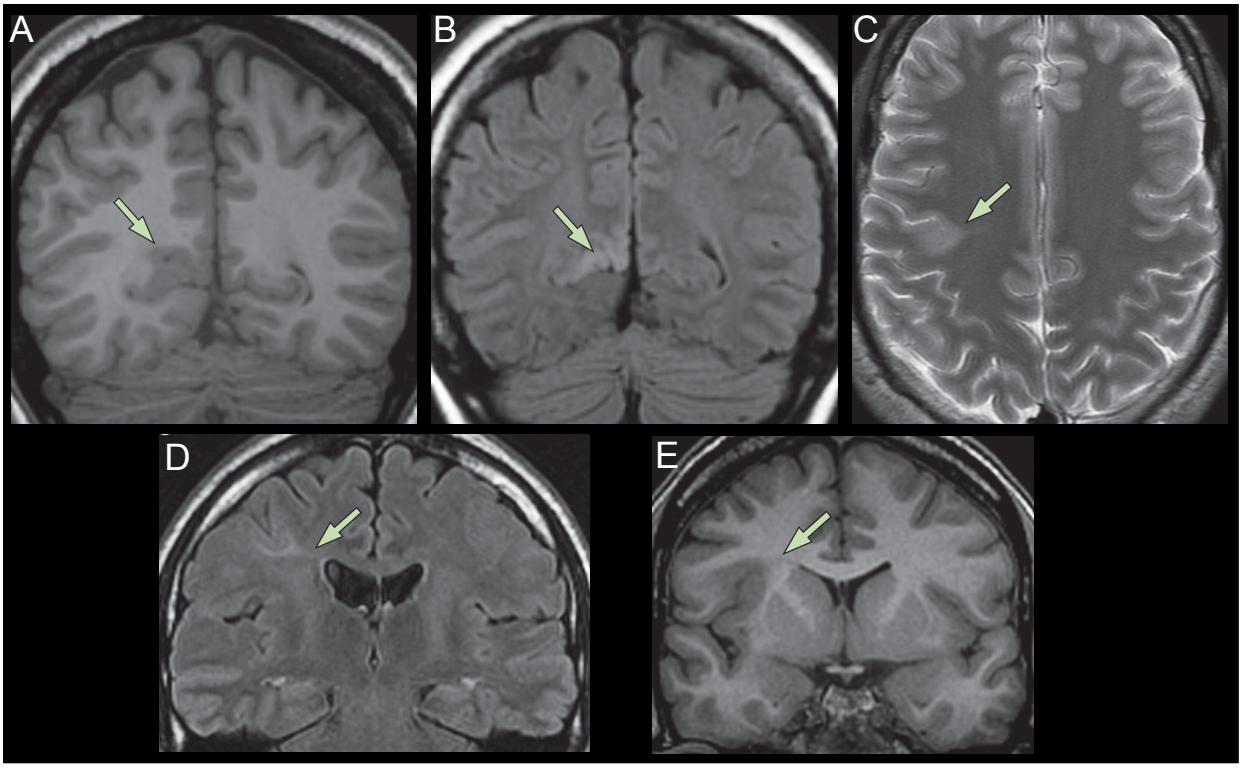

Figure 2.4 T1 and T2-weighted MRI of FCD type II. Coronal slice of T1-weighted MRI, showing increased cortical thickness (A; arrow), with increased FLAIR signal in the same region (B). Axial slice of fast spin-echo MRI sequence, showing increased cortical thickness and a subtle transmatle sign (C; arrow), which is more clearly visible in the coronal FLAIR image (D; arrow). Coronal slice of T1-weighted MRI, showing blurring of the gray/white matter boundary (E; arrow). This figure was adapted with permission from (Sisodiya et al., 2009).

In addition to neuroanatomical abnormalities, PET imaging with ^{18}F-fluorodeoxyglucose (FDG) has shown lesional hypometabolism in 71% – 87% of

patients with FCD (Salamon et al., 2008; Chassoux et al., 2010). Markers of inflammation were also shown to be increased within the lesion using [^{11}C]PK11195 PET in a single case of a patient with FCD (Butler et al., 2013). However, much less research has focused on neuroreceptor PET imaging of the molecular pathways that may underlie epileptogenesis in FCD. PET studies utilizing the N-methyl-D-aspartate (NMDA) receptor ligand [^{18}F]GE-179 showed localizing value in only 36% of patients with FCD (McGinnity et al., 2015). Studies of [^{11}C]flumazenil PET in patients with focal neocortical epilepsy, including FCD, have consistently demonstrated abnormal γ-aminobutyric acid$_A$ ($GABA_A$) receptor binding (Richardson et al., 1996; Hammers et al., 2001; Juhasz et al., 2001; Hammers et al., 2003).

Using immunoreactivity, receptor subunits for $GABA_A$ have shown decreased expression in dysplastic neurons when compared to normal cortex (Crino et al., 2001). However, microdialysis studies in patients with mesial temporal lobe epilepsy shows increases in GABA concentrations in the seizure focus were secondary to increases in glutamate concentrations proceeding seizures (During and Spencer, 1993). Dysplastic neurons have also shown increased expression of proteins for excitatory ionotropic glutamate receptors (iGluRs) including NMDA and α-amino-3-hydroxy-5-methyl-4-isoxazolepropionic acid (AMPA) (Crino et al., 2001; White et al., 2001). However, traditional anti-epileptic drugs targeting ion channels regulated by iGluRs are often ineffective in patients with FCD (Rogawski and Löscher, 2004; Alexander and Godwin, 2006). A separate group of receptors that has been less well studied are metabotropic glutamate receptors. Surgical specimens from patients with drug-resistant focal epilepsy and FCD show that mGluR5 was expressed in a large proportion of dysplastic and

heterotopic neurons, suggesting that mGluR5 may play a role in the intrinsic epileptogenicity of dysplastic cortex (Aronica et al., 2003).

2.3 METABOTROPIC GLUTAMATE RECEPTOR TYPE 5

Glutamate is the primary excitatory neurotransmitter in the central nervous system, controlling fast cortical processing via iGluRs. In addition, glutamate activates mGluRs, which modulate intracellular excitatory pathways, leading to long-term potentiation and depression. mGluRs are class C G-protein coupled receptors, consisting of 8 receptor subtypes, divided into 3 groups (Nicoletti et al., 2011). Group II and group III mGluRs are primarily located on the presynaptic terminal, whereas group I mGluRs, including mGluR1 and mGluR5, are found in the periphery of the postsynaptic terminal (Niswender and Conn, 2010). Via intracellular secondary messengers, group I mGluRs mediate neuronal excitability and postsynaptic plasticity (Figure 2.5) (Conn and Pin, 1997; Anwyl, 1999).

Group I mGluRs have a large extracellular domain including a Venus flytrap glutamate binding site, and a cysteine rich domain connected by 7 transmembrane helices to the intracellular COOH terminal (reviewed by Nicoletti, 1999). A disulphide bridge binds the receptors to form functional homodimers that require two orthosterically bound ligands (e.g. glutamate) for activation (Kniazeff et al., 2004). Generally, agonist binding to group I mGluRs causes a conformational change in the receptor leading to the intracellular exchange of guanosine diphosphate (GDP) for guanosine triphosphate (GTP) and stimulation of phospholipase C (PLC) (Gomeza et al., 1996; Pin et al., 2005). PLC cleaves phosphatidylinositol 4,5-bisphosphate (PIP_2), resulting in the formation of

inositol-1,4,5-trisphosphate (IP_3) and diacylglycerol (DAG). IP_3 initiates the release of cytosolic Ca^2+ from the endoplasmic reticulum, which bind to protein kinase C (PKC). PKC is then translocated to the cell membrane, where it is activated by DAG (reviewed by Hermans and Challiss, 2001).

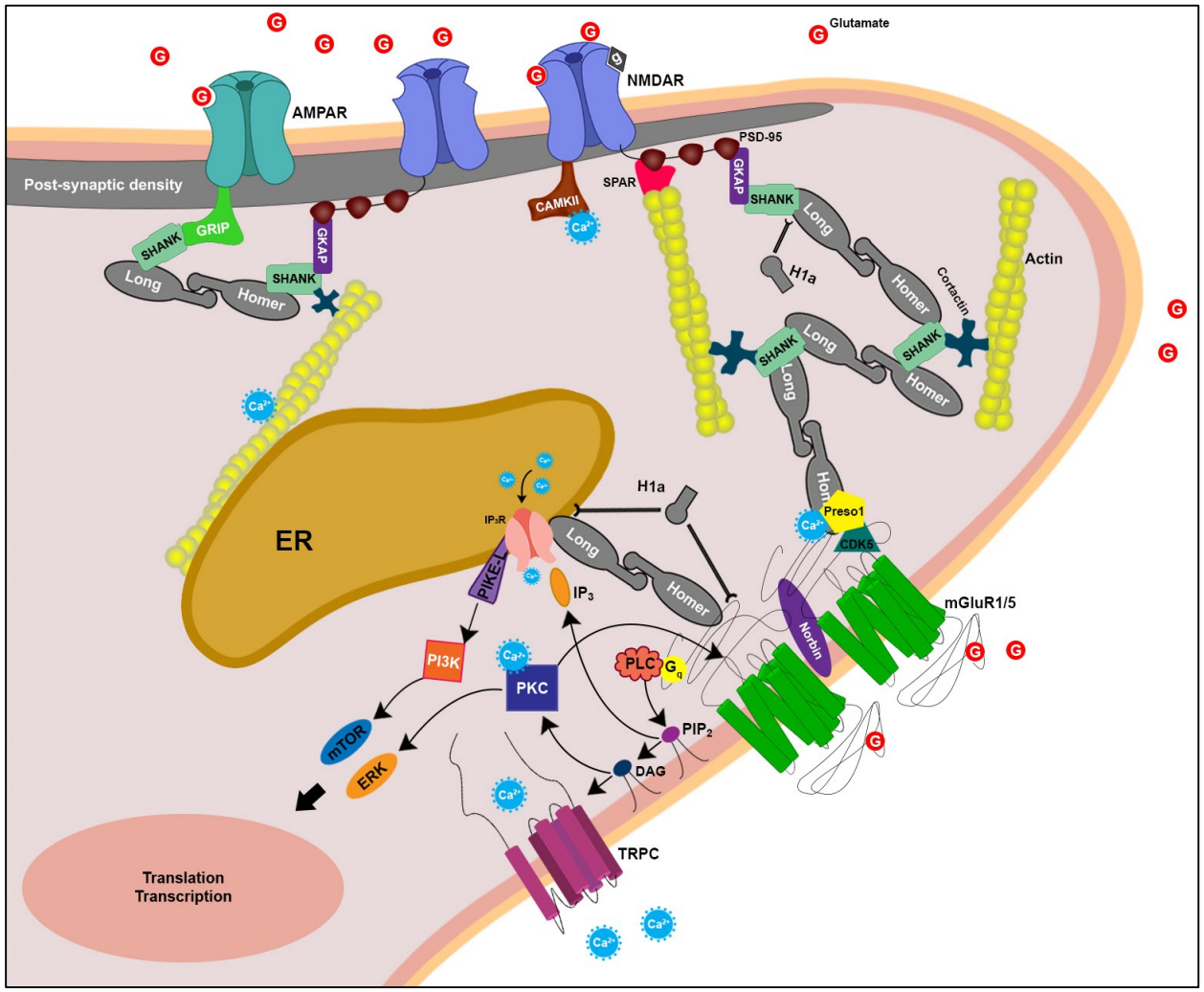

Figure 2.5 mGluR5 signaling pathways. Schematic representation of intracellular secondary messengers that interact with mGluR5 within the postsynaptic terminal. Active mGluR5 homodimers are shown in green with GTP (G_q) and PLC attached to the intracellular domain. Secondary messengers are shown with black arrows indicating their downstream targets, leading to protein synthesis via mTOR and ERK pathways.

Once activated, PKC desensitizes group I mGluRs by phosphorylating multiple intracellular sites including an mGluR5 specific threonine residue (T840) (Nakahara et al., 1997). NMDA activation promotes a positive feedback loop with mGluR5 by reversing PKC-mediated phosphorylation, which may result in an oscillatory pattern of Ca^2+ release from intracellular stores observed in mGluR5-related PKC activation (Alagarsamy et al., 1999; Flint et al., 1999). In addition, PKC activation initiates a signaling pathway leading to phosphorylation of the extracellular-signal-regulated kinase (ERK), which can trigger translational and transcriptional factors (e.g. cAMP response element-binding protein) (Kim et al., 2008).

Due to the broad range of mGluR5 signaling pathways, membrane targeting via the long and short form of Homer scaffolding proteins (Homer1a and Homer1b/c, respectively) plays a key role. Under normal conditions, reciprocal promotion between mGluR5 and NMDA receptors is regulated by Homer1a, which inhibits NMDA activation following prolonged synaptic activity (Field et al., 2011; Moutin et al., 2012). Homer scaffolding proteins also mediate dendritic targeting of mGluR5 to the postsynaptic density, which is dependent upon synaptic activity (Ango et al., 2000). In addition, the interaction between long Homer proteins and phosphoinositide 3 kinase enhancer-long (PIKE-L) mediate the activation of phosphoinositide 3 kinase (PI_3K). PI_3K plays a critical role in the activation of the mTOR pathway, which converges with the ERK pathway to stimulate protein synthesis, resulting in long term potentiation and depression (Rong et al., 2003; Niswender and Conn, 2010).

Increased cytosolic Ca^2+ is a primary consequence of mGluR5 activation, as it initiates several downstream pathways leading to increased neuronal excitability.

However, excessive cytosolic Ca^2+, due to over excitation, may initiate neurotoxic pathways leading to excitotoxicity (Mehta et al., 2013). Although there are several regulatory mechanisms to protect against excitotoxicity, they may be overridden by pathological levels of extracellular glutamate, which have been found in the epileptic focus (During and Spencer, 1993; Eid et al., 2004). In hippocampal slices, the group I mGluR selective agonist (*S*)-3,5-dihydroxyphenylglycine (DHPG) produced prolonged epileptiform bursts, which were prevented by administration of the mGluR5 antagonist 2-methyl-6-(phenylethynyl)-pyridine (MPEP) (Merlin and Wong, 1997). As a result, mGluR5 has been investigated as a therapeutic target for epilepsy as well as other neurological and psychiatric disorders (for review see Benarroch, 2008).

2.4 [^{11}C]ABP688 PET

PET imaging with [^{11}C]ABP688 offers the opportunity to visualize mGluR5 availability non-invasively. While previous studies of mGluR5 immunoreactivity have been limited to surgically resected tissue, [^{11}C]ABP688 PET allows for analysis of abnormalities in mGluR5 availability throughout the brain. Moreover, [^{11}C]ABP688 PET imaging can be acquired broadly across patients and controls, which allows for more powerful statistical comparisons.

[^{11}C]ABP688 shows high affinity for mGluR5, as well as good blood-brain barrier permeability and fast kinetics (Ametamey, 2006; Hintermann et al., 2007; Wyss et al., 2007). It is synthesized in 45-50min, with high radiochemical purity (>99%) (Elmenhorst et al., 2010). *Ex vivo* studies of the rat brain as well as *in vivo* studies in humans show highly selective uptake of [^{11}C]ABP688 with accumulation in mGluR5 dense regions

such as the hippocampus, striatum, and cortex (Ametamey, 2006; Ametamey et al., 2007; Treyer et al., 2007). These studies also show negligible binding in the cerebellum and white matter where mGluR5 expression is minimal (Ametamey et al., 2007; Elmenhorst et al., 2010). Non-specific binding of [^{11}C]ABP688 in the cerebellum allows for this region to be used as a reference for calculating non-displaceable binding potential values (BP_{ND}) in the rest of the brain (Lammertsma and Hume, 1996; Elmenhorst et al., 2010). This method has been shown to have a high correspondence with kinetic constants ratio estimates using arterial input function in humans and rodents (Elmenhorst et al., 2010; Milella et al., 2011).

Studies reporting on [^{11}C]ABP688 binding in healthy individuals have generally done so secondary to investigations of psychiatric disorders or addiction, and utilized a limited number of subjects with a narrow age and sex distribution. A study investigating the association between [^{11}C]ABP688 binding and smoking showed that female non-smokers had significantly lower [^{11}C]ABP688 binding than males non-smokers in the caudate, mesial temporal lobe, orbital frontal cortex, and thalamus. However, only 14 (8 female / 6 male) non-smoking volunteers were included (Akkus et al., 2013). Age has been associated with increased [^{11}C]ABP688 binding throughout the brain of cocaine users and in the medial temporal lobe, cingulate cortex, and parietal lobe of smokers, but age-related differences have not been found in healthy controls (Deschwanden et al., 2011; Akkus et al., 2013; Hulka et al., 2014). However, only one study included subjects older than 40 years of age (Deschwanden et al., 2011).

[^{11}C]ABP688 occupies the transmembrane allosteric binding site rather than the orthosteric binding site, inducing a conformational change in the receptor, which

reduces the effect of glutamate binding (Ametamey, 2006). Therefore, it is considered a negative modulator of mGluR5. There is also recent evidence suggesting that glutamate binding may induce a conformational change in mGluR5 that reduces the probability of [^{11}C]ABP688 binding (DeLorenzo et al., 2014). This is further supported by a combined microdialysis and PET study in rats, which demonstrated increased [^{11}C]ABP688 binding by activation of the GLT-1 transporter, which reduced extracellular glutamate concentrations (Zimmer et al., 2015b). This mechanism may underlie the finding of increased [^{11}C]ABP688 binding upon repeated same-day PET scanning in a group of human controls. In that study, the authors suggest that the participants experienced decreased anxiety during the follow-up scan, which was about 2 hours after the original, leading to decreased glutamatergic neurotransmission and an increase in available binding sites for [^{11}C]ABP688 (DeLorenzo et al., 2011a). Alternatively, test-retest differences may be caused by diurnal variation in mGluR5 availability, as larger intervals prior to retesting (days or weeks) did not show a significant difference between scans (Burger et al., 2010; DeLorenzo et al., 2016; Elmenhorst et al., 2016). These studies highlight the wide range of possible mechanisms affecting [^{11}C]ABP688 binding to mGluR5, including receptor internalization, the functional state of receptor (high/low affinity), the total amount of protein in the tissue, conformational changes, anomalous receptor isoforms, or excessive concentrations of endogenous ligands, such as glutamate (Chugani et al., 1988; van Wieringen et al., 2013; DeLorenzo et al., 2014; Zimmer et al., 2015a; Vidal et al., 2016).

In a prior group analysis of [^{11}C]ABP688 in patients with mesial temporal lobe epilepsy, decreased binding was found in the hippocampus (Kobayashi et al., 2010).

This result contrasts immunoreactivity studies showing increased mGluR5 expression in hippocampal tissue specimens resected from patients with mesial temporal lobe epilepsy (Notenboom et al., 2006; Kandratavicius et al., 2013). In patients with epilepsy who have pathologically high levels of extracellular glutamate in the seizure focus (During and Spencer, 1993), regionally decreased [^{11}C]ABP688 binding may be due to a conformational change in mGluR5 as result of glutamate binding rather than decreased expression of mGluR5.

In addition to epilepsy, mGluR5 differences have been demonstrated in several central nervous system disorders, including major depressive disorder, fragile X syndrome, addiction, and schizophrenia (Dölen and Bear, 2008; Niswender and Conn, 2010; Deschwanden et al., 2011; Akkus et al., 2013; Martinez et al., 2014). Therefore, [^{11}C]ABP688 PET could shed light on several complex phenotypes related to mGluR5 dysfunction and advance the development of novel therapeutic and diagnostic tools targeting the mGluR5 pathways.

Chapter 3

Characterization of age, sex, and the regional distribution of mGluR5 availability in the healthy human brain measured by high-resolution [^{11}C]ABP688 PET

This work was published in:
Eur J Nucl Med Mol Imaging, 2016, 43(1):152-163

3.1 PREFACE

In order to accurately detect mGluR5 abnormalities in patients with FCD, we first aimed to characterize mGluR5 availability in healthy individuals. Early studies evaluating the binding properties of [^{11}C]ABP688 reported increased mGluR5 availability in the anterior cingulate and putamen, with low availability in the cerebellum (Ametamey et al., 2007; Treyer et al., 2007). However, these studies suffered from imprecise segmentation methods as well as a narrow distribution of age and sex amongst controls. Further understanding of these factors is essential for design of patient-control studies, determining for example, if a matched control group is necessary for patient comparisons or if certain brain regions are less sensitive to detection of abnormalities. Therefore, the purpose of this study was to utilize high-resolution [^{11}C]ABP688 PET and advanced image analyses, to precisely describe the cortical and subcortical distribution

of mGluR5 availability in a large sample of healthy individuals.

3.2 ABSTRACT

Metabotropic glutamate receptor type 5 (mGluR5) is a G protein-coupled receptor that has been implicated in several psychiatric and neurological diseases. The radiopharmaceutical [^{11}C]ABP688 allows for in vivo quantification of mGluR5 availability using positron emission tomography (PET). In this study, we aimed to detail the regional distribution of [^{11}C]ABP688 binding potential (BP_{ND}) and the existence of age/sex effects in healthy individuals. Thirty-one healthy individuals aged 20 to 77 years (men, n = 18, 45.3 ± 18.2 years; females, n = 13, 41.5 ± 19.6 years) underwent imaging with [^{11}C]ABP688 using the high-resolution research tomograph (HRRT). We developed an advanced partial volume correction (PVC) method using surface-based analysis in order to accurately estimate the regional variation of radioactivity. BP_{ND} was calculated using the simplified reference tissue model, with the cerebellum as the reference region. Surface-based and volume-based analyses were performed for 39 cortical and subcortical regions of interest per hemisphere. We found the highest [^{11}C]ABP688 BP_{ND} in the lateral prefrontal and anterior cingulate cortices. The lowest [^{11}C]ABP688 BP_{ND} was observed in the pre- and post-central gyri as well as the occipital lobes and the thalami. No sex effect was observed. Associations between age and [^{11}C]ABP688 BP_{ND} without PVC were observed in the right amygdala and left putamen, but were not significant after multiple comparisons correction. The present results highlight complexities underlying brain adaptations during the aging process, and support the notion that certain aspects of neurotransmission remain stable during the adult life span.

3.3 **INTRODUCTION**

Metabotropic glutamate receptor type 5 (mGluR5) is a G protein-coupled receptor that plays a critical role in learning and memory (Anwyl, 1999; Cartmell and Schoepp, 2000). Through several intracellular cascades, mGluR5 modulates neuronal excitability and synaptic plasticity, leading to long-term potentiation and long-term depression (Hermans and Challiss, 2001; Waung and Huber, 2009). It is currently being investigated as a therapeutic target, given the growing evidence of its role in several psychiatric and neurological disorders ((for review see Benarroch, 2008)).

The recently developed radiopharmaceutical 3-(6-methyl-pyridin-2-ylethynyl)-cyclohex-2-enone-O-11C-methyloxime ([^{11}C]ABP688) allows for in vivo quantification of mGluR5 availability using positron emission tomography (PET) and provides a window through which to explore glutamatergic neurotransmission in living individuals (Ametamey, 2006). [^{11}C]ABP688 is a negative mGluR5 allosteric modulator with high selectivity and affinity. Previous in vivo studies of [^{11}C]ABP688 PET in healthy subjects have confirmed postmortem data suggesting high variability of [^{11}C]ABP688 binding across brain regions, with high binding in known mGluR5-dense regions such as the striatum, the hippocampus, and the anterior cingulate cortex, in contrast to low binding in the thalamus and negligible binding in the cerebellum (Ametamey et al., 2007; Treyer et al., 2007). Yet, age and sex effects on mGluR5 availability remain unknown, as they have not been formally studied in healthy volunteers.

PET studies using specific radiopharmaceuticals have been a valuable tool for investigating sex effects in health and disease states. PET studies have provided evidence of sex effects in energy metabolism (Hu et al., 2013) and in the availability of a

number of neuroreceptors (Madsen et al., 2011). Although preclinical studies suggest an effect of sex on mGluR5-mediated behaviors (Grove-Strawser et al., 2010), the possibility of sex differences affecting mGluR5 availability in the human brain, until recently, had not been addressed due to the absence of female participants in most previous [^{11}C]ABP688 studies (Ametamey et al., 2007; Treyer et al., 2007; DeLorenzo et al., 2011a; Deschwanden et al., 2011; Hulka et al., 2014). A recent study of the association between [^{11}C]ABP688 binding and smoking suggests that non-smoking female controls had lower binding throughout the brain than male non-smokers (Akkus et al., 2013). However, sex differences in binding were not specifically assessed.

PET has also been instrumental in demonstrating age-related adaptations in brain neurochemistry, which may represent vulnerability to specific disease processes. In fact, some neurotransmitter systems remain stable during the aging process, while others show either downregulation (Moses-Kolko et al., 2011; Engman et al., 2012; Matuskey et al., 2012) or up-regulation (Fowler et al., 1997). Although no study has formally examined the effects of aging on [^{11}C]ABP688 binding, a lack of aging effects has been previously suggested (Deschwanden et al., 2011; Akkus et al., 2013; Hulka et al., 2014), with the caveat that only one study included subjects over 40 years of age (Deschwanden et al., 2011).

Assessment of aging effects cannot be dissociated from effects of age-related structural changes on PET outcome measures due to partial volume effects (PVE) (Erlandsson et al., 2012). While there are a number of methods proposed to recover the loss of PET signal due to age-related reduction in brain volumes, partial volume correction (PVC) is still a work in progress, particularly in the context of high-resolution

scanners (Uchida et al., 2011; Greve et al., 2014). The fact that [^{11}C]ABP688 binding is highly varied across brain regions further challenges the application of such corrections. The region-based voxel-wise (RBV) correction introduced by Thomas and collaborators represents an attractive PVC method for radiopharmaceuticals such as [^{11}C]ABP688 that display large variances in regional binding (Thomas et al., 2011). RBV has been shown to accurately correct for PVE in healthy controls and patients with Alzheimer's disease for PET imaging of amyloid-binding tracers (Thomas et al., 2011). An important consideration for RBV-PVC is the selection of regions of interest with homogenous radioactivity. In order to accurately correct for PVE while maintaining the regional variation present in [^{11}C]ABP688 binding, we incorporated tracer binding estimates obtained using MRI-based cortical morphology into the original RBV method.

In view of the chemoarchitectural organization of mGluR5 in the brain, we sought to report on the cortical distribution of [^{11}C]ABP688 binding using a fine surface and volume-based parcellation, with correction for PVE. In addition, we investigated whether binding in these regions is susceptible to age or sex effects.

3.4 METHODS

3.4.1 Subjects

Thirty-one healthy volunteers (age range20–77 years; men, n = 18, 45.3 ± 18.2 years; women, n = 13, 41.5 ± 19.6 years) were recruited via advertisements on the McGill University website and campus, as well as at the McGill Centre for studies in aging (Table 3.1). All subjects provided written informed consent prior to participation in the scanning sessions. Inclusion criteria required subjects to be healthy individuals

between 20 and 80 years of age. Exclusion criteria included (1) a personal or first-degree relative history of axis I psychiatric disorders, (2) present or past chronic use of medications, illicit drugs, or tobacco, (3) pregnancy, (4) breastfeeding, (5) history of neurological or medical disorders, and (6) MRI contraindications. The study was approved by the Montreal Neurological Institute Research Ethics Board and the Institutional Review Board of McGill University.

Age Group	N	Sex (M/F)	Handedness (R/L)	Weight (kg) (Avg ± SD)	Dose Injected (MBq) (Avg ± SD)
20-30	12	6/6	11/1	69.2 ± 12.4	366.3 ± 22.2
30-40	2	2/0	2/0	83.9 ± 8.3	358.9 ± 33.3
40-50	4	2/2	4/0	65.0 ± 9.0	340.4 ± 55.5
50-60	3	2/1	2/1	90.2 ± 7.3	344.1 ± 0.0
60-70	7	4/3	6/1	75.7 ± 13.2	351.5 ± 33.3
70-80	3	2/1	3/0	70.7 ± 11.0	362.6 ± 11.1

Table 3.1 Subject information. N number of subjects in each age group, M/F male/female, R/L right/left, kg kilograms, Avg±SD average ± standard deviation, MBq megabecquerel

3.4.2 PET acquisition and reconstruction

Synthesis of [^{11}C]ABP688 followed a procedure previously described in detail (Elmenhorst et al., 2010). All subjects were scanned in the Siemens high-resolution research tomograph (HRRT), which has approximately 2-mm full width at half maximum (FWHM) spatial resolution (Siemens–CTI, Knoxville, TN, USA). A transmission scan (6 min) was acquired for attenuation and scatter correction. [^{11}C]ABP688 was administered as a slow bolus injection through an intravenous line installed at the antecubital region, at a dose of 355.2 ± 29.6 MBq, with specific activity of 13.9 ± 6.3 GBq/μmol. Specific activity was not available for four subjects. Immediately following injection, a 1-h

dynamic emission scan was acquired in 3D list mode. A time-series of 3D images (frames) was reconstructed into 256 × 256 × 207 voxels (voxel side length of 1.21875 mm), using the ordinary Poisson version of the ordered subsets expectation maximization (OP-OSEM) algorithm (Hong et al., 2007). This ordinary Poisson version included full accounting for the normalization, attenuation, and time-dependent scatter and random events. Point spread function modeling was included in the OP-OSEM reconstruction (Comtat et al., 2008; Sureau et al., 2008). Subject head motion was corrected for using a modified data-based motion estimation method (Costes et al., 2009).

3.4.3 Binding potential analysis

Voxel-wise [^{11}C]ABP688 non-displaceable binding potentials (BP_{ND}) were estimated using the simplified reference tissue model with cerebellar grey matter as reference region (Gunn et al., 1997; Innis et al., 2007; Elmenhorst et al., 2010). [^{11}C]ABP688 BP_{ND} has high correspondence with k3/k4 kinetic constants ratio estimates using arterial input function in humans (Milella et al., 2011). BP_{ND} was calculated at the voxel level using parametric mapping of receptor–ligand binding with a basis function implementation (Lammertsma and Hume, 1996; Gunn et al., 1997).

3.4.4 MRI acquisition and analysis

A 3D T1-weighted MP RAGE [magnetization-prepared rapid gradient-echo] sequence (1 mm3 voxel size, 256 × 256 × 256 matrix; TE = 2.98; TR = 2300; TI = 900 ms; flip angle = 9°) was acquired for each subject using a Siemens Trio 3T scanner.

MRI data were analyzed with the FreeSurfer software package (www.surfer.nmr.mgh.harvard.edu, version 5.3), following the structural analysis pipeline that has previously been described in detail (Dale et al., 1999; Fischl et al., 1999a; Fischl et al., 2002). Briefly, the process includes intensity normalization, removal of the skull and non-brain tissue (Segonne et al., 2004), subcortical segmentation of grey and white matter structures (Fischl et al., 2002), and sub-voxel tessellation of the pial surface and grey matter/white matter boundary (subsequently referred to as the white matter surface) (Dale et al., 1999; Fischl et al., 1999a; Fischl et al., 2001; Segonne, 2007). Tessellation of the pial and white matter surfaces results in a mesh of approximately 300,000 vertices. The initial surface reconstruction was then manually inspected and corrected for errors due to incomplete removal of non-brain tissue or inadequate intensity normalization. At each vertex on the final white matter surface, cortical thickness was estimated as the closest distance from the white matter surface to the pial surface (Fischl and Dale, 2000). Based on the individual's cortical anatomy, the surface was then parcellated into 34 regions of interest per hemisphere using the Desikan-Killiany cortical atlas (Desikan et al., 2006).

3.4.5 PET-MRI integration

For each subject, boundary-based rigid-body registration was performed between the raw PET radioactivity averaged across time and the white matter surface (Greve and Fischl, 2009). Registration was visually inspected and adjusted when necessary to ensure accuracy. Following BP_{ND} analysis, values were sampled from the PET volume space to the reconstructed white matter surface (Greve et al., 2014). PET

images and BP_{ND} values were sampled halfway between the white matter and pial surfaces based on cortical thickness (Figure 3.1). Sampling from the middle of the cortex was performed to reduce partial volume error in the non-PVC data and to ensure consistency across analyses. For cortical vertex-wise analysis and visualization, BP_{ND} data was sampled to a standard surface and blurred at 10 mm FWHM.

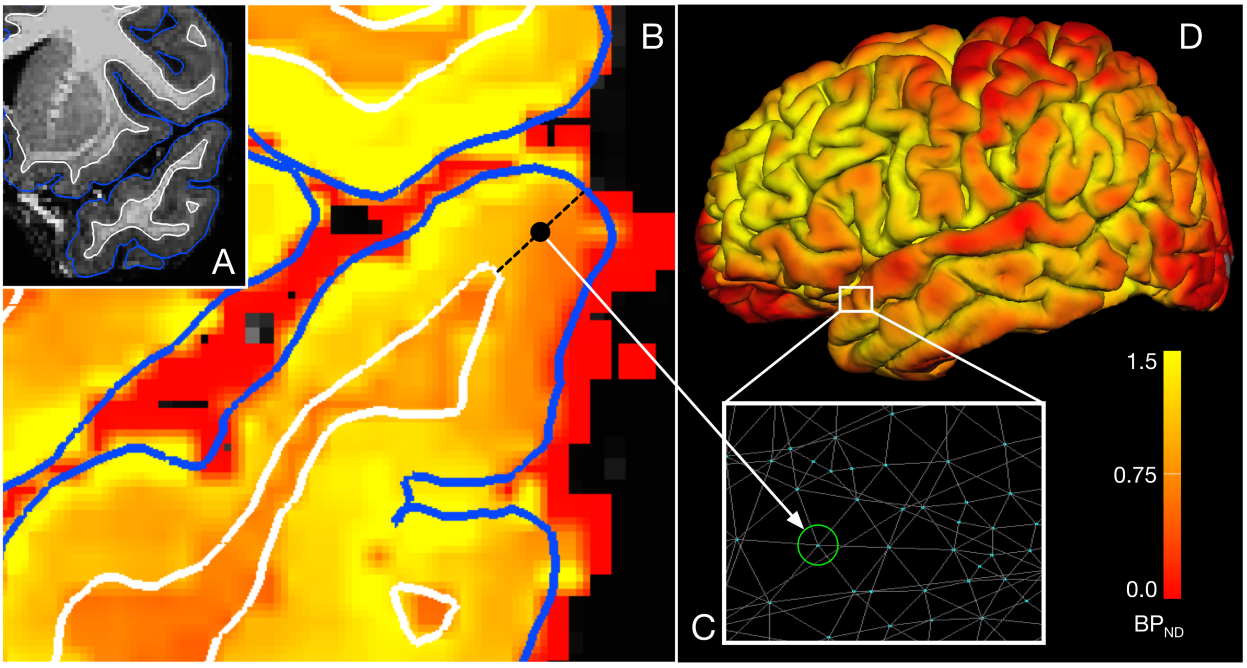

Figure 3.1 Simplified representation of volume-to-surface sampling method. (a) Left hemisphere shown in the coronal plane of a single subject's T1 MRI. (b) Enlarged view of the anterior portion of the temporal lobe. A white line denotes the white matter surface and a blue line denotes the pial surface. An RBV-PVC BP_{ND} image (in yellow-red color scale) is co-registered and superimposed over the T1 MRI. The black dotted line represents corresponding vertices, with the midpoint indicated by the black circular point. In this example, BP_{ND} values are sampled from the midpoint to the surface mesh. The vertex corresponding to the midpoint is denoted by the green circle on the magnified surface mesh (c). The smaller white box denotes the region of the anterior temporal lobe that the magnified surface mesh corresponds to. RBV-PVC BP_{ND} values for all vertices are shown on the lateral left hemisphere pial surface of the same subject (d).

3.4.6 Partial volume correction

BP_{ND} data in this study were corrected for PVE using two algorithms: the modified Muller-Gartner method (mMG-PVC) and a customized version of the RBV-

PVC method (Muller-Gartner et al., 1992; Rousset et al., 1998; Thomas et al., 2011). The mMG-PVC method uses a geometric transfer matrix to estimate the mean PET activity in the grey matter, white matter, and cerebral spinal fluid, as described previously (Muller-Gartner et al., 1992; Rousset et al., 2007). Tissue classification was performed with the New Segment tool in SPM8 (www.fil.ion.ucl.ac.uk/spm/software/spm8/) (Ashburner and Friston, 2005). In order to avoid noise amplification, the grey matter classification threshold was set at 20% (Rousset et al., 2007).

Our RBV-PVC implementation was designed to reduce the degree of binding inhomogeneity within cortical regions of interest by incorporating information about regional variances within each hemisphere (Figure 3.2). First, the raw dynamic PET frames were averaged across time and sampled to the surface mesh (Greve and Fischl, 2009). The PET vertex values were then blurred at 10 mm FWHM. Surface sampling and blurring allowed us to define regions of homogeneous radioactivity without increasing PVE. For each hemisphere, high, low, and mid-range clusters were defined by setting thresholds one standard deviation above and below the mean. The clusters were then sampled back to the subject's MRI volume space, and combined with segmented subcortical volumes (caudate, putamen, hippocampus, amygdala, thalamus, white matter, cerebellar white matter, cerebellar grey matter, cerebral spinal fluid, and other subcortical grey matter structures). All segmented cortical and subcortical volumes were then combined with the appropriate tissue classification. This segmented and classified volume atlas was then resampled to the subject's PET native space and processed using the geometric transfer matrix method to obtain the PVC PET values for

each region. RBV-PVC was performed on the resulting geometric transfer matrix values, as described by Thomas and colleagues (Thomas et al., 2011).

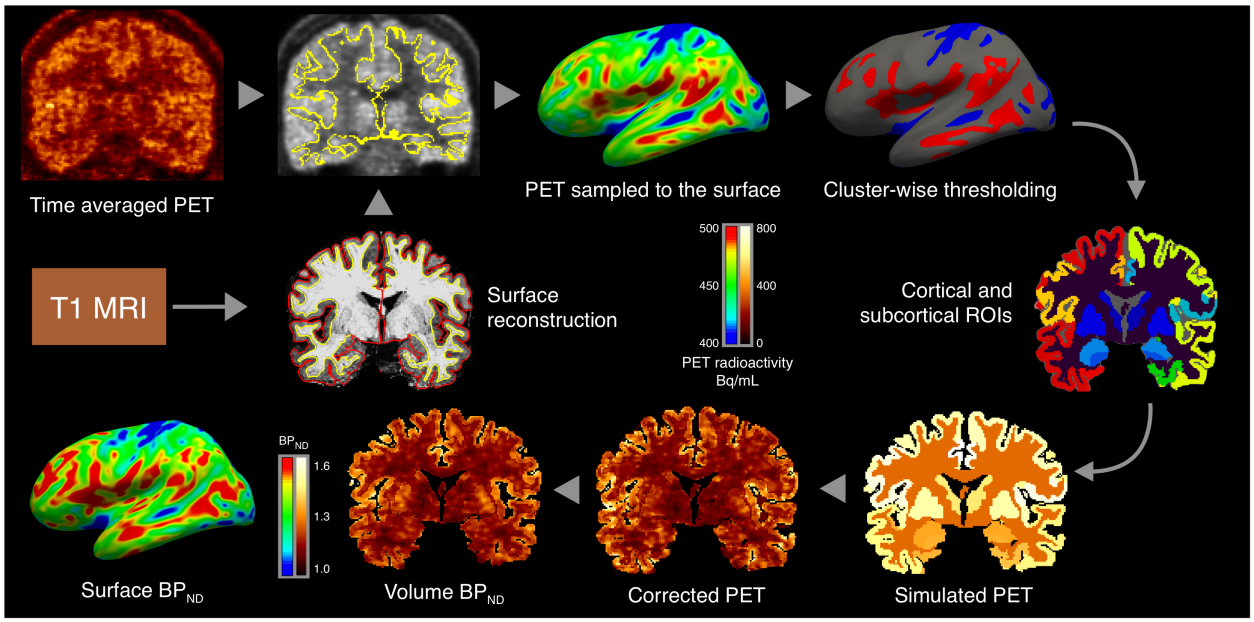

Figure 3.2 Customized RBV-PVC processing pipeline. Reconstruction of the white matter and pial surfaces displayed as yellow and red lines on the T1- MRI. The white matter surface (yellow line) co-registered to the time- averaged raw [^{11}C]ABP688 PET using boundary based registration. The raw [^{11}C]ABP688 PET is blurred at 10 mm FWHM and clustered using the mean and standard deviation. Surface clusters are sampled back to the volume space and combined with subcortical ROIs. The simulated PET displays the segmented volume, where values generated by the geometric transfer matrix are assigned to each ROI. RBV-PVC processing is then performed to create the corrected [^{11}C]ABP688 PET image. RBV-PVC BP_{ND} results are displayed in the volume and on the inflated pial surface, blurred at 10 mm FWHM.

3.4.7 Statistical analyses

Cortical BP_{ND} analysis was conducted in the surface space with the FreeSurfer software package using a vertex-wise general linear model. Multiple comparisons correction for the number of vertices was carried out with cluster-based Monte Carlo simulation. Separately, a general linear model was used to determine differences in average BP_{ND} between sexes and age groups for five segmented subcortical structures in each hemisphere (caudate, putamen, hippocampus, amygdala, thalamus). In

addition, we analyzed BP_{ND} averaged across the whole cortex. False discovery rate correction was used to control for multiple comparisons in the analysis of subcortical structures (Benjamini and Hochberg, 1995). The coefficient of variation was calculated at each vertex by dividing the population standard deviation by the mean. Lastly, the Spearman rank correlation was used to examine the relationship between non-PVC BP_{ND} and the two PVC methods (i.e., RBV-PVC and mMG-PVC). All statistical analyses and related figures were generated with the open-source statistical software R (R Core Team, 2013).

3.5 RESULTS

While participants ranged in age from 20 to 77 years, fewer subjects between the ages of 45 and 55 years were included (Table 2.1). As a result, the relationship between BP_{ND} and age in several regions of interest did not fit a linear model (Figure 3.3). Therefore, age was analyzed as both a continuous and a categorical variable. Subjects were grouped according to age as either less than or greater than the median of the population (i.e., 47 years). The younger group comprised 18 subjects (29.4 ± 7.8 years), while the older group included 13 subjects (63.5 ± 6.9 years).

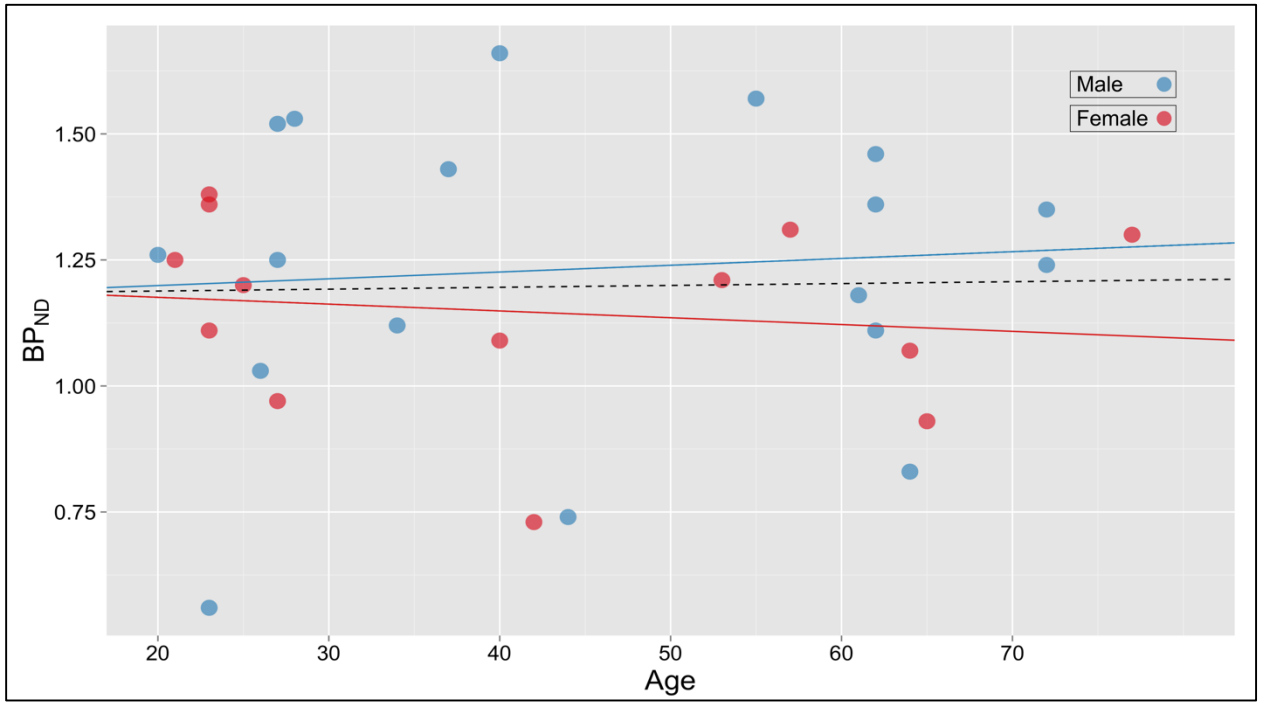

Figure 3.3 Correlation between average cortical RBV-PVC BP_{ND} and age. The correlation between age and RBV-PVC BP_{ND} averaged across all cortical surface vertices is shown for all male (blue) and female (red) participants. Separate blue and red regression lines display the relationship between RBV-PVC BP_{ND} and age for male and female participants, respectively. The dotted black line shows the relationship between RBV-PVC BP_{ND} and age for the combined group.

3.5.1 Age

No significant relationship was found between continuous age and non-PVC, RBV-PVC, or mMG-PVC BP_{ND} for any of the subcortical structures (results not shown). Continuous age was also not associated with BP_{ND} averaged across both hemispheres of the cortical surface for RBV-PVC (Figure 3.3), non-PVC, or mMG-PVC (results not shown). When separate age groups were compared, older subjects showed higher non-PVC BP_{ND} in the right amygdala, right thalamus, and left putamen (Table 3.2). However, these differences were not significant after multiple comparisons correction for the number of subcortical structures. RBV-PVC and mMG-PVC BP_{ND} showed no significant differences in subcortical regions (Table 3.2).

Vertex-wise analysis showed no regions where cortical BP_{ND} was associated with continuous age for non-PVC, RBV-PVC, or mMG-PVC. Age group analysis of vertex-wise RBV-PVC BP_{ND} showed one small cluster in the anterior cingulate cortex where younger subjects had higher BP_{ND} than older subjects. This cluster did not survive multiple comparisons correction for the number of vertices. Conversely, mMG-PVC vertex-wise analysis showed higher BP_{ND} in older subjects in the left superior parietal cortex and bilaterally in the frontal poles. These regions also did not survive multiple comparison correction for the number of vertices. Vertex-wise analysis of non-PVC BP_{ND} showed no significant differences between the age groups.

3.5.2 Sex

Cortical vertex-wise analysis of both RBV-PVC BP_{ND} and non-PVC BP_{ND} showed no significant clusters prior to multiple comparisons correction. mMG-PVC, on the other hand, showed several significant clusters in the left lateral prefrontal cortex, right insular cortex, right lateral superior frontal cortex, and the medial parietal cortex bilaterally where male participants had higher BP_{ND} than female participants. As with RBV-PVC BP_{ND} and non-PVC BP_{ND}, none of these clusters survived multiple comparisons correction. Furthermore, sex had no significant effect on BP_{ND} in any of the subcortical regions studied (Table 3.2).

		non-PVC			RBV-PVC			mMG-PVC		
Region		**F**	**P**	**D**	**F**	**P**	**D**	**F**	**P**	**D**
RH Thalamus	**Age**	4.483	0.043	0.779	1.916	0.177	0.513	0.817	0.374	0.332
	Sex	0.415	0.525	0.265	0.020	0.888	0.080	0.429	0.518	0.259
RH Caudate	**Age**	0.935	0.342	0.357	0.044	0.835	0.078	0.018	0.894	0.050
	Sex	0.139	0.712	0.157	0.000	0.983	0.013	0.144	0.707	0.143
RH Putamen	**Age**	2.271	0.143	0.551	0.377	0.544	0.227	0.319	0.577	0.198
	Sex	0.718	0.404	0.334	0.089	0.767	0.123	3.301	0.080	0.682
RH Hipp	**Age**	1.909	0.178	0.500	0.898	0.351	0.344	1.228	0.277	0.402
	Sex	1.335	0.258	0.444	1.151	0.292	0.412	1.135	0.296	0.411
RH Amygdala	**Age**	4.742	0.038	0.801	2.134	0.155	0.538	2.878	0.101	0.617
	Sex	0.389	0.538	0.258	0.344	0.562	0.241	1.090	0.305	0.405
LH Thalamus	**Age**	1.587	0.218	0.462	0.705	0.408	0.309	0.688	0.414	0.307
	Sex	0.504	0.484	0.283	0.353	0.557	0.236	0.009	0.925	0.017
LH Caudate	**Age**	1.323	0.260	0.421	0.000	0.996	0.002	0.021	0.886	0.053
	Sex	0.630	0.434	0.312	0.346	0.561	0.217	0.938	0.341	0.361
LH Putamen	**Age**	4.548	0.042	0.769	1.188	0.285	0.401	1.358	0.254	0.415
	Sex	1.542	0.225	0.472	0.332	0.569	0.233	2.348	0.137	0.581
LH Hipp	**Age**	2.544	0.122	0.588	0.736	0.398	0.316	1.200	0.283	0.404
	Sex	0.268	0.608	0.218	0.291	0.594	0.216	0.233	0.633	0.199
LH Amygdala	**Age**	3.722	0.064	0.709	0.681	0.416	0.303	2.904	0.099	0.618
	Sex	0.431	0.517	0.269	0.468	0.499	0.268	1.234	0.276	0.428

Table 3.2 Age and sex effects in subcortical structures. Rows correspond to each subcortical structure (thalamus, caudate, putamen, hippocampus [hipp], and amygdala) for the right hemisphere (RH) and left hemisphere (LH). For each subcortical structure, separate general linear models were run for age group (age) and sex. Columns display the Fisher's statistics (F), nominal p value (P), and Cohen's d estimate of effect size (D) for non-PVC, RBV-PVC, and mMG-PVC BP_{ND}. * indicates significance at the 5% level (uncorrected for multiple testing).

3.5.3 Partial volume correction

Over the whole cortex, mean RBV-PVC BP_{ND} was 10% higher and mMG-PVC BP_{ND} was 26 % higher than non-PVC BP_{ND}. The coefficient of variation over the whole

cortex was 0.22 for non-PVC BP_{ND}, and 0.21 and 0.26 for RBV-PVC and mMG-PVC BP_{ND} respectively. As shown in Figure 3.4, the vertex-wise coefficient of variation was more localized in mMG-PVC than RBV-PVC or non-PVC BP_{ND}. mMG-PVC showed a high degree of variation in the central and occipital cortices, which was much lower in the RBV-PVC and non-PVC BP_{ND}. There was also a high degree of variation for all PVC and non-PVC methods in the area surrounding the border of the cingulate cortex, which may be due to errors in registration or volume-to-surface sampling (Figure 3.4).

To determine the degree to which PVC alters general trends such as the distribution of subjects within the population, we examined the relationship between non-PVC and RBV-PVC compared to that of non-PVC and mMG-PVC BP_{ND} averaged across the whole cortex. While PVC alters the mean and standard deviation of BP_{ND} values, the distribution of subjects within the population should be preserved in relation to the non-PVC BP_{ND}. A stronger correlation was found between the subject order of non-PVC BP_{ND} and RBV-PVC BP_{ND} ($r=0.98$) than that of non-PVC BP_{ND} and mMG-PVC BP_{ND} ($r = 0.90$).

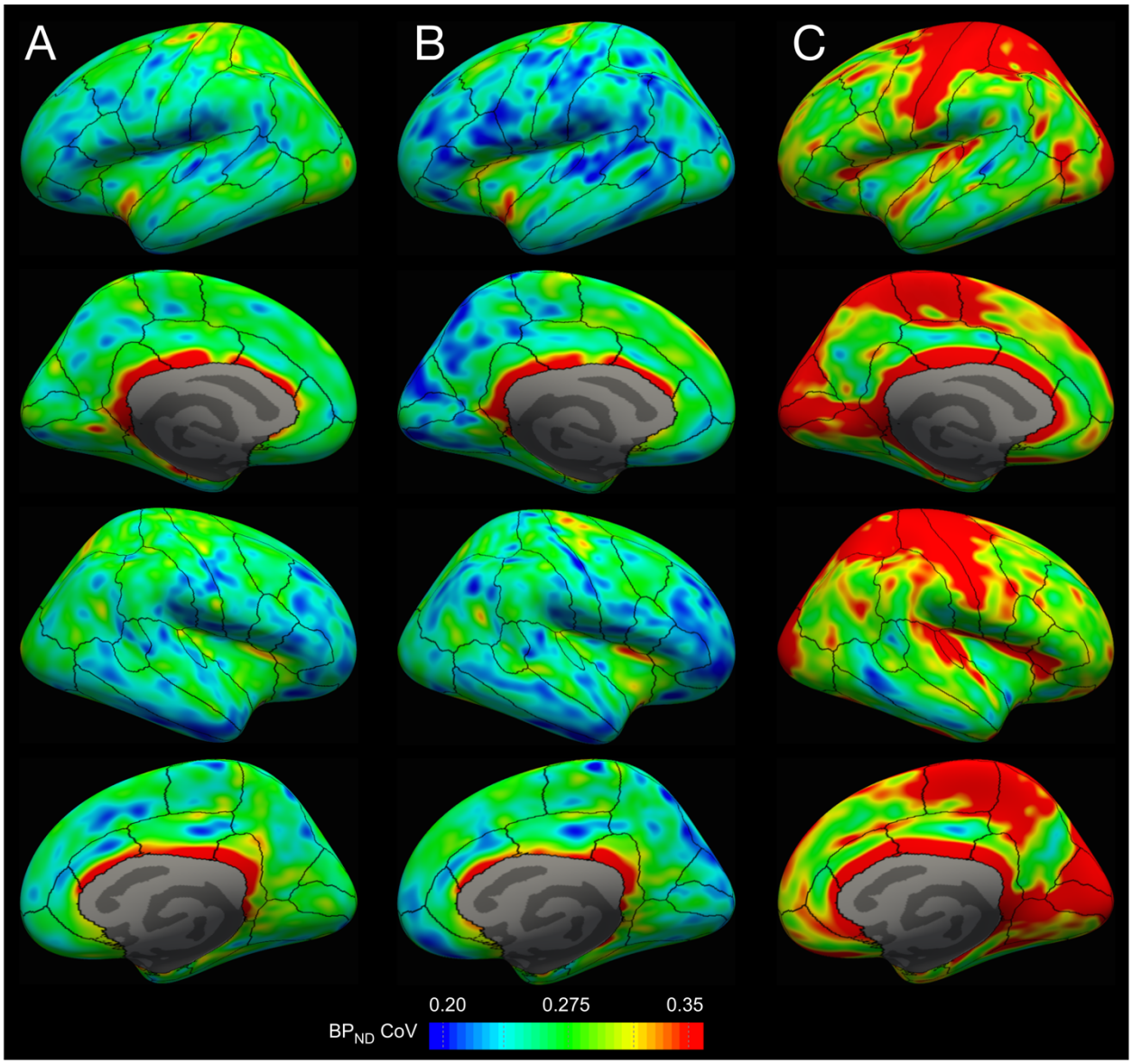

Figure 3.4 Effect of PVC on cortical distribution of the coefficient of variation. Lateral and medial views of the inflated pial surface are shown for the left and right hemispheres, with thin black lines delineating anatomical regions. The coefficient of variation was calculated at each vertex and smoothed at 10 mm FWHM. (a) Non-PVC BP_{ND}; (b) RBV-PVC BP_{ND}; (c) mMG-PVC BP_{ND}

3.5.4 Regional distribution

As RBV-PVC and non-PVC BP_{ND} showed high regional correspondence in the previous analysis, only RBV-PVC was used to assess the regional distribution. The highest BP_{ND} values were in the lateral prefrontal/inferior frontal cortex, the

anterior and posterior cingulate, and the supramarginal cortex. Moderately higher RBV-PVC BP_{ND} was observed in the left lateral prefrontal cortex, the left middle temporal gyrus, and the left supramarginal cortex relative to the same regions in the right hemisphere (Figure 3.5a). The lowest BP_{ND} values were found in the pre- and post-central cortices, the cingulate isthmus, the occipital lobes, and the thalami (Figure 3.5b). Among the 39 cortical and subcortical regions compared, no significant inter-hemispheric differences were found in average RBV-PVC BP_{ND} (Figure 3.5b). The coefficient of variation of cortical RBV-PVC BP_{ND} was highest in the medial superior frontal cortex, the central cortex, the insula, and the cingulate isthmus.

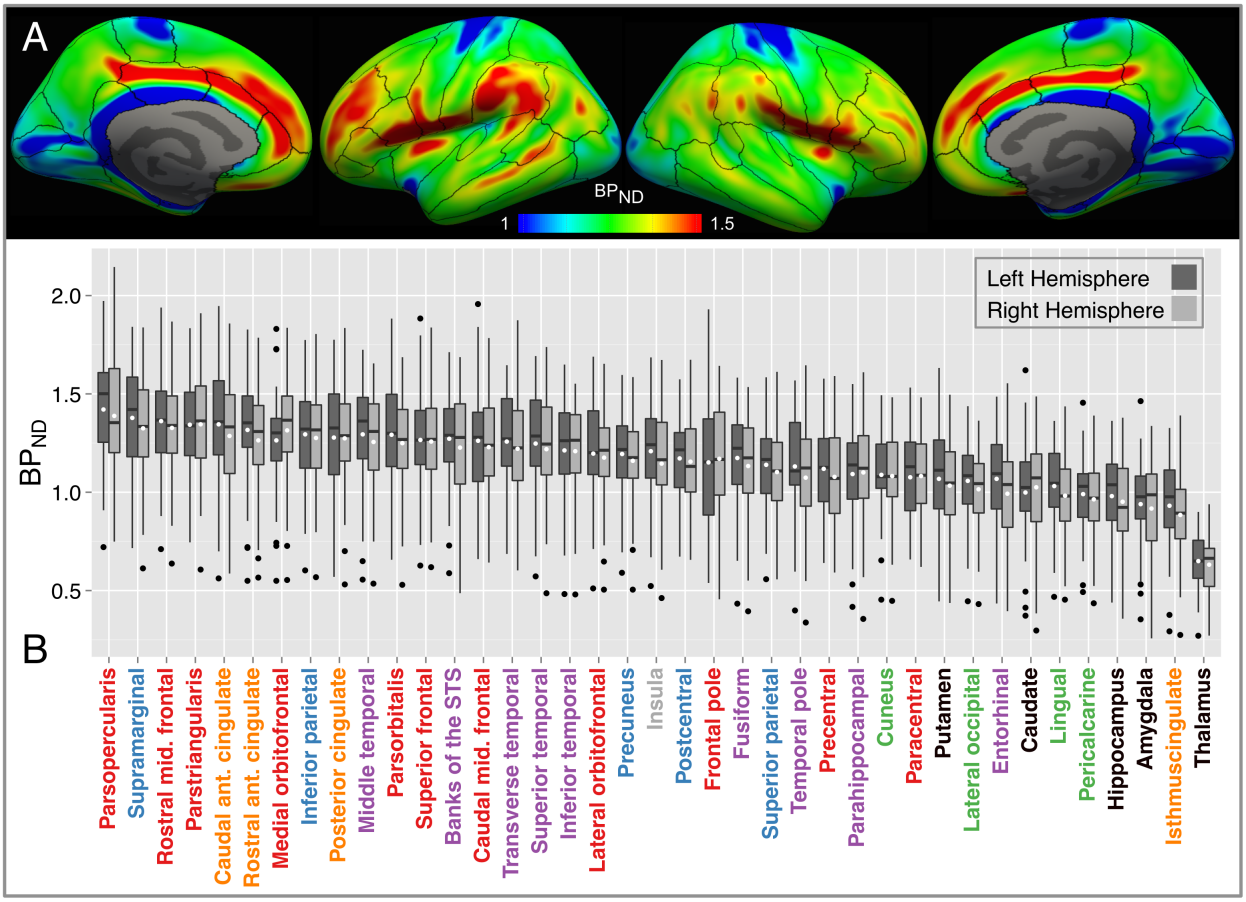

Figure 3.5 Cortical and subcortical distribution of RBV-PVC BP_{ND}. (a) Cortical RBV-PVC BP_{ND} averaged across subjects, and smoothed at 10 mm FWHM. RBV-PVC BP_{ND} data is visualized on the inflated cortical surface and overlaid by outlines of the 34 anatomical cortical regions (delineated by thin black lines). (b) Box plots for the distribution of RBV-PVC BP_{ND} within 34 cortical and five subcortical regions. The box-plot whiskers extend to the highest and lowest data point within 1.5 times the interquartile range, as described by Tukey [48]. The white dots in the box plot represent the group mean for each structure. Structures are ordered based on the average RBV-PVC BP_{ND} of the combined hemispheres, with higher values displayed on the left.

3.6 DISCUSSION

In the present study, we characterized in vivo mGluR5 availability in healthy subjects with high-resolution [^{11}C]ABP688 PET imaging using an automated cortical segmentation algorithm. Refining cortical regions using cortical-based segmentation allowed us to reappraise [^{11}C]ABP688 regional distribution and to better assess age and sex effects, which remained undefined from prior studies. The present analysis revealed no age or sex effects of regional [^{11}C]ABP688 binding in healthy individuals.

Our fine parcellation in cortical areas expanded previous concepts regarding human mGluR5 chemoarchitecture. We observed large cortical heterogeneity of [^{11}C]ABP688 binding, with association cortices showing high [^{11}C]ABP688 BP_{ND}, and primary motor/sensory regions showing low binding. Our results revealing low mGluR5 availability in the pre- and post- central cortices are a feature not previously described by in vivo PET or by animal studies. In fact, the detailed parcellation of the frontal and temporal regions employed in this study has allowed us to refine current concepts regarding mGluR5 cortical distribution. Previous studies had reported higher mGluR5 availability in temporal versus frontal regions in analysis of large frontal and temporal regions of interest (Ametamey et al., 2007; Treyer et al., 2007; DeLorenzo et al., 2011a). In contrast, we show that most frontal cortical regions displayed higher [^{11}C]ABP688 binding than most temporal cortical areas. Such detailed parcellation and

vertex-wise analysis may be advantageous for investigating mGluR5 abnormalities in disease states.

One could speculate that the mGluR5 chemoarchitectural features seen here are related to variations in dendritic branching and spine density of distinct cytoarchitectural cortical areas (Elston, 2002; Elston and Rockland, 2002). While dendritic density is not directly related to mGluR5 availability, mGluR5 is located primarily on the dendritic spines and shafts of pyramidal neurons (Romano et al., 1995; Niswender and Conn, 2010). As mGluR5 is known to play a role in learning and memory through regulation of long-term potentiation and long-term depression, it is possible that regions with high mGluR5 availability are those where a greater degree of synaptic plasticity is found (Hermans and Challiss, 2001; Waung and Huber, 2009).

mGluR5 availability in subcortical structures has been well described in animal studies, where the striatum, hippocampus, and amygdala were shown to be mGluR5-rich compared to the thalamus and cerebellum (Romano et al., 1995). The highest subcortical BP_{ND} values in our study were observed in the putamen, followed by the caudate, hippocampus, and amygdala. The lowest BP_{ND} values, including all cortical regions, were found in the thalami.

The present results refute the presence of significant sex-related mGluR5 differences in healthy individuals. Our results contrast with those of Akkus et al., who observed that [^{11}C]ABP688 binding was lower in non-smoking females than males (Akkus et al., 2013). Although [^{11}C]ABP688 binding indicates similar availability of mGluR5 allosteric binding sites in males and females, this does not necessarily preclude sex differences in receptor function, regulation, or downstream effects, or of

different involvement in disease processes between males and females (Akkus et al., 2013). As such, the absence of sex differences reported here can be reconciled with preclinical literature suggesting sex-related functional changes in mGluR5 (Grove-Strawser et al., 2010) and sex-related changes in tissue glutamate concentrations measured by MRI spectroscopy in humans (Sailasuta et al., 2008; Hadel et al., 2013).

Our results support the concept that mGluR5 availability remains stable during the aging process. First, we found no effects of age on [^{11}C]ABP688 cortical binding. Second, the effects observed on the right amygdala, right thalamus, and left putamen were weak and did not survive multiple comparisons correction. Interestingly, and supporting our present results, Tsamis and collaborators (Tsamis et al., 2013) found that the number of striatal medium spiny neurons mildly immunoreactive for mGluR5 was increased in older individuals (Tsamis et al., 2013). Higher mGluR5 expression has been found in the cortex of patients with Lewy body disease and Parkinson's disease as well as epilepsy (Notenboom et al., 2006; Price et al., 2010).

Despite reports in the MR spectroscopy literature that age-related changes in glutamate brain concentrations might occur (as either increases or decreases, depending on the brain region being considered (Sailasuta et al., 2008; Hadel et al., 2013)), there is a growing body of evidence suggesting that mGluR5 stability is associated with successful aging. This construct is supported by preclinical work in aging rodents and via genetic or pharmacological mGluR5 manipulation in aged animals and human studies of dementia populations (Car et al., 2006; Price et al., 2010; Menard and Quirion, 2012; Leuzy et al., 2015).

Although we utilized high-resolution PET imaging, we found that correction for

PVE by our data-driven RBV approach improved [^{11}C]ABP688 BP_{ND} findings and outperformed the widely used mMG-PVC method. mMG-PVC showed greater variation than RBV-PVC and non-PVC in several localized regions (Figure 3.4). These results contrast with those of a previous study of a serotonin-4 receptor radioligand ([11C]SB207145), which used similar surface-based analyses and high-resolution imaging, but which showed no significant increase in variance with mMG-PVC (Greve et al., 2014). mMG-PVC assumes homogeneity within the white matter, grey matter, and cerebral spinal fluid tissue compartments, and therefore may be biased by inaccuracies in tissue classification. Reduced grey matter concentration or blurring of the grey–white matter junction due to age or pathology could increase PVE, resulting in an underestimation of the radioactivity in the grey matter relative to the surrounding tissue. The assumption of homogeneity is also not valid for all radioligands. For example, patients with Alzheimer's disease show as much as 50% less binding in the occipital grey matter as in the frontal grey matter for the Aβ radioligand [18F]flutemetamol (Thomas et al., 2011). The large regional variation in [^{11}C]ABP688 binding across cortical areas rendered mMG-PVC less well suited for our analyses, as it does not account for spillover effects between adjacent cortical regions.

Previous studies of both RBV-PVC and mMG-PVC have reported increased variation over uncorrected data, which has been suggested to represent true variation in the signal (Thomas et al., 2011; Greve et al., 2014). However, this increase in variation may be due, in part, to inadequate delineation of regions with homogeneous radioactivity. Previous implementations of RBV-PVC selected cortical regions of interest based on clinical relevance, relationship to a particular disease, or known tracer

distribution (Rousset et al., 2008; Thomas et al., 2011). In contrast, by thresholding [^{11}C]ABP688 radioactivity values sampled to the cortical surface, our data-driven approach attempted to delineate cortical regions based on differences in tracer uptake. While some error was introduced due to volume-to-surface sampling, surface analysis allowed us to smooth and cluster the data without introducing more PVE. While we used the mean and standard deviation to cluster tracer uptake data, future studies may consider applying more sophisticated clustering methods such as k-means clustering, provided that the matrix does not become ill conditioned.

Reference tissue methods for calculating BP_{ND} require a region with negligible specific binding of the radioligand to the receptor. We have validated the cerebellar grey matter as a suitable reference region for [^{11}C]ABP688 (Elmenhorst et al., 2010; Milella et al., 2011). Subsequent postmortem tissue assessment conducted by Deshwanden and colleagues using western blots revealed negligible mGluR5 protein expression in the human cerebellum (Deschwanden et al., 2011). On the other hand, two of three in vivo competition studies using [^{11}C]ABP688 and blocking agents, both administered in bolus injections, claimed an effect in the cerebellum when the entire cerebellum time-activity curves were computed as input function (DeLorenzo et al., 2011b; Kagedal et al., 2013; Mathews et al., 2014). However, the use of the entire cerebellum must be exercised with caution, given species differences and significant mGluR5 expression found in the human deep cerebellar nuclei (Daggett et al., 1995; Patel et al., 2007).

[^{11}C]ABP688 BP_{ND} may be vulnerable to fluctuations in extracellular concentrations of glutamate [67–69]. While it is improbable that the binding changes described are attributable to direct glutamate competition, age-related changes affecting extracellular

glutamate concentrations could have affected the results of this study.

In conclusion, high-resolution imaging and detailed segmentation of cortical and subcortical regions were shown to better describe the complex mGluR5 chemoarchitectural features in humans than previous approaches. Based on a larger series of healthy female and male subjects than in any previous study with [^{11}C]ABP688 PET, our results indicate little or negligible age and sex effects on [^{11}C]ABP688 binding. Finally, RBV-PVC seems to be better suited for quantifying [^{11}C]ABP688 binding, because it produces less variability than mMG-PVC. The present results highlight complexities underlying brain adaptations during the aging process, and support the notion that certain aspects of neurotransmission remain stable during the entire adult life span.

Chapter 4

mGluR5 cortical abnormalities in focal cortical dysplasia identified in vivo with [^{11}C]ABP688 PET Imaging

---

This work was published in:
Cereb Cortex, 2016, 26:4170-4179

4.1 PREFACE

In the previous study, we developed a novel partial volume correction method and described in detail the regional distribution of mGluR5 availability in the cortex and subcortical structures of healthy controls. In addition, our results suggest that mGluR5 availability was stable across the adult healthy lifespan and between sexes. In the current study, we build upon the prior findings by comparing mGluR5 availability between healthy controls and patients with FCD. While surgical specimens resected from patients with FCD have shown increased mGluR5 immunoreactivity in dysplastic and heterotopic neurons (Aronica et al., 2003), it remains unknown if mGluR5 abnormalities can be identified *in vivo* and if they are specific to the cortical lesion. Here, we performed the first whole-brain *in vivo* analysis of mGluR5 availability in patients with FCD, using [^{11}C]ABP688 PET. In patients who underwent surgical resection, we also assess mGluR5 immunoreactivity and histopathological features.

4.2 ABSTRACT

Metabotropic glutamate receptor type 5 abnormalities (mGluR5) have been described in tissue resected from epilepsy patients with focal cortical dysplasia (FCD). To determine if these abnormalities could be identified in vivo, we investigated mGluR5 availability in 10 patients with focal epilepsy and an MRI diagnosis of FCD using positron emission tomography (PET) and the radioligand [^{11}C]ABP688. Partial volume corrected [^{11}C]ABP688 binding potentials (BP_{ND}) were computed using the cerebellum as a reference region. Each patient was compared to homotopic cortical regions in 33 healthy controls using region-of-interest (ROI) and vertex-wise analyses. Reduced [^{11}C]ABP688 BP_{ND} in the FCD was seen in 7/10 patients with combined ROI and vertex-wise analyses. Reduced FCD BP_{ND} was found in 4/5 operated patients (mean follow-up: 63 months; Engel I), of whom surgical specimens revealed FCD type IIb or IIa, with most balloon cells showing negative or weak mGluR5 immunoreactivity as compared to their respective neuropil and normal neurons at the border of resections. [^{11}C]ABP688 PET shows for the first time in vivo evidence of reduced mGluR5 availability in FCD, indicating focal glutamatergic alterations in malformations of cortical development, which cannot be otherwise clearly demonstrated through resected tissue analyses.

4.3 INTRODUCTION

Focal cortical dysplasia, a common cause of drug-resistant epilepsy, is histologically characterized by cortical dyslamination and presence of dysmorphic neurons, including balloon cells (Taylor et al., 1971; Blumcke et al., 2011). Lineage marker protein expression studies in FCD specimens indicate that balloon cells derive

from the radial glial progenitor cells in the telencephalic ventricular zone, most carrying a glutamatergic, and therefore excitatory, neurochemical phenotype (Lamparello et al., 2007).

Metabotropic glutamate receptor type 5 (mGluR5) is a post-synaptic G-protein coupled receptor that mediates neuronal excitability (Conn and Pin, 1997; Anwyl, 1999). mGluR5 plays a key role in cortical development, neurogenesis, cell survival, and regulation of morphogenesis (Catania et al., 2007). In addition, several lines of evidence support a role of mGluR5 in epileptogenesis. mGluR5 downregulation has been described after amygdala kindling and in the pilocarpine mesial temporal lobe epilepsy models (Akbar et al., 1996; Kirschstein et al., 2007). A serial [^{11}C]ABP688 positron emission tomography (PET) study in pilocarpine-treated rats demonstrated binding changes during the silent period (i.e., epileptogenesis), with pronounced and diffuse reduction of binding following status epilepticus that resolved in all locations except in the hippocampi, as seizures develop in these regions (Choi et al., 2014). The observation of an anticonvulsant effect from mGluR5 antagonism and initiation of persistent epileptiform activity from mGluR5 agonism further indicate an underlying mechanism modulated by this receptor in epileptogenesis, which may contribute to the intrinsic epileptogenicity attributed to malformations of cortical development (Palmini et al., 1995; Chassoux et al., 2000; Merlin, 2002; Catania et al., 2007; Bianchi et al., 2009a).

Whereas surgical specimens resected from patients with FCD show mGluR5 abnormalities in dysmorphic neurons and balloon cells (Aronica et al., 2003), it remains unclear whether such abnormalities can be identified in vivo. In addition, as with any

information obtained exclusively through resected tissue, it is unknown whether mGluR5 abnormalities could be a diffuse cortical characteristic of patients with FCD or limited within the boundaries of the epileptogenic lesion.

Therefore, our primary goal was to investigate in vivo mGluR5 abnormalities in patients with FCD using [^{11}C]ABP688, a PET tracer that binds selectively to the mGluR5 allosteric site allowing whole brain imaging of its availability (Ametamey et al., 2007; Treyer et al., 2007). Demonstrating the possibility to detect mGluR5 abnormalities in vivo could have important clinical implications not only for diagnosis of malformations of cortical development as an underlying cause of seizures (i.e., finding occult or subtle lesions not clearly depicted through anatomical imaging) but also as a biomarker for future pharmacological interventions through identification of populations at higher risk for acquired epilepsies, in whom halting of epileptogenesis and prevention of epilepsy could be attempted.

In order to ensure accurate comparisons between the FCD lesion and healthy cortex, we developed a surface-based analysis with a data-driven partial volume correction method. This method has been instrumental for identifying regional differences related to mGluR5 availability in cortical and subcortical structures (DuBois et al., 2016b) and to ensure accurate comparisons across FCD and healthy tissue accounting for location, magnitude, and extent of abnormalities. Furthermore, here we provide information about cortical mGluR5 immunoreactivity for patients who underwent surgical resection and to whom surgical specimens are available for analysis.

4.4 METHODS

4.4.1 Subjects

We studied 10 patients with focal epilepsy and an MRI diagnosis of FCD investigated at the Montreal Neurological Hospital (Table 4.1). Five patients underwent surgery and had pathological diagnosis of FCD type IIb or type IIa. Four operated patients are currently seizure-free (Engel I, mean follow-up, 5 years and 9 months, Table 4.1), while the fifth patient experienced recurrent seizures (Engel II) and relocated medical care 1.5 years ago, at which point follow-up information became unavailable.

Thirty-three healthy subjects (range = 20–77y/o; males, n = 18, 47.4 ± 17.7 y/o; females, n = 15, 46.2 ± 18.9 y/o) were recruited via university advertisements. Exclusion criteria included: personal or first-degree relative history of axis I psychiatric disorders, chronic use of CNS active medications or illicit drugs, pregnancy/breastfeeding, present or past cigarette usage, history of neurological or medical disorders, and MRI contraindications. The study was approved by the Montreal Neurological Institute Research Ethics Board. All subjects provided written informed consent prior to participation in the study.

Patient	Age	Sex	FCD location	Last sz prior to scan (days)	AEDs	Age at sz onset / duration of epilepsy (years)	Surgery follow-up (years) Engel class	Pathology	PET Scanner
1	39	F	L lateral frontal	180	LEV, LMT, CLB, CBZ	3 / 36	no	N/A	HR+
2	56	M	R mesial parietal /posterior cingulate	1	CBZ, LEV, CLB	8 / 48	6y, Engel I	FCD IIb	HR+
3	25	M	R superior temporal	4	CBZ	8 / 17	6y9m, Engel I	FCD IIb	HRRT
4	20	F	L superior temporal	1	CLB	14 / 6	no	N/A	HRRT
5	19	F	R parahippocampal	11	VA, LEV, PB	15/4	6y11m, Engel II	FCD IIa	HR+
6	31	F	L posterior cingulate /mesial parietal	1	LMT, DPH, CLB	16 / 15	No	N/A	HR+
7	39	F	L mesial orbitofrontal	30	None (LMT discontinued at admission)	34 / 5	no	N/A	HR+
8	29	M	R frontal pole	1	VA, OXC, CLB	0.4 / 29	4y3m, Engel I	FCD IIb	HRRT
9	41	F	L posterior fusiform gyrus	6	LMT, PB, CLB	12 / 29	no	N/A	HR+
10	38	M	R inferior frontal	1	CBZ, CLB	17 / 21	5y1m, Engel I	FCD IIb	HRRT

Table 4.1 Clinical information. F: female; M: male; L: left; R: right; sz: seizure; AED: antiepileptic drug; LEV: levetiracetam, LMT: lamotrigine; CBZ: carbamazepine; CLB: clobazam; DPH: diphenylhydantoine; VA: valproic acid; OXC: oxcarbazepine; PB: phenobarbital

4.4.2 PET acquisition and reconstruction

[^{11}C]ABP688 was synthetized using the same methodology as in our previous studies (Elmenhorst et al., 2010; DuBois et al., 2016b). [^{11}C]ABP688 was administered as a slow bolus injection through an intravenous line at the antecubital region (injected dose/activity = 356.7 ± 25.2MBq; specific activity = 13.6 ± 6.3 GBq/μmol, unavailable for 10 of the controls). Immediately following injection, a 1-h dynamic emission scan was acquired in 3D list mode.

Six patients and 7 controls were scanned in the Siemens ECAT EXACT HR+ scanner [approximate resolution, 6 mm full width at half maximum (FWHM)]. The remaining subjects (4 patients, 26 controls) were scanned with the Siemens High Resolution Research Tomograph (HRRT, approximate resolution of 3 mm FWHM).
After correction for attenuation, scatter, and decay, data were reconstructed by filtered back-projection. The reconstructed time-series was 128 × 128 × 63 voxels (2.45 mm pixels) for the HR+ and 256 × 256 × 207 voxels (1.21875 mm pixels) for the HRRT.

To combine data from both scanners, the HRRT images were blurred with an anisotropic Gaussian kernel of 5.7 × 5.7 × 6.7 mm FWHM, based on findings from an in-house phantom study (unpublished data). The anisotropic Gaussian kernel used here was similar to previously published methods using an isotropic Gaussian kernel of 6 mm FWHM (van Velden, 2009).

4.4.3 MRI acquisition and analysis

As described previously in DuBois et al. (2016b), a 3D T1- weighted MPRAGE sequence (1 mm3 voxel size, 256 × 256 × 256 matrix; TE = 2.98; TR = 2300; TI = 900

ms; flip angle = 9) was acquired for each subject using a Siemens Trio 3 T scanner. MRI data were analyzed with FreeSurfer (www.surfer.nmr.mgh. harvard.edu, version 6.0 beta) (Dale et al., 1999; Fischl et al., 1999a), in order to perform subvoxel reconstruction of the pial surface and gray matter/white matter boundary (i.e., the white matter surface). The initial surface reconstruction was then manually inspected and corrected for errors due to incomplete removal of non-brain tissue or inadequate intensity normalization. At each vertex on the final white matter surface, cortical thickness was estimated as the closest distance between the white matter surface to the pial surface (Fischl and Dale, 2000). The subject surface was registered to symmetric and asymmetric average templates for subsequent analysis and visualization (Fischl et al., 1999b; Greve et al., 2013).

Boundary-based rigid-body registration was utilized to accurately align the MRI and the time-averaged raw PET images by fitting the white matter surface to the maximum of the radioactivity gradient (Greve and Fischl, 2009). Each subject's registration was visually inspected and manually adjusted when necessary. Using the cortical thickness information, PET data were then sampled from the middle of the cortex, halfway between the white matter and pial surfaces (Greve et al., 2014; DuBois et al., 2016b).

Correction for partial volume error was performed using a data-driven, region-based per-voxel partial volume correction method, as described in DuBois et al. (2016b). First, time-averaged raw PET data were sampled to the surface and blurred at 10 mm FWHM (Greve et al., 2014). For each hemisphere, high, low, and mid-range clusters were created by setting thresholds one standard deviation above and below the

mean radioactivity. Clusters were defined as a set of continuous vertices within the threshold range and with a surface area greater than 200 mm2 (DuBois et al., 2016b). These cortical regions were then sampled back to the subject's MRI volume space and combined with subcortical gray and white matter segmentations (Desikan et al., 2006). The geometric transfer matrix method was used to obtain the partial volume corrected PET values for each region (Rousset et al., 1998). The resulting values were then used to perform per-voxel correction for the whole brain (Thomas et al., 2011).

4.4.4 Binding potential analysis

Following PVC, [^{11}C]ABP688 non-displaceable binding potentials (BP_{ND}) were estimated using the simplified reference tissue model (with the cerebellar gray matter as reference region) and a basis function implementation of voxel-wise parametric mapping (Lammertsma and Hume, 1996; Gunn et al., 1997; Innis et al., 2007; Elmenhorst et al., 2010). Despite the presence of mGluR5 in the cerebellar cortex, several lines of evidence indicate that specific [^{11}C]ABP688 binding in the cerebellar cortex is negligible, including in vitro and in vivo imaging of [^{11}C]ABP688 binding in humans and animals (Elmenhorst et al., 2010; Milella et al., 2011), and human postmortem analysis of mGluR5 mRNA (Daggett et al., 1995) and protein expression (Deschwanden et al., 2011).

4.4.5 FCD manual labeling procedure

Three labels were created for each patient to encompass the lesion, as well as the perilesional and contralateral cortex in relation to the lesion (Figure 4.1). The "FCD

label" was manually traced along the white matter surface representation in volume space using each patient's MRI. Characteristics such as cortical thickness, blurring of the gray/white matter junction, and abnormal gyrification were used to estimate the extent of the lesion. When available, the clinical T2-weighted MRI was also utilized. All tracings were reviewed and corrected, when needed, by an experienced epileptologist. Each labeled voxel was assigned to the nearest white matter surface vertex. An automatic topological closing operation was used to fill any holes created by gaps in the volume label or the sub-voxel resolution of the surface. The "perilesional label" was created to account for the possibility of lesions extending beyond the MRI-visible abnormalities, by dilating each surface lesion label by approximately 10 mm in all directions followed by subtraction of the FCD label area. The "contralateral lesion label" was created by sampling the surface lesion label to the contra-lateral surface using average symmetrical atlas. This surface-based approach was used to ensure that the contralateral lesion label was sampled to the appropriate cortical anatomy (Greve et al., 2013).

4.4.6 Statistical analyses

Vertex-wise group comparisons of BP_{ND} were conducted in the average surface space using the FreeSurfer software package. Once sampled to the surface, BP_{ND} images were blurred at 5 mm FWHM and 2-tailed Z-tests were computed between each patient and the entire control group. Multiple comparisons correction for the number of vertices was carried out with a cluster-based Monte Carlo simulation (cluster-wise $P < 0.05$) (Hagler et al., 2006). In order to assess the distribution of extralesional vertex-

wise findings, we calculated the Euclidian distance along the cortical surface originating from the maximum vertex within the extralesional cluster and the nearest edge of the lesion label.

Z-tests were used to determine differences between average BP_{ND} within a given region-of-interest (ROI) for each patient and homotopic areas in the control group. Based on the results of the vertex-wise analysis, Z-scores were converted to one-tailed P-values for false discovery rate correction for multiple comparisons (Benjamini et al., 2006). Analyses and figures were generated with the R statistical software package (R Core Team).

4.4.7 *Surgical specimens analysis*

FCD was confirmed based on the presence of cortical dyslamination and dysmorphic neurons with balloon cells (Type IIb) or without balloon cells (Type IIa) (Blumcke et al., 2011) using formalin-fixed paraffin-embedded tissue from surgery (Blumcke et al., 2011). Neuropathology protocol included immunostaining for neuronal nuclear antigen NeuN, MAP2, synaptophysin, glial fibrillary acidic protein GFAP, Nissl (Luxol Fast Blue/Cresyl Violet), and Bielschowsky stainings.

mGluR5 staining (anti-mGLUR5 C-terminus antibody, Millipore Chemicon 06–451, 1:100) was performed in 5 µm slices adjacent to those used for clinical diagnosis. Immunohistochemistry was performed on a Benchmark XT stainer (Ventana Medical System): after deparaffinization, sections were pretreated with cell conditioning 1 buffer, the primary antibody was applied for 32 min and the Ultraview DAB kit was used. Slides were digitalized using an Aperio scan-scope system and image analysis was performed

using Spectrum software.

A descriptive qualitative analysis of mGluR5 immunostaining was conducted (Aronica et al., 2003). Cells (balloon cells, dysmorphic neurons and normal neurons) and neuropil were visually analyzed and rated for the immunoreactivity pattern as negative, mild, moderate, and strong (Aronica et al., 2003).

4.5 RESULTS

4.5.1 Vertex-wise analysis of [^{11}C]ABP688 BP_{ND}

Reduced BP_{ND} was found within the lesion in 8/10 patients, which remained significant in 6 patients after cluster-wise correction for multiple comparisons (see Figure 4.1; Table 4.2). No patients showed clusters of increased BP_{ND} within the lesion. Eight out of 10 patients showed a median of 3 extralesional areas of increased or decreased BP_{ND}, which were diffusely scattered throughout the ipsilateral and contralateral cortices (Figure 4.2). These extralesional clusters were mainly found in 3 patients, at variable distance from the lesion (Figure 4.2). Although the HRRT PET data were blurred to match the HR+ resolution, extralesional BP_{ND} abnormalities were more frequent in patients imaged with the HR+ scanner.

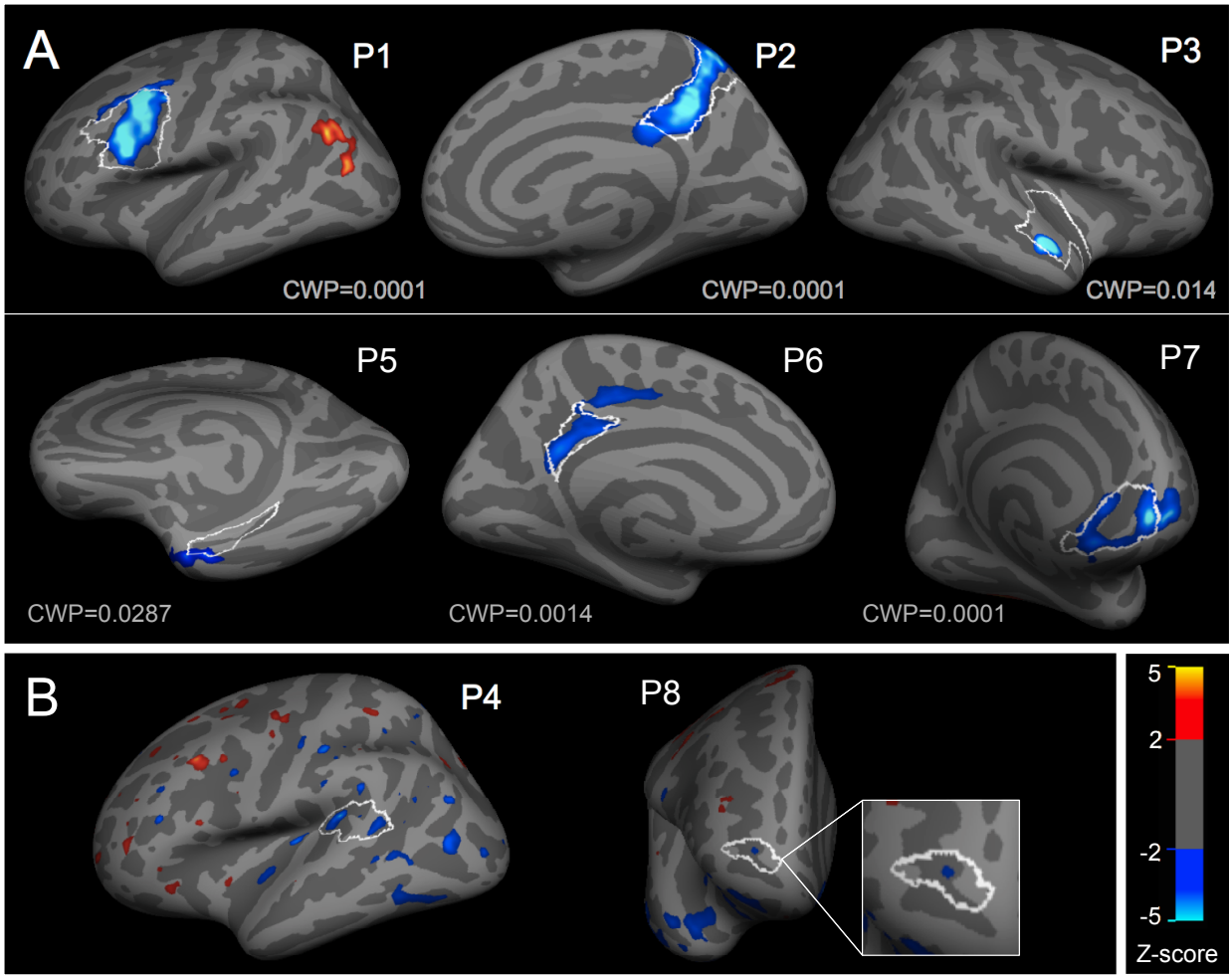

Figure 4.1 Vertex-wise [^{11}C]ABP688 BP_{ND} patient maps. Individual vertex-wise z-score maps showing reduced [^{11}C]ABP688 BP_{ND} in FCD lesions. Results are displayed on each patient's inflated cortical surface, with light gray regions indicating gyri and dark regions indicating sulci. FCD boundaries from manual labeling are displayed as a white outline. Blue-teal colors indicate regions with lower BP_{ND} as compared to controls, whereas red-yellow colors indicate regions with higher BP_{ND} compared to controls. (A) Six patients showed clusters of decreased [^{11}C]ABP688 BP_{ND} differences within the lesion boundaries, which remained significant after correction for multiple comparisons (corresponding cluster-wise P-value is indicated as CWP). (B) Two patients showed small lesional clusters of reduced [^{11}C]ABP688 BP_{ND} that (displayed here at $P < 0.05$), were not significant after correction for multiple comparisons.

	Lesion			Perilesion			Contralateral lesion			Vertex-wise					
Pat	BP	Z	FDR	BP	Z	FDR	BP	Z	FDR	Neg. clusters	Max negative Z-value	Pos. clusters	Max positive Z-value	Region of maximum negative Z-value	Region of maximum positive Z-value
1	1.36	-5.58	0.00	1.32	0.88	0.33	1.39	-0.78	0.33	4	-5.71	4	4.49	L (ipsilateral) frontal	R (contralateral) temporal
2	1.24	-5.01	0.00	1.22	-0.06	0.33	1.26	-0.76	0.39	1	-4.82	1	2.82	R (ipsilateral) precuneus	L (contralateral) occipital
3	1.24	-2.32	0.00	1.24	-0.37	0.33	1.21	-0.79	0.40	1	-5.33	0	N/A	R (ipsilateral) temporal	N/A
4	1.28	-2.81	0.00	1.28	-0.44	0.33	1.26	-0.64	0.40	0	N/A	0	N/A	N/A	N/A
5	1.05	-1.92	0.01	0.92	-0.11	0.33	0.91	-0.34	0.40	2	-3.21	1	5.20	R (ipsilateral) temporal	R (ipsilateral) frontal
6	1.29	-3.34	0.04	1.17	-0.97	0.33	1.28	-0.98	0.41	2	-3.43	2	6.51	L (ipsilateral) cingulate	L (ipsilateral) frontal
7	1.43	-3.28	0.08	1.49	0.25	0.33	1.49	-0.79	0.42	3	-4.78	1	3.94	L (ipsilateral) frontal	L (ipsilateral) temporal
8	1.52	-1.61	0.09	1.48	2.02	0.33	1.43	1.07	0.42	4	-3.98	2	4.42	R (ipsilateral) temporal	L (contralateral) cuneus
9	1.18	-0.12	0.16	1.19	-0.65	0.33	1.10	0.70	0.42	8	-6.46	6	4.85	L (ipsilateral) frontal	L (ipsilateral) occipital
10	1.35	0.10	0.33	1.36	0.73	0.33	1.32	-0.31	0.42	1	-3.91	1	3.96	L (contralateral) temporal	R (ipsilateral) cingulate

Table 4.2 ROI and vertex-wise analysis statistics. Pat: patient number; BP: Mean BP_{ND} within the ROI; Z: z-score; FDR: adjusted p-value using false discovery rate correction; Neg. clusters: the number of significant negative clusters after multiple comparisons correction; Max negative Z-value: the maximum z-value within the significant negative clusters; Pos. clusters: the number of significant positive clusters after multiple comparisons correction; Max positive Z-value: the maximum z-value within the significant positive clusters.

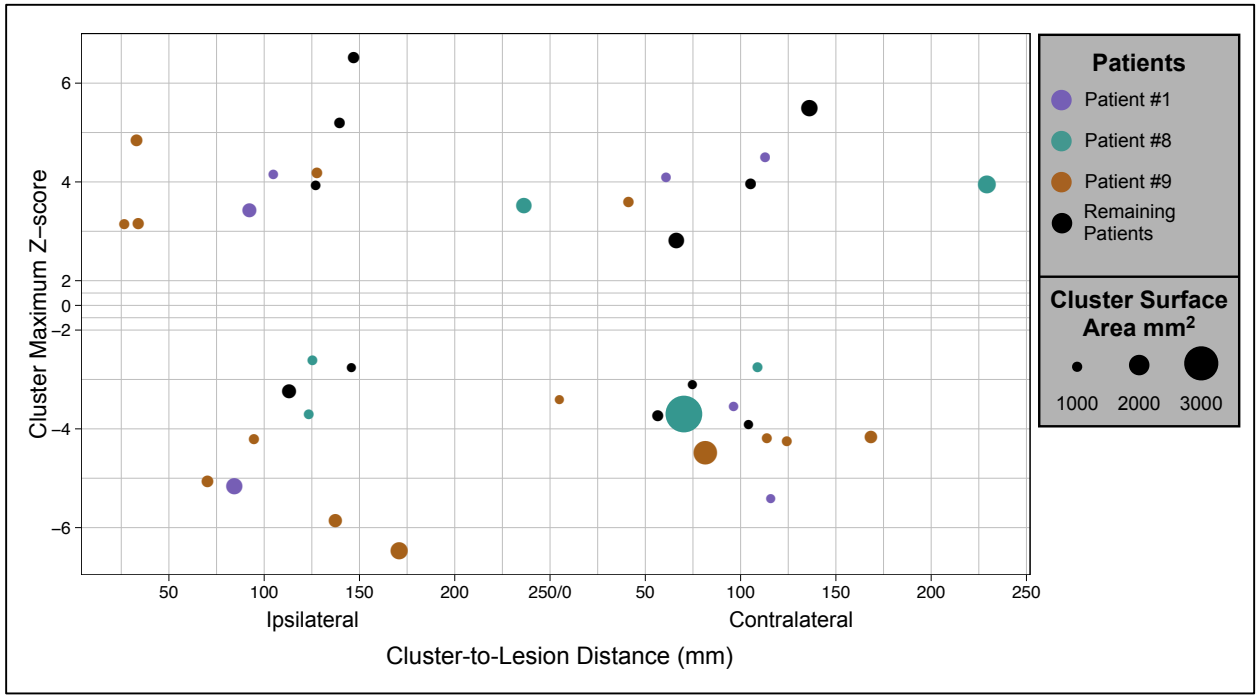

Figure 4.2 Distribution of significant extralesional [^{11}C]ABP688 BP_{ND} clusters. Scattered clusters of increased and decreased [^{11}C]ABP688 BP_{ND} in the ipsi- and contralateral hemispheres observed in our group of patients can be primarily accounted for by 3 subjects. The x-axis displays the percent of the maximum Euclidian distance along the cortical surface between the vertex of max Z-score value within each significant cluster and the nearest edge of the ipsilateral lesion label. In the contralateral hemisphere, distance is calculated between the vertex of max Z-score value within each significant cluster and the nearest edge of the contralateral lesion label. The y-axis displays the maximum Z-score of each significant extralesional cluster (the portion of the y-axis between 2 and −2 is compressed because there are no significant z-scores within this threshold). The diameter of the circle represents the surface area of each cluster, ranging from 1000–3000 mm2. Separate colors distinguish the 3 patients with the largest number of extralesional clusters (patient #1—purple, patient #8—green, patient #9—brown), while extralesional clusters in the remaining 5 patients are displayed altogether in black.

4.5.2 ROI analysis of [^{11}C]ABP688 BP_{ND}

Confirming vertex-wise analysis, significantly lower lesional BP_{ND}, was found in 6/10 patients as compared to the homotopic cortex in healthy controls (z-scores ranging from −5.58 to −2.32; see Table 4.2; Figure 4.3). No differences were found between patients and controls in the perilesional or the contralateral lesion labels. These ROI results differed slightly from the vertex-wise results in that patient #5 (significantly reduced BP_{ND} within a small anterior portion of the lesion—Figure 4.1) did not show a

significant difference in the ROI analysis, which can be understood by the extensive portion of the lesion extending posteriorly and that does not show any BP_{ND} abnormality. On the other hand, patient #4 showed significantly reduced lesional BP_{ND} in the ROI analysis (Figure 4.3), but only small nonsignificant vertex-wise clusters of decreased BP_{ND} in the ipsilateral temporal lobe, including some located within the lesion (Figure 4.1).

Epilepsy duration showed no association with mean BP_{ND} in the FCD lesion ($r = 0.17$, $n = 8$, $P = 0.65$). Considering the possible effect of extracellular glutamate levels fluctuations in [^{11}C] ABP688 BP_{ND} (Zimmer et al., 2015b), we further analyzed whether there was a relationship between the last seizure and the scan date. Likewise, no correlation was found between the number of days since the last seizure and BP_{ND} in the FCD lesion ($r = 0.19$, $n = 8$, $P = 0.60$).

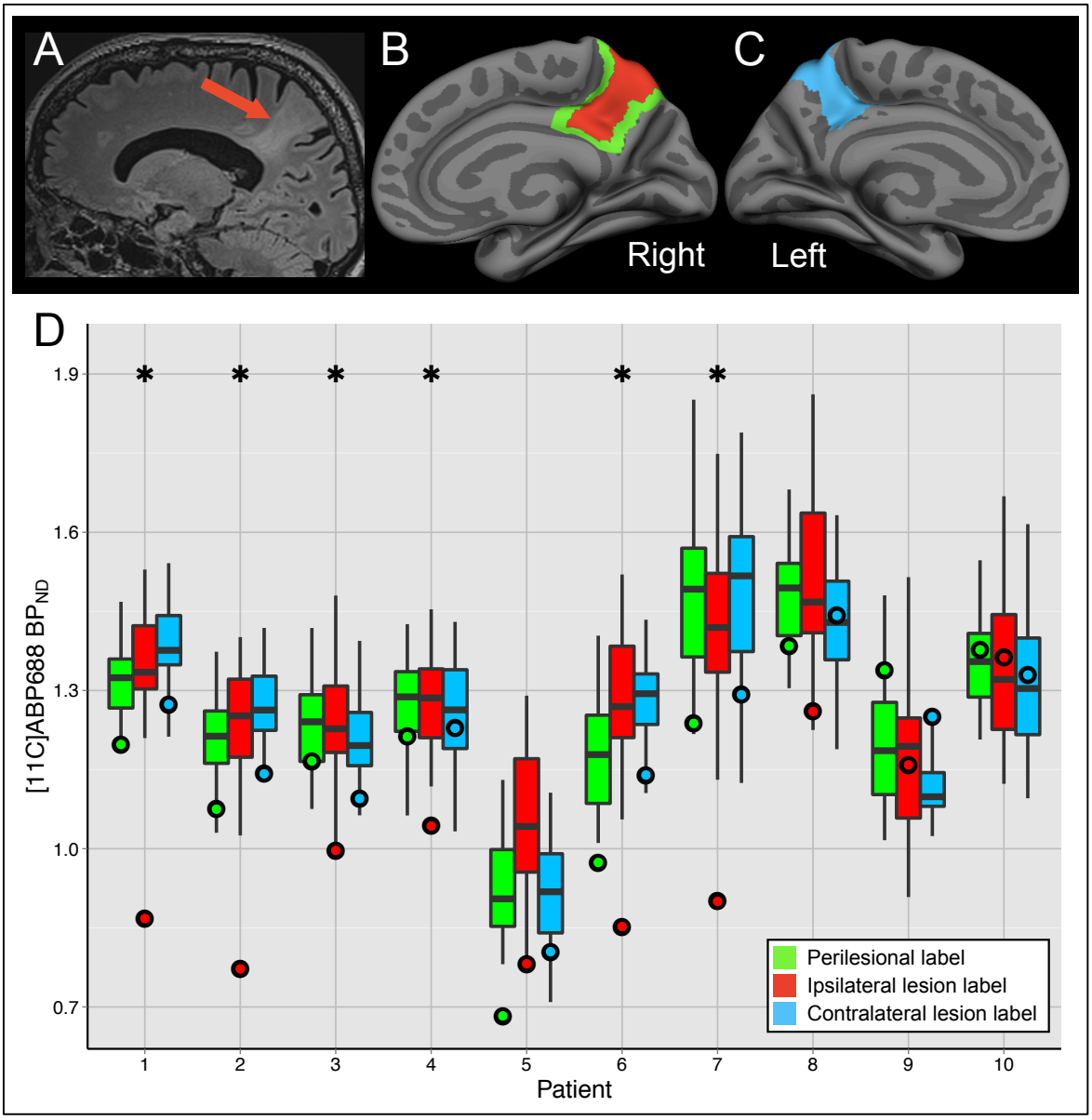

Figure 4.3 Regional [^{11}C]ABP688 BP_{ND} in FCD compared to controls. (A-C) Illustrate the labeling procedure in a patient with a parietal FCD (patient #2): (A) sagittal slice of a T2-FLAIR MRI image showing the lesional cortex (indicated by the red arrow); (B) the ipsilateral right hemisphere of the semi-inflated pial surface with the lesion label shown in red and the perilesional label shown in green and (C) the contralateral left hemisphere of the semi-inflated pial surface displaying the contralateral lesion label in blue. (D) X axis indicate the patient number; Y axis indicates [11C]ABP688 BPND values. The boxplots display the average [11C]ABP688 BPND values within homotopic cortical regions of the control group corresponding to the perilesional (green), the ipsilateral lesion (red), and the contralateral lesion (blue) labels for each patient. The boxplot whiskers extend to the highest or lowest data point within 1.5 times the inter-quartile range. Each circle displays the average BPND for the corresponding patient for the three ROIs. *: $p<0.05$

4.5.3 mGluR5 immunohistochemistry

We found a high degree of intra/intersubject variability in mGluR5 immunoreactivity within the lesions. There was weak to strong neuropil staining; dysmorphic neurons as well as balloon cells, however, most often showed negative or weak immunoreactivity, with isolated and at times rare cells showing moderate or strong immunoreactivity. Intracellular and membrane staining was variable across sections and cells, with one patient showing intranuclear immunoreactivity in isolated dysmorphic and balloon cells (Figure 4.4F). Normal neurons from cortical regions at the border of the resections showed normal strong cytoplasmic mGluR5 immunoreactivity (Aronica et al., 2003). Altogether, the resulting cortical pattern was of weak-moderate mGluR5 immunoreactivity derived from neuropil staining (Figure 4.4A,C,E,G), with negative-mild intracellular immunoreactivity in portions of the lesion with most severe abnormalities (i.e., with higher concentration of balloon cells, Figure 4.4B,H).

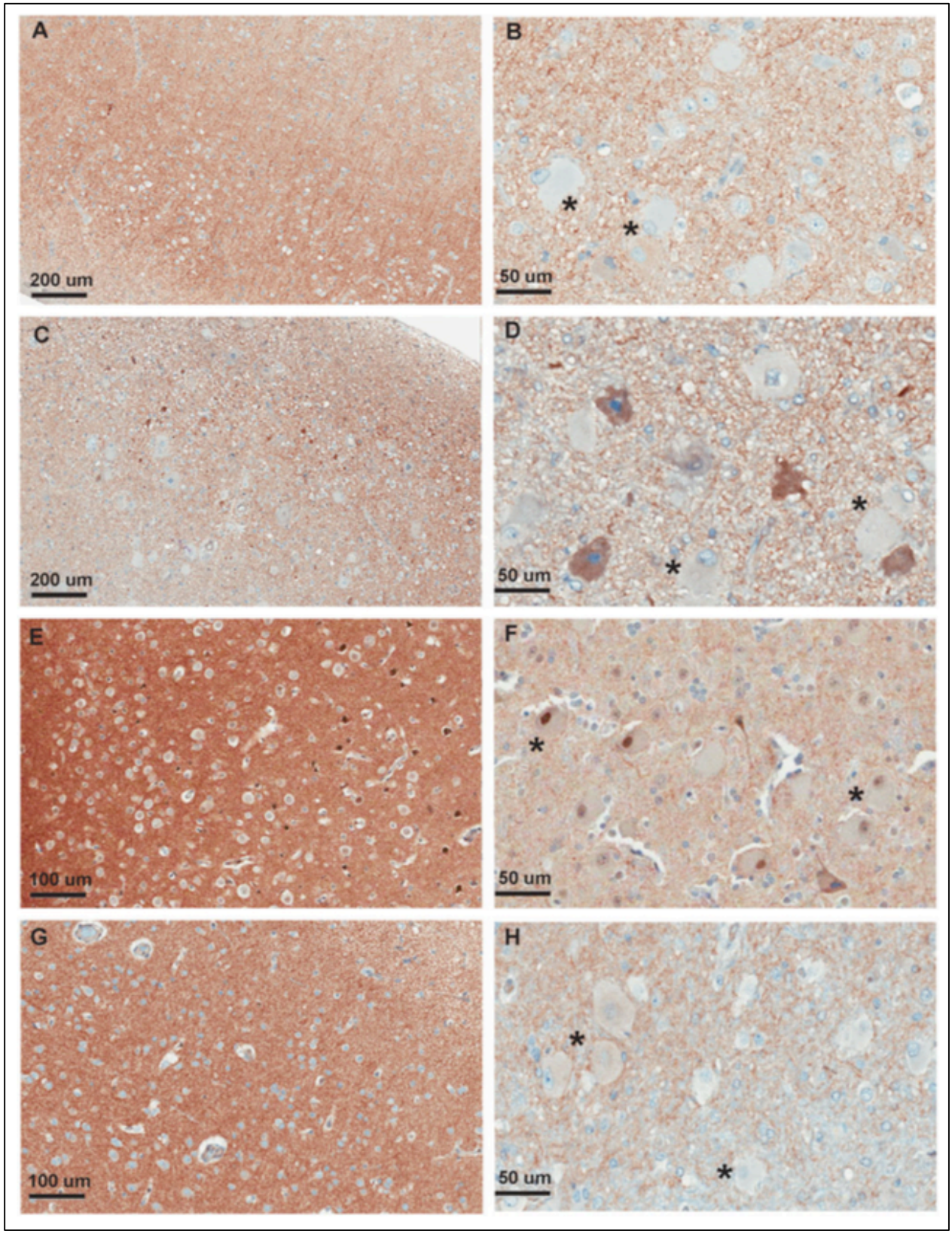
A
200 um
B
50 um
C
200 um
D
50 um
E
100 um
F
50 um
G
100 um
H
50 um

Figure 4.4 mGluR5 immunohistochemistry in resected FCD IIb tissue. (A) Patient #2, objective x10: Disorganization of the cortex, in which no pyramidal cell layer can be properly identified. There is presence of numerous dysmorphic neurons and balloon cells, with few entrapped neurons strongly stained for mGluR5. (B) Patient #2, objective x40: Detailed view of deeper cortical section in the same slide, with presence of balloon cells (asterix) which are negative for mGluR5, with few entrapped neurons and dysmorphic neurons showing a cytoplasmic pattern of mGluR5staining. (C) Patient #3, objective x10: Disorganization of the cortex, presence of dysmorphic neurons and rare neurons strongly stained for mGluR5. (D) Patient #3, objective x40: Detailed view of deeper section in the same slide, with presence of mGluR5-negative balloon cells (asterix) and mGluR5-positive neurons. (E) Patient #8, objective x10: Disorganization of the cortex, in which no pyramidal cell layer can be properly identified. Few neurons are strongly stained for mGluR5. (F) Patient #8, objective x40: Detailed view of deeper section of the cortex, with presence of balloon cells (asterix) with either no clear staining or with a strong nuclear mGluR5 staining. (G) Patient #10, objective x10: Disorganization of the cortex, with strong neuropil staining but no mGlur5-positive neurons identified. (H) Patient #10, objective x40: Detailed view of deeper section depicting the transition of cortex/white matter, with presence of balloon cells (asterix) with either absent staining or weak cytoplasmic staining.

4.6 DISCUSSION

In this study, we identified for the first time in vivo mGluR5 abnormalities in FCD lesions using [^{11}C]ABP688 PET. Reduced BP_{ND} within the FCD was observed in 70% of patients using a combination of vertex-wise and ROI analyses. While no BP_{ND} differences were found in perilesional or contralateral cortices in ROI analysis compared to homotopic regions in healthy controls (Figure 4.3), vertex-wise whole cortex analysis showed mGluR5 abnormalities within the visible lesion sometimes extending to the surrounding cortex (Figure 4.1).

Reduced BP_{ND} may indicate reduced mGluR5 tissue concentration or a reduction of [^{11}C]ABP688 affinity to mGluR5 caused by receptor internalization, conformational changes, anomalous receptor isoforms, or excessive concentrations of endogenous ligands. Reduced BP_{ND} observed in our patients can be first explained by mGluR5 interactions with glutamate, found to be at high levels in the extracellular compartment in the epilepsy focus (During and Spencer). While [^{11}C]ABP688 binds selectively to the mGluR5 allosteric site, glutamate binding to its orthosteric site causes a conformational

change that makes the transmembrane allosteric site unavailable (Ametamey et al., 2007; Treyer et al., 2007).

Although it is still unclear to what degree mGluR5 availability fluctuates during and after seizures, microdialysis studies have shown that extracellular glutamate concentrations increase prior to and during a seizure (During and Spencer; Meurs et al., 2008). Interestingly, the two patients who showed no [^{11}C]ABP688 BP_{ND} differences in the FCD lesion (i.e., patients #9 and #10), experienced frequent seizures prior to [^{11}C]ABP688 PET scanning. We have previously demonstrated, by combined microdialysis and PET, that [^{11}C]ABP688 BP_{ND} is influenced by extracellular synaptic concentration of glutamate (Zimmer et al., 2015b). Prior evidence further supports that [^{11}C]ABP688 BP_{ND} can be modulated by extracellular glutamate: administration of a sub anesthetic dose of ketamine, known to elicit glutamate release, caused a 20% decrease in BP_{ND} throughout the brain of healthy controls (DeLorenzo et al., 2014).

Since seizures induce dynamic changes in GABA and glutamate (Rowley et al., 1997) as well as glutamate transporter expression (Hubbard et al., 2016), it is plausible to expect that [^{11}C]ABP688 BP_{ND} in FCD might incorporate information regarding extracellular concentration of glutamate. As such, these factors should be taken into account to interpret PET mGluR5 imaging in epilepsy due to the high frequency of seizures (including electrographic seizures) among carriers of an FCD lesion. Many patients with FCD have abundant spiking activity, particularly evidenced when these lesions are targeted with intracranial EEG electrodes.

Patient #10 had not only frequent seizures but also abundant interictal epileptiform discharges, with almost continuous spiking activity found in intracranial

EEG monitoring prior to surgery. In addition, patients #9 and #10 experienced frequent nocturnal seizures, which may have interrupted their normal sleep pattern. A recent study showed that sleep deprivation was associated with a global increase in [^{11}C]ABP688 binding, maximal in the medial temporal lobe and cingulate cortex, in healthy individuals (Hefti et al., 2013). While further investigation is needed to confirm these speculations, it is possible that increased seizure activity alone or combined with sleep deprivation may have obscured localized lesional changes in [^{11}C]ABP688 BP_{ND} in these patients.

Furthermore, given its dependency on glutamate concentrations, [^{11}C]ABP688 BP_{ND} might also be related to excitotoxicity. In FCD type IIb, glutamatergic balloon cells with reduced or dysfunctional mGluR5 could potentially result in insufficient postsynaptic modulation of glutamatergic transmission, leading to increased excitotoxicity.

Extralesional areas of increased or decreased BP_{ND} were also observed in some patients, including those who underwent resection of the MRI-visible lesion and who are currently seizure-free. While we cannot fully understand the significance of these scattered extralesional abnormalities, in this small series of patients it did not seem to implicate in a poor postsurgical prognosis or to highlight additional areas of epileptogenicity.

Our analysis showed that extralesional abnormalities could be found scattered across both hemispheres, but were unevenly represented across subjects (Figure 4.2). The patient with the largest number of significant extralesional abnormalities (patient #9) has not been operated. This patient has frequent clusters of seizures and bilateral independent EEG abnormalities, which may suggest cortical abnormalities extending

beyond the visible lesion. However, the other two patients who showed a large number of extralesional abnormalities are both seizure-free following resective surgery of the MRI-visible FCD lesion. The reason why patients imaged in the HR+ PET scanner showed a larger number of extralesional abnormalities could be a result of variability in the HR+ scanner, the effect of combining the HR+ and HRRT data sets, or differences inherent to the patients.

Because of its role in cortical development, neurogenesis, cell survival and regulation of morphogenesis, mGluR5 abnormalities in FCD could reflect a developmental feature of the malformed tissue mediated through this receptor that makes these lesions highly epileptogenic, as demonstrated by neurophysiological studies (Palmini et al., 1995; Catania et al., 2007). In a pilocarpine-treated rat model of temporal lobe epilepsy, status epilepticus was associated with a global reduction in [11C] ABP688 BP_{ND} (Choi et al., 2014). Following status, [^{11}C]ABP688 BP_{ND} remained reduced in the hippocampus and amygdala, regions that later developed epileptogenicity and became capable of producing spontaneous seizures in the chronic stage. This suggests a role for mGluR5 in epileptogenesis of previously normal brain regions.

Tissue analysis conducted in a small subsample of our patients who underwent surgical resection of the MRI-visible FCD lesion, showed concordance between mGluR5 immunoreactivity pattern, abnormal histology and [^{11}C]ABP688 PET. mGluR5 immunohistochemistry revealed negative or weak staining of balloon cells and dysmorphic neurons that, despite not being a quantitative measurement of protein levels, suggest that this might be contributory to the in vivo findings with [11C] ABP688.

In three operated patients, reduced BP_{ND} within the FCD could be at least partially attributed to the substitution of normal appearing mGluR5-positive neurons by mGluR5-negative or weakly stained abnormal (balloon) cells.

The reason why one operated patient did not show detectable in vivo [^{11}C]ABP688 BP_{ND} abnormalities is unknown since the tissue analysis did not reveal any significant differences compared to other operated patients who had in vivo [^{11}C]ABP688 BP_{ND} abnormalities (Figure 4.4G,H). In vivo binding studies using PET should be carefully interpreted since the binding of the radioligand is influenced by 1) the total amount of protein in the tissue (Morey et al., 2009), 2) the functional state of the receptor (high/low affinity state), and 3) the presence of an endogenous competitor (Chugani et al., 1988; van Wieringen et al., 2013; Zimmer et al., 2015b; Vidal et al., 2016).

Furthermore, the quantification or mGluR5 using molecular imaging agents cannot discriminate cellular compartments, but rather provide measures of tissue concentrations (Zimmer et al., 2014). As such, the “normal” [^{11}C]ABP688 binding observed here can be explained by steady-state status of the tissue during the PET scan session (Zimmer et al., 2014). For example, we have previously shown using PET and microdialysis that reduction in tissue glutamate concentrations via activation of glutamate transporter can increase [^{11}C]ABP688 binding by up to 30%. Therefore PET image, rather than simply indicating tissue concentrations of neuroreceptors, can capture functional aspects of neuroreceptors in their native environment (Zimmer et al., 2015b).

Moderate-strong mGluR5 immunoreactivity in balloon cells from FCD type IIb has

been previously described (Aronica et al., 2003). In contrast, most balloon cells and dysmorphic neurons in the tissue obtained in our series had negative or weak mGluR5 immunoreactivity (Figure 4.4), with a moderate-strongly stained neuropil and strong immunoreactivity in neurons that had a normal morphology within the periphery of resected tissue. Although the small number of patients in both series (11 in Aronica, (2003) and 4 in our study) does not allow for clear conclusions concerning these findings, it is interesting to note some differences between FCD IIb patients in these series. Mean age at surgery being much earlier (18 vs. 37) and proportion of seizure-free patients being much lower (50% vs. 100%) in the previously reported series might suggest a more severe form of epilepsy requiring earlier intervention as compared to our adult series (all our operated patients with FCD IIb had surgery after age 25, compared to only 3/11 of theirs).

Keeping in mind that our cohort is very small and considering the clinical-pathological findings in both series, we could speculate that our patients fall into a subcategory of FCD IIb in which epilepsy is less severe. Tissue differences described here (such as predominantly negative or weak mGluR5 positive balloon cells) could potentially correlate with a better prognosis, and the same could be potentially true for the [^{11}C]ABP688 BP_{ND} abnormalities described here.

Because many of our patients in the present series will not have a surgical resection due to location within eloquent cortex, we unfortunately cannot expand the imaging-pathological contributions at this point. Furthermore, the regulation on the administration of radioligands in research by Health Canada does not allow us to prospectively recruit patients younger than 18 y/o, making it unfeasible to design a

prospective comparison to clarify these differences.

Indeed, an important limitation of our study is the small number of patients evaluated. While we attempted to control for potential confounds of particular relevance for mGluR5 imaging (from cigarette smoking to depression), a larger sample size may allow more robust comparisons and more specific characterization of lesional and extralesional abnormalities.

In conclusion, we have shown for the first time in vivo imaging of mGluR5 availability in patients with epilepsy and an underlying FCD. Using [^{11}C]ABP688 PET, we have demonstrated that binding is reduced in these lesions as compared to homotopic areas in healthy controls. Our findings, albeit derived from a small number of patients, support future studies on the evaluation of [^{11}C]ABP688 PET for diagnosis of occult malformations in patients with a negative MRI. Additional analysis comparing in vivo [^{11}C]ABP688 BP_{ND} to ex vivo analyses of protein quantification and function in different types of lesions resected from epilepsy patients may further elucidate the role of mGluR5 in epileptogenicity and epileptogenesis, particularly in malformations of cortical development. [^{11}C]ABP688 PET could shed light on more complex phenotypes related to mGluR5 dysfunction, including acquired forms of epilepsy, as well as neurodegenerative diseases, psychiatric conditions, and Fragile X chromosome syndrome, which can also be associated with seizures. Finally, mGluR5 imaging could potentially be used as an imaging biomarker for epileptogenesis in other forms of acquired epilepsies that can be targeted with disease modifying therapies.

Chapter 5

Reduced efficiency of the mGluR5 network in focal cortical dysplasia: graph-theoretical analysis of [^{11}C]ABP688 PET

Manuscript in preparation

5.1 PREFACE

In patients with FCD, we previously demonstrated reduced mGluR5 availability within the MRI defined lesion (chapter 4). Eighty percent of patients also showed at least one area of mGluR5 abnormality in perilesional or remote regions of the cortex. While the presence of extralesional abnormalities was not associated with a poorer post-surgical prognosis, and therefore unlikely to be related to a secondary area of epileptogenicity or malformation, these findings may suggest widespread alterations in the glutamatergic network. Moreover, the previous vertex-wise z-test analysis did not allow for comprehensive assessment of the organization of mGluR5 abnormalities beyond their size and number. To further characterize extralesional mGluR5 abnormalities in patients with FCD, we performed network analysis of [^{11}C]ABP688 PET using a graph theoretical framework. This technique provides tools to evaluate network efficiency and resilience, which, in the context of mGluR5 availability, may indicate the degree of excitatory signaling dysregulation. To our knowledge this is the first

application of graph theoretical analyses to neuroreceptor PET imaging, which may allow for further investigation of network properties of neuromodulatory systems in healthy and diseased populations.

5.2 ABSTRACT

While focal cortical dysplasia (FCD) is generally characterized by focal histopathological abnormalities, recent evidence suggests that the dysplastic lesion may interact with a widespread network of neuroanatomical structures. Using [^{11}C]ABP688 PET in patients with FCD, we previously observed abnormalities of metabotropic glutamate receptor type 5 (mGluR5) availability in the dysplastic lesion, as well as in perilesional and remote areas of the cortex. To further characterize mGluR5 abnormalities in patients with FCD, we performed graph theoretical analysis of [^{11}C]ABP688 PET binding potentials (BP_{ND}), which allows for quantification of abnormalities across networks. Undirected graphs were constructed for each hemisphere in 17 patients with FCD and 33 healthy controls using inter-regional similarity of [^{11}C]ABP688 BP_{ND}. We assessed group differences in network efficiency, segregation, resilience, and local topology between healthy controls and the ipsilateral and contralateral hemisphere of patients with FCD. FCD patients showed reduced network efficiency and less resilience to targeted attacks in both ipsilateral and contralateral hemispheres, suggesting a more regularized network organization. However, we did not find evidence of significant local reorganization in terms of high degree or highly efficient hub nodes, indicating that reduced efficiency is a general network-wide process rather than due to specific regional changes. Our data provide

the first evidence for widespread mGluR5 network alterations in patients with FCD, affecting network integration. To our knowledge, this is the first application of graph theoretical analysis to neuroreceptor PET imaging, which could support clinical applications for exploration of neuroreceptor network abnormalities in a broad range of neurological diseases.

5.3 INTRODUCTION

Focal cortical dysplasia (FCD) is a malformation of cortical development often associated with drug resistance. FCD comprises a spectrum of histopathological abnormalities, including cortical dyslamination, dysmorphic neurons and balloon cells (Taylor et al., 1971; Blumcke et al., 2011). Although focal pathophysiology is a defining characteristic of FCD, there is growing evidence that, in many patients, the FCD lesion may be part of a more widespread network of abnormalities that contribute to rapid seizure spread and incur greater functional and structural alterations due to chronic seizures (Kramer and Cash, 2012; Caciagli et al., 2014).

mGluR5 is a postsynaptic G-protein coupled receptor that may play a role in the underlying mechanism of epileptogenesis, thereby contributing to the intrinsic epileptogenicity attributed to FCD (Palmini et al., 1995; Chassoux et al., 2000; Merlin, 2002; Aronica et al., 2003; Catania et al., 2007; Bianchi et al., 2009b). Using [^{11}C]ABP688 positron emission tomography (PET), we recently showed that, in addition to abnormal mGluR5 availability within the radiologically identified area of dysplasia, 80% of patients with FCD had mGluR5 reductions in perilesional and remote regions, which were not associated with a visible structural abnormality (DuBois et al., 2016a).

The presence of these abnormalities was however not associated with poorer post-surgical outcomes, suggesting that the biological underpinnings of extra-lesional abnormalities may be distinct from those within the lesion. Similar extralesional abnormalities have been observed in FCD patients using diffusion tensor imaging (DTI) (Lee et al., 2004; Widjaja et al., 2007), MRI morphometry (Thesen et al., 2011; Hong et al., 2014), functional MRI (fMRI) (Dansereau et al., 2014; Besseling et al., 2016), EEG-fMRI (Tyvaert et al., 2008; Thornton et al., 2011), and [^{11}C]flumazenil PET (Juhasz et al., 2009).

While the widespread functional or structural abnormalities observed in patients with FCD are suggestive of a system disruption, few studies have attempted to investigate the overall network organization. Graph theoretical analysis is a framework for quantification of network topology that may aid in the characterization of distributed abnormalities (Rubinov and Sporns, 2010; Sporns, 2016). In one graph theory study of magnetoencephalography, increased global efficiency was found in the gamma and theta bands, suggesting a more randomly organized network in patients with FCD (Jeong et al., 2014). In contrast, graph theoretical analyses of patients with non-lesional focal epilepsy have consistently shown evidence of a less efficient and more regularly ordered network, which has been associated with cognitive decline (Hermann et al., 2009; Caciagli et al., 2014; Chiang and Haneef, 2014). It is possible that neuroreceptors network alterations contribute to dysfunction observed in these patients.

To characterize the network of mGluR5 availability in patients with FCD, we performed graph theoretical analysis based on the inter-regional similarity of [^{11}C]ABP688 PET binding potentials (BP_{ND}). Graph metrics, including network

efficiency, segregation, resilience, and local topology, were used to compare the ipsilateral and contralateral hemispheres of FCD patients to healthy controls. Based on previous studies in non-lesional focal epilepsy, we hypothesized that patients with FCD would show altered efficiency in the ipsilateral hemisphere, which may extend to the contralateral side. While studies of acquired brain injury, simulated lesions, and non-lesional focal epilepsy show some degree of nodal differences, it is unknown if a similar relationship will be present for developmental lesions such as FCD (Alstott et al., 2009; Vlooswijk et al., 2011; Gratton et al., 2012).

5.4 METHODS

5.4.1 Subjects

Seventeen patients with focal epilepsy previously investigated at the Montreal Neurological Hospital with an [^{11}C]ABP688 PET study were retrospectively selected for the study based on criteria as follows. Patients were included in the study if they had diagnosis of FCD from either MRI or neuropathology following surgery: positive MRI and neuropathological diagnosis of FCD (N=5), positive MRI without surgery (N=7), and negative MRI and neuropathological diagnosis of FCD (N=5). For detailed information regarding lesion location, surgical outcome, and clinical variables, refer to Table 5.1.

As described previously in DuBois et al., 33 healthy subjects (range=20-77y/o; males, n=18, 47.4 $\pm$ 17.7y/o; females, n=15, 46.2 $\pm$ 18.9y/o) were recruited for the study (DuBois et al., 2016a). Exclusion criteria included: personal or first-degree relative history of axis I psychiatric disorders, chronic use of CNS active medications or illicit drugs, pregnancy/breastfeeding, present or past cigarette usage, history of neurological

or medical disorders and MRI contraindications. The study was approved by the Montreal Neurological Institute Research Ethics Board. All subjects provided written informed consent prior to participation in the study.

5.4.2 PET acquisition and reconstruction

3-(6-methyl-pyridin-2-ylethynyl)-cyclohex-2-enone-O-^{11}C-methyloxime ([^{11}C]ABP688) was synthetized as previously described (Elmenhorst et al., 2010; DuBois et al., 2016b). Images were acquired in the Siemens ECAT EXACT HR+ scanner for 7 patients and 7 controls [approximate resolution, 6 mm full width at half maximum (FWHM)]. The remaining subjects (10 patients and 26 controls) were scanned in the Siemens High Resolution Research Tomograph (HRRT, approximate resolution of 3mm FWHM). A 7-minute transmission scan was performed for attenuation correction, followed by a 1-hour dynamic emission scan, which began concurrently with the slow bolus injection of [^{11}C]ABP688 (injected dose/activity=356.7±25.2MBq; specific activity=13.6±6.3GBq/μmol, unavailable for 10 of the controls).

Data was acquired in 3D list mode and reconstructed by filtered back-projection. The reconstructed time-series was 128×128×63 voxels (2.45 mm pixels) for the HR+ and 256×256×207 voxels (1.21875 mm pixels) for the HRRT. To combine PET scanner data, HRRT images were blurred with an anisotropic Gaussian kernel of 5.7×5.7×6.7 mm FWHM (DuBois et al., 2016a).

Pat	Age	Sex	FCD lobe	Radiology (MRI)	Last sz prior to scan (days)	Age at sz onset	Duration of epilepsy at the time of PET scan (years)	Surgery follow-up (years), Engel class	Pathology	AEDs
1	39	F	L frontal	Pos	180	3	36	no	N/A	LEV, LMT, CLB, CBZ
2	56	M	R parietal	Pos	1	8	48	6y, Engel I	FCD IIb	CBZ, LEV, CLB
3	25	M	R temporal	Pos	4	8	17	6y9m, Engel I	FCD IIb	CBZ
4	20	F	L temporal	Pos	1	14	6	no	N/A	CLB
5	19	F	R temporal	Pos	11	15	4	6y11m, Engel II	FCD IIa	VA, LEV, PB
6	31	F	L cingulate	Pos	1	16	15	no	N/A	LMT, DPH, CLB
7	39	F	L frontal	Pos	30	34	5	no	N/A	none
8	29	M	R frontal	Pos	1	0.4	29	4y3m, Engel I	FCD IIb	VA, OXC, CLB
9	41	F	L temporal	Pos	6	12	29	no	N/A	LMT, PB, CLB
10	38	M	R frontal	Pos	1	17	21	5y1m, Engel I	FCD IIb	CBZ, CLB
11	23	F	L cingulate	Pos	1	10	13	no	N/A	DPH, TPM
12	29	F	L parietal	Neg	120	21	8	4y, Engel II	FCD IIa	CBZ, LMT
13	35	M	R frontal	Neg	1	16	19	4y6m, Engel I	FCD IIa	LEV, TPM
14	18	F	R parietal	Neg	25	12	6	3y9m, Engle I	FCD IIb	none
15	22	F	R cingulate	Neg	14	17	5	0y1m, N/A	FCD IIa	LCM
16	25	F	R frontal	Pos	4	12	13	no	N/A	CBZ, CLB, LCM
17	41	M	R cingulate	Neg	0.5	6	35	6y11m, Engel II	FCD IIb	OXC, LEV, PB

Table 5.1 Clinical Information. Pat: Patient ID; F: female; M: male; L: left; R: right; Pos: positive; Neg: negative; sz: seizure; N/A: not applicable; AED: antiepileptic drug; LEV: levetiracetam, LMT: lamotrigine; CBZ: carbamazepine; CLB: clobazam; DPH: diphenylhydantoine; VA: valproic acid; TPM: topiramate; OXC: oxcarbazepine; PB: phenobarbital

5.4.3 MRI acquisition and processing

As previously described in DuBois et al. (2016a), A 3D T1-weighted MPRAGE sequence (1 mm^3 voxel size, 256x256x256 matrix; TE=2.98; TR=2300; TI=900 ms; flip angle=9°) was acquired for each subject using a Siemens Trio 3T scanner. MRI data was analyzed with FreeSurfer (www.surfer.nmr.mgh.harvard.edu, version 6.0)(Dale et al., 1999; Fischl et al., 1999a; Fischl et al., 2002). The process included intensity normalization, removal of the skull and non-brain tissue (Segonne et al., 2004), cortical and subcortical segmentation of grey and white matter structures (Fischl et al., 2002; Destrieux et al., 2010), and sub-voxel reconstruction of the pial surface and gray matter/white matter boundary (i.e. the white matter surface) (Dale et al., 1999; Fischl et al., 1999a). Each individuals' surface was then registered to an FreeSurfer template surface for analysis and visualization (Fischl et al., 1999b; Greve et al., 2013).

The MRI and the time-averaged raw PET images were aligned by fitting the white matter surface to the maximum of the radioactivity gradient (Greve and Fischl, 2009). For surface-based partial volume correction and network analysis, PET data was sampled from the volume halfway between the white matter and pial surfaces using nearest-neighbor interpolation (Greve et al., 2014; DuBois et al., 2016b).

5.4.4 Partial volume correction and binding potential analysis

Correction for partial volume error was performed using a data-driven, region-based per-voxel partial volume correction method, as described previously (DuBois et al., 2016a; DuBois et al., 2016b). Briefly, time-averaged raw PET data were sampled to the surface and clustering was performed to create homogenous cortical regions of

radioactivity. Clustered cortical regions were then sampled back to the volume and combined with subcortical grey and white matter segmentations, which were partial volume corrected using the geometric transfer matrix method (Rousset et al., 1998). The resulting values were then used to perform per-voxel correction for the whole brain (Thomas et al., 2011).

As described previously, [^{11}C]ABP688 non-displaceable binding potentials (BP_{ND}) were estimated with a simplified reference tissue model, using the cerebellar grey matter as the reference region (DuBois et al., 2016a). While mGluR5 is expressed in the cerebellar cortex, several studies indicate that cerebellar [^{11}C]ABP688 binding is negligible, including *in vitro* and *in vivo* imaging of [^{11}C]ABP688 binding in humans and animals (Elmenhorst et al., 2010; Milella et al., 2011), as well as human postmortem analysis of mGluR5 mRNA (Daggett et al., 1995) and protein expression (Deschwanden et al., 2011). Voxel-wise parametric mapping was performed using basis function implementation (Lammertsma et al., 1996; Gunn et al., 1997; Innis et al., 2007; Elmenhorst et al., 2010).

5.4.5 Network nodes

To define network nodes, we utilized an existing probabilistic atlas, which parcellated the cortex of the FreeSurfer average template brain into 74 regions per hemisphere based on gyral and sulcal anatomy (Destrieux et al., 2010). In order to achieve regions of roughly similar surface area, some regions were divided or combined with neighboring regions, resulting in 91 regions per hemisphere with an average surface area of 839 $\pm$ 259mm^2. Each of these 182 regions represented a network node.

5.4.6 Network edges

Following binding potential analysis, BP_{ND} values were sampled from each subject's volume to the FreeSurfer surface template and extracted from each cortical region in the parcellation scheme. The probability density function was then computed for each regional BP_{ND} distribution, at the individual subject level, using kernel density estimation with automatically chosen bandwidths (Rosenblatt, 1956; Wang et al., 2016) (function: kde, http:// www.mathworks.com/matlabcentral/fileexchange/14034-kernel-density-estimator). Subsequently, we compared the probability density function of each node pair by calculating the symmetrical Kullback-Leibler divergence, which was defined as follows:

$$KL(p,q) = \int_x \left(p(x)\log\frac{p(x)}{q(x)} + q(x)\log\frac{q(x)}{p(x)} \right) dx \geq 0$$

where *p* and *q* are the two probability density functions (Kullback and Leibler, 1951; Kong et al., 2014). KL divergence was then converted to a measure of similarity (KLS), with values between 0 and 1, using the following equation:

$$KLS(p,q) = e^{-KL(p,q)}$$

where *e* is the natural exponential (Kong et al., 2014; Kong et al., 2015). These analyses generated a whole-brain matrix of 182 x 182 nodes, with edges corresponding to the KLS value between a given node pair. Hemispheric matrices were generated by dividing the whole-brain matrix into 4 quadrants. Separately, left-to-left and right-to-right hemisphere node pairs were extracted, comprising left hemisphere and right hemisphere matrices of 91 x 91 nodes each (Figure 5.1).

5.4.7 Thresholding

Prior to network analysis, a density threshold was applied to equate the number of edges between both subjects and hemisphere matrices. The density threshold was determined by preserving a proportion of high KLS edges relative to the number of total possible edges in the matrix. All analyses were done over a broad range of densities (5% – 40%, with an interval of 1%), which included the optimal range for measuring several graph metrics (5% – 25%), including small worldness (Bassett et al., 2008). The resulting matrices reflect unweighted, undirected graphs, which ensures that group and individual differences reflect topological alterations rather than aberrant KLS values (He et al., 2008).

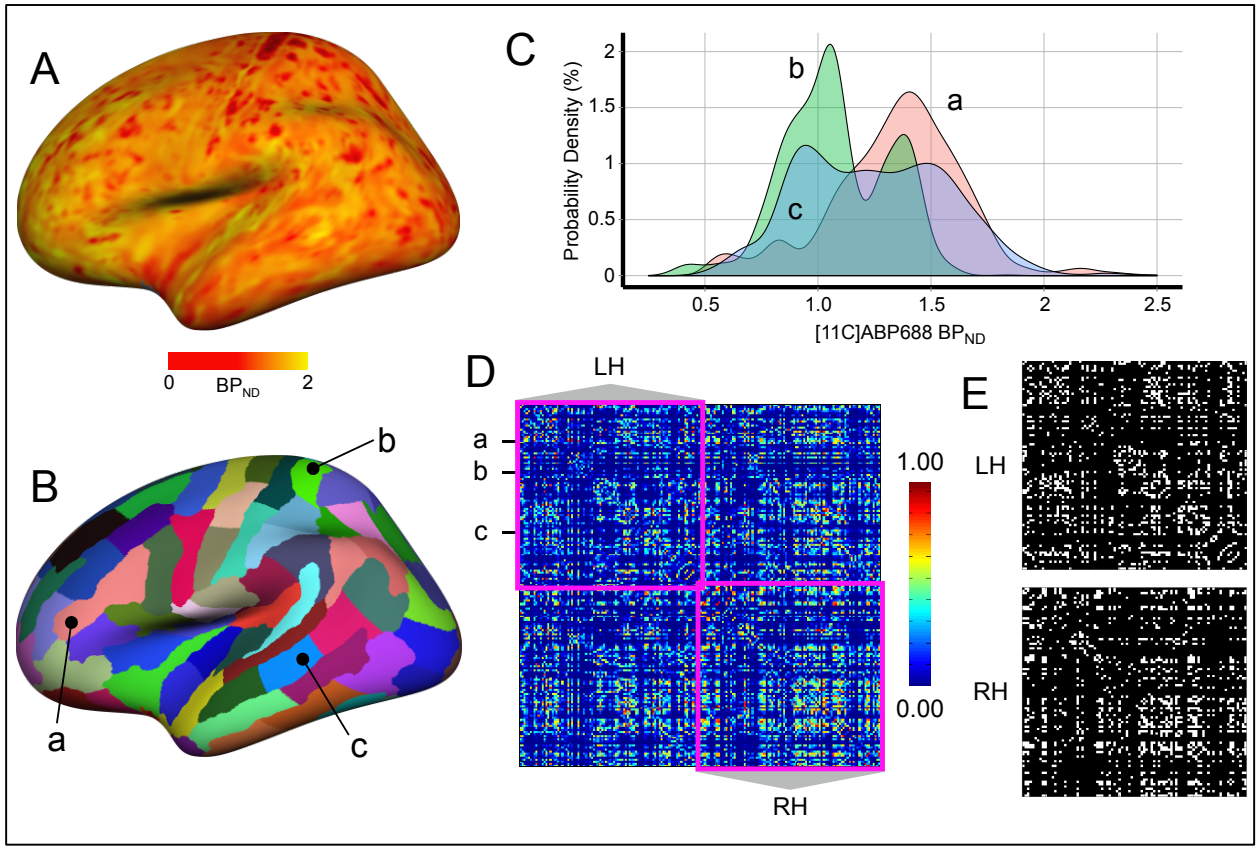

Figure 5.1 Construction of network nodes and edges. Displays [^{11}C]ABP688 BP_{ND} values (unitless, ranging from 0-2) from a healthy control sampled to the average inflated surface (A). Regions of interest displayed on the average inflated surface, highlighting three ROIs from the frontal (a; pink), parietal (b; green), and temporal (c; blue) lobe (B). A representation of the probability density estimate from each of the three ROIs displayed with the corresponding color (C). The whole-brain graph displaying the KLS value from 0-1 (D). The network-wide KLS values for the three example ROIs are displayed on the indicated line, with the right and left hemisphere subgraphs are highlighted in pink. The thresholded (15% sparsity) subgraphs for the left and right hemisphere (E).

5.4.8 Network analysis

We examined network topology at global and local scales for each graph (Figure 5.2A). Global metrics included: characteristic path length, clustering coefficient, small-world index, modularity, and global efficiency. Local metrics included: local efficiency, betweenness centrality, participation coefficient, and degree centrality. For a detailed review of these measures, see Rubinov and Sporns (Rubinov and Sporns, 2010). All graph metrics were calculated using the Brain Connectivity Toolbox (http://www.brain-connectivity-toolbox.net) with MATLAB (version 2015b; MathWorks).

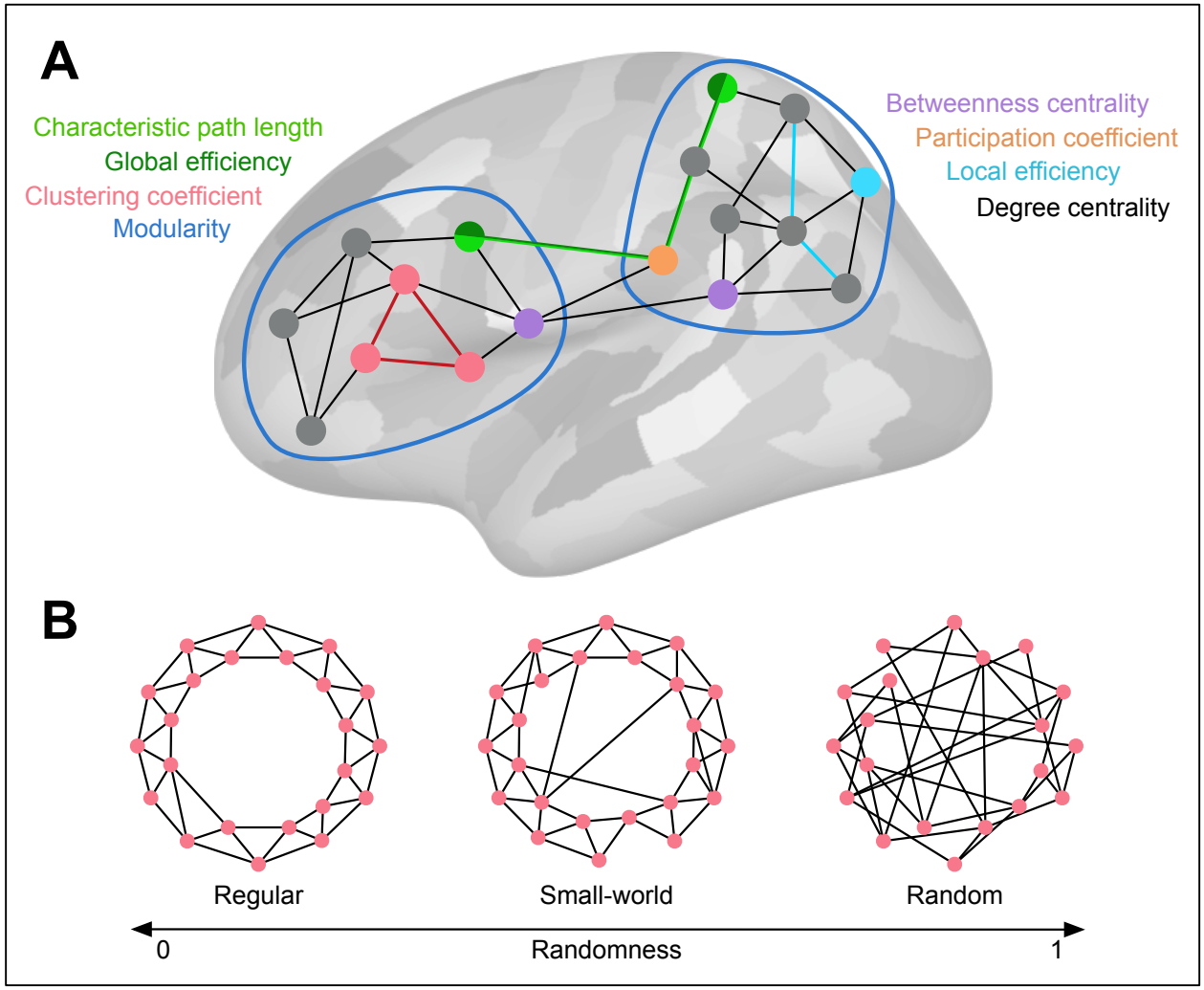

Figure 5.2 Measures of Network topology. An illustration of the network measures assessed in the present study. Gray-scale regions of interest are displayed on the inflated surface with basic representation of graph overlaid (A). Colors correspond to each of the global (right) and local (left) metrics, displaying the basic components of each measurement. A representation of random network organization is shown to illustrate the features of the small-world network (B).

Characteristic path length is defined as the average shortest path length between all node pairs. It is a measure of network integration.

Clustering coefficient of a node is equivalent to the ratio of the nodes neighbors that are connected to each other. Network-wide clustering coefficient is the average clustering coefficient of all nodes, and reflects the degree of clustered connectivity around an average node.

Modularity is a measure of the degree to which the network can be subdivided into non-overlapping groups. Here we utilized a multi-iterative algorithm optimized for detection of hierarchical modules in large networks (Blondel et al., 2008).

Global efficiency is defined as the average inverse of the shortest path length. Although it is related to path length, it is often considered a superior measure of network integration (Latora and Marchiori, 2001).

Small-world index. Compared to a random network, a small world network should have a similar characteristic path length and a greater clustering coefficient (Figure 5.2B) (Maslov and Sneppen, 2002). To determine if the networks were non-randomly organized, characteristic path length and clustering coefficient were separately normalized by 100 randomly generated networks, which preserved the number of nodes, edges, and the degree distribution of the real network. The small world index was then calculated by dividing normalized clustering coefficient by normalized path length.

Degree Centrality is equal to the number of edges connected to a given node, also described as the number of neighbors of a node.

Local efficiency for a given node is defined as the shortest path connecting the neighbors of that node. Like clustering coefficient, average local efficiency is related to local connectivity, although it is also considered a measure of fault tolerance of the network.

Betweenness centrality is defined as the fraction of all the shortest path that pass through a given node. High betweenness centrality nodes are likely to connect disparate parts of the network.

Participation coefficient is a measure of the number of inter-module connections for a given node. A high participation coefficient node is known as a connector hub, as it facilitates inter-modular integration.

Resilience reflects network integration by measuring the degree of alternative routes to ensure efficient information processing (Achard and Bullmore, 2007). To determine the resilience of each network, we simulated attacks on the network by removing nodes, either randomly (random attack) or in descending order of their degree centrality, participation coefficient, or betweenness centrality (targeted attack) (Albert et al., 2000). Thus, network components were incrementally removed without replacement from 0 to 100% at an increment of 1%. After each node deletion, global efficiency was recalculated (Rubinov and Sporns, 2010). Analyses were performed at a network density of 15%, which is consistent with prior studies (Bernhardt et al., 2011; Lo et al., 2015).

5.4.9 Statistical analyses

To compare graph metrics between FCD patients and healthy controls, we calculated the area under the curve (AUC) across the density spectrum using Simpson's rule and performed non-parametric permutation tests with approximately 10,000 iterations (Hothorn et al., 2006). Pearson correlation was used to assess the relationship between graph metrics and clinical variables. False discovery rate (FDR) correction was used to control for multiple comparisons ($P < 0.05$) (Benjamini et al., 2006). All analyses and figures were generated with the R statistical software package (R Core Team, 2013).

5.5 RESULTS

5.5.1 Hemispheric network topology

In healthy controls, no significant hemispheric differences were found after FDR correction in any of the four global network metrics, or any node using the four local metrics. Therefore, we grouped the left and right hemispheres of healthy controls and compared graph metrics relative to the ipsilateral hemisphere (including right and left side) and contralateral hemisphere (including right and left side) of FCD patients.

Both FCD patients and healthy controls exhibited a small-world index greater than one, over the entire density spectrum (Figure 5.3A). This reflected greater clustering and approximately equal path length compared to randomly generated networks (Figure 5.2B). Interestingly, FCD patients showed a significantly reduced small-world index in the contralateral hemisphere (Z = -2.93, P = 0.002, *P-adjusted* = 0.01). While the small-world index in the ipsilateral hemisphere of FCD patients was similar to the contralateral hemisphere at high density thresholds, it converged with that of healthy controls at densities below 10%, without a significant AUC difference (P = 0.21) (Figure 5.3B). Clustering Coefficient and characteristic path length did not show significant differences between patients and controls in either hemisphere.

Global efficiency was significantly reduced in the ipsilateral (Z = -2.78, P = 0.004, *P-adjusted* = 0.009) and contralateral (Z = -2.54, P = 0.01, *P-adjusted* = 0.01) hemispheres of FCD patients (Figure 5.3C and D). Modularity was significantly reduced in the contralateral hemisphere (Z = -2.23, P = 0.03, *P-adjusted* = 0.04), but not in the ipsilateral hemisphere (P = 0.13). Overall, hemispheric graph metrics reflect a more

regularized network topology in patients with FCD relative to healthy controls.

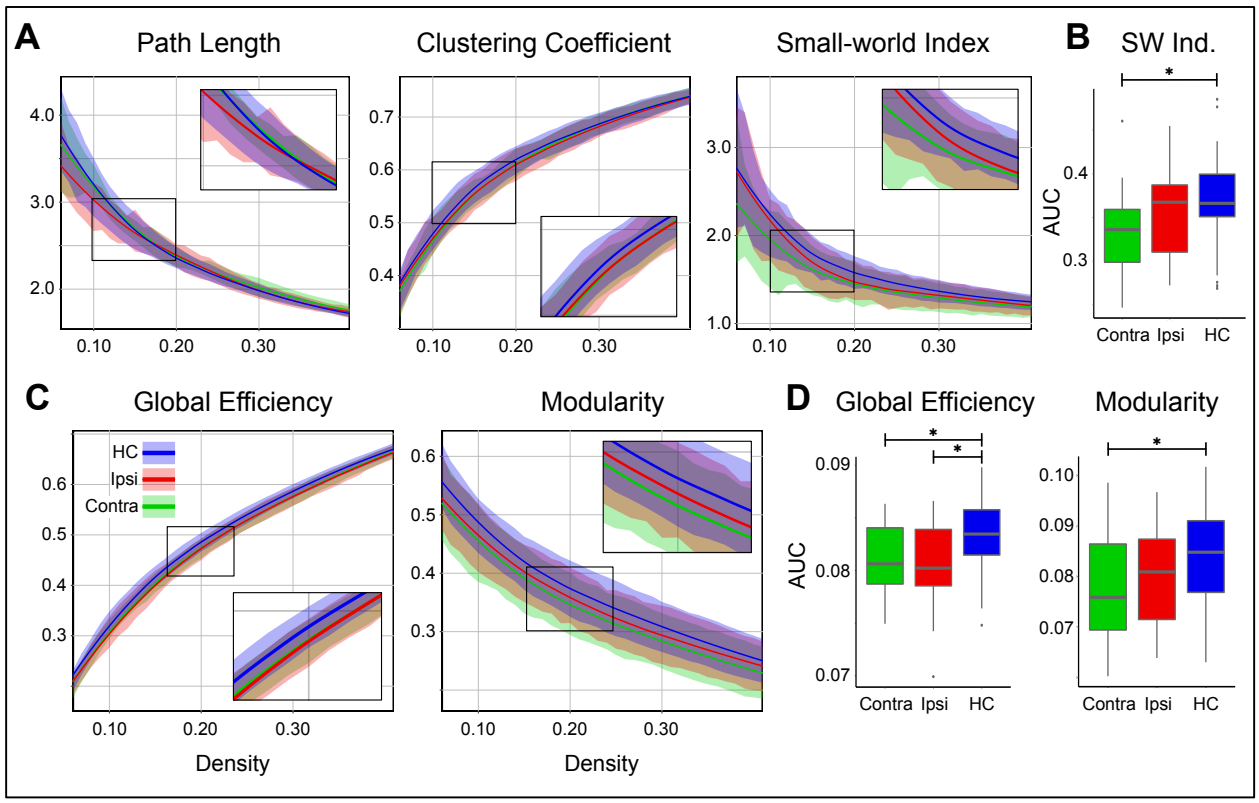

Figure 5.3 Group differences in network topology. Path length, clustering coefficient, and small-world index graphs display the fitted density curve for the contralateral FCD hemisphere (green), ipsilateral FCD hemisphere (red), and combined hemispheres of healthy controls (blue) (A). Shaded regions show one standard deviation above and below the regression line. Box-plots display the area under the curve across the density spectrum, with the star indicating a significant difference between healthy controls and the contralateral hemisphere of FCD patients (B). Global efficiency and modularity display a consistent difference across the density spectrum (C), although modularity is only significantly different from healthy controls in the contralateral hemisphere, whereas global efficiency significantly differs from healthy controls in both hemispheres.

5.5.2 Resilience

Upon random node removal, global efficiency remained higher (>50% after 25% of nodes removed) than targeted node removal (i.e., based on degree centrality, betweenness centrality, or participation coefficient, Figure 5.4), indicating that mGluR5 brain networks were resistant to random failure. Global efficiency of all groups was

highly degraded by targeted removal of high centrality (betweenness, degree, or participation) nodes. Global efficiency was reduced by more than 50% after 25% removal of high centrality nodes, and was reduced by approximately 85% after 50% removal of high centrality nodes (Figure 5.4).

Between-group differences of normalized global efficiency were not significant after random node removal (Figure 5.4A), or targeted node removal based on betweenness centrality (Figure 5.4B). However, targeted node removal based of participation coefficient nodes showed a significant difference in normalized global efficiency for both the ipsilateral (Z = -2.75, P = 0.005, *P-adjusted* = 0.02) and contralateral (Z = -3.0, P = 0.002, *P-adjusted* = 0.01) hemispheres of FCD patients compared to the combined hemispheres of healthy controls (Figure 5.4D). There was also a trend toward reduced normalized global efficiency based on removal of high degree nodes in the ipsilateral hemisphere of patients with FCD (Z = -1.9, P = 0.06, *P-adjusted* = 0.13). This supports the above finding that the mGluR5 network is more regularized throughout the brain of patients with FCD as compared to healthy subjects, which is associated with reduced resistance to targeted attacks to inter-modular connections.

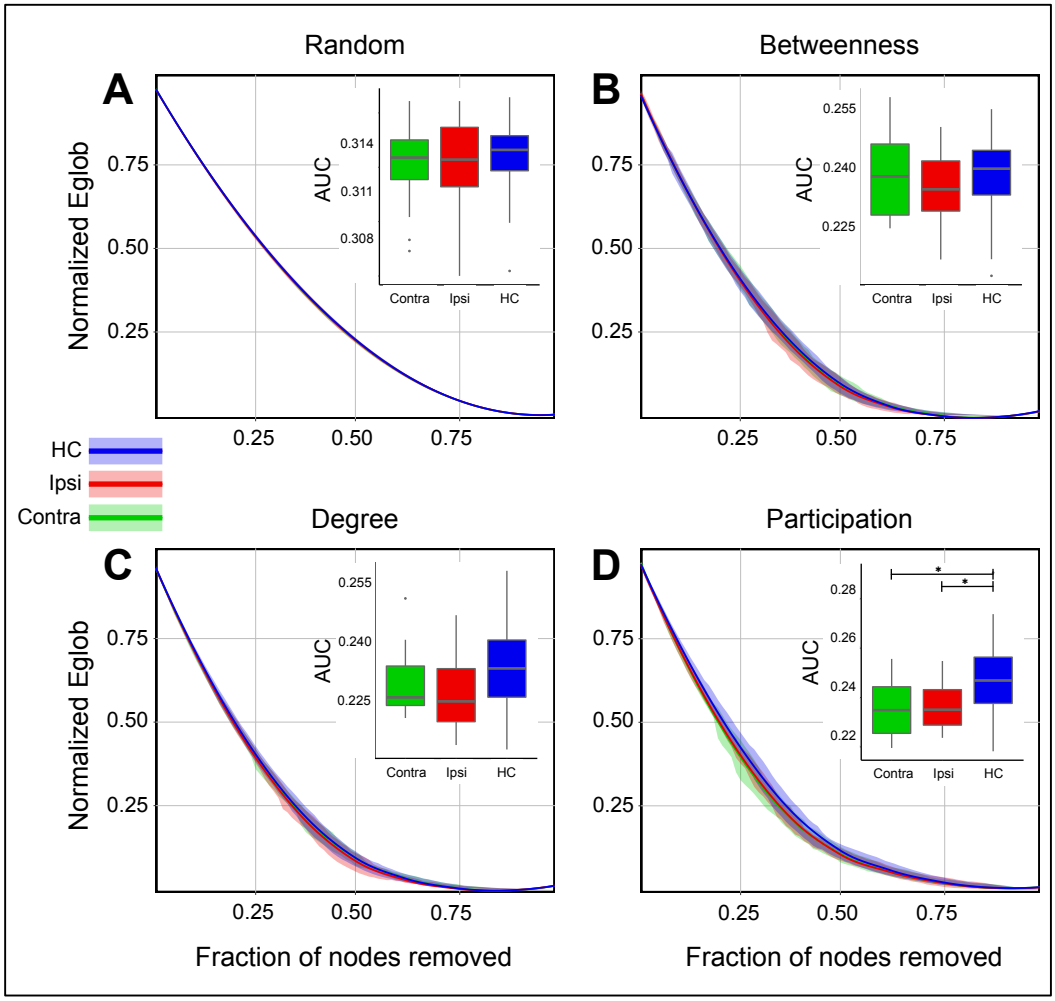

Figure 5.4 Network resilience to targeted and random attack. Fitted curves display the normalized global efficiency measured after each incremental removal of a random node (A), high betweenness centrality node (B), high degree node (C), or high participation coefficient node (D). Shaded regions show one standard deviation above and below the regression line. The x-axis displays the fraction of nodes removed. Boxplots indicate the area under the curve across the density spectrum, with the star indicating a significant difference between healthy controls (blue) and the contralateral hemisphere (green) or ipsilateral hemisphere (red) of FCD patients (B).

5.5.3 Nodal topology

Given the group difference in global efficiency, we further examined the nodal efficiency at the individual patient and group level. In healthy controls, high efficiency nodes were observed in the precuneus, anterior cingulate, lateral temporal, anterior superior frontal, and precentral cortices. In FCD patients, reduced efficiency was found

contralateral to the lesion in the anterior cingulate and superior temporal nodes, although these differences were not significant after FDR correction. Likewise, excluding lesion nodes in the ipsilateral hemisphere led to non-significant reductions in efficiency in the anterior cingulate, middle and superior temporal, superior frontal, and insular nodes. None of the nodes significantly differed however, when individual patients were compared to the healthy control group.

5.5.4 Correlational of network metrics and clinical variables

In the FCD group, we explored the relationship between the global network metrics and clinical variables, including duration of epilepsy, age of onset, and days since last seizure (table 1). A significant correlation was found between last seizure (in number of days) prior to scan and modularity in the ipsilateral hemisphere (r = -0.42, P < 0.05), suggesting that more recent seizures are related to increased modularity in the ipsilateral hemisphere. No significant relationship was found in the contralateral hemisphere between days since last seizure and modularity. None of the other metrics showed a significant relationship with any of the other clinical variables.

5.6 DISCUSSION

In the present study, we compared the network topology of mGluR5 availability between patients with FCD and healthy controls by performing graph theoretical analysis of [^{11}C]ABP688 BP_{ND} inter-regional similarity. mGluR5 networks in both groups showed a small-world organization, reflecting increased clustering and approximately equal path length relative to randomly organized networks (Figure 5.3A and B). In the

healthy brain, small-world networks reflect the large proportion of local intra-cortical connection relative to the small number of connections that are made between networks (Watts and Strogatz, 1998; Zhang and Sejnowski, 2000; Sporns and Zwi, 2004; Massobrio et al., 2015). While mGluR5 networks do not share anatomical connections, through several roles in cortical development, cell survival, and morphogenesis, the small-world topology of FCD patients may reflect more similar developmental influences locally as compared to distant regions. In addition, mGluR5 mediates postsynaptic glutamatergic excitability, which may reflect a small-world topology as a result of locally similar excitatory thresholds (Conn and Pin, 1997; Anwyl, 1999; Catania et al., 2007).

Within the spectrum of small-world networks, patients with FCD showed a more regularized mGluR5 topology than healthy controls, as evidenced by reduced network efficiency in both the ipsilateral and contralateral hemispheres (Figure 5.3C). In contrast to our results, a previous neurophysiological study using magnetoencephalography showed increased global efficiency in the beta and gamma bands of patients with FCD compared to healthy controls (Jeong et al., 2014). However, in line with our findings, multimodal graph theoretical analyses, including magnetoencephalography, have consistently observed decreased network efficiency in patients with non-lesional neocortical epilepsy and temporal lobe epilepsy (Horstmann et al., 2010; Bernhardt et al., 2011; Vlooswijk et al., 2011; Vaessen et al., 2012). In the current study, subgraph analysis revealed divergent hemispheric findings in both the small-world index and modularity, which showed significant reductions in the contralateral hemisphere that were not present in the ipsilateral hemisphere. These findings may reflect high similarity values within the FCD lesion, resulting in higher clustering and lower path length in the

ipsilateral hemisphere at low density thresholds (Figure 5.3A).

Given the large group difference in global efficiency and the contralateral hemispheric findings in modularity and small-worldness, we expected that specific nodes would show differences in local efficiency between patients with FCD and healthy controls. While moderate differences were found within the ipsilateral and contralateral association cortices, none of these regions differed significantly at either the individual or group level. Nodal differences have been less consistently reported than global differences in previous graph theoretical analysis of focal epilepsy (Bernhardt et al., 2011; Jeong et al., 2014). Although a resting-state fMRI study of frontal and temporal lobe epilepsy patients has shown significantly decreased clustering throughout the brain, there was no association to the laterality of the seizure focus or to the distribution of functional networks (Vlooswijk et al., 2011). In addition, studies of acquired brain injury and simulated lesions show widespread nodal differences, largely mediated by the centrality of the lesioned node (Alstott et al., 2009; Gratton et al., 2012). However, these studies do not account for developmental processes such as those which may occur in patients with FCD in order to compensate for dysfunction of a normally high centrality node.

In our analysis, local differences in network topology may have been obscured by the heterogeneous distribution of the lesion location and lesion extent in our FCD patient population. While we have previously shown local abnormalities using vertex-wise analysis of [^{11}C]ABP688 BP_{ND} in patients with FCD, it is possible that the graph theoretical analysis methods used here may be less sensitive to local variability in network organization (DuBois et al., 2016a). Additional graph theoretical analyses using

multimodal imaging methods are needed to fully explore local network abnormalities in patients with FCD.

A more regularized network in patients with FCD is further supported by our finding of decreased resilience to attacks targeting high participation coefficient nodes (Figure 5.4). While random graphs maintain high levels of global efficiency after node deletion (regardless of the centrality of the node), small-world networks are more vulnerable to deletion of high centrality nodes due to the heterogeneous distribution of connections (Albert et al., 2000; Achard et al., 2006). Rather than a general vulnerability to deletion of high centrality nodes, patients with FCD showed a specific vulnerability to deletion of high participation coefficient nodes, which may indicate a selective reduction in inter-modular connections, a key component of efficient, small-world networks (Figure 5.4D). A reduction in inter-modular connections may be related to modularity, which was reduced bilaterally in FCD patients, although it only significantly differed from healthy controls in the contralateral hemisphere (Figure 5.3D).

Combined, our findings of decreased resilience and decreased global efficiency underscore the presence of a more regularized network in patients with FCD. In the context of mGluR5 availability, network regularization could signify a wide range of possible mechanisms affecting [^{11}C]ABP688 binding to mGluR5, including receptor internalization, the functional state of receptor (high/low affinity), the total amount of protein in the tissue, conformational changes, anomalous receptor isoforms, or excessive concentrations of endogenous ligands (Chugani et al., 1988; van Wieringen et al., 2013; Zimmer et al., 2015a; Vidal et al., 2016). We have previously suggested that reduced mGluR5 availability in the lesion may be related to excessive glutamate

concentrations, which when bound to the orthosteric site can cause a conformational change in mGluR5, making the transmembrane allosteric site unavailable for [^{11}C]ABP688 binding (Ametamey et al., 2007; Treyer et al., 2007; DeLorenzo et al., 2014; Zimmer et al., 2015b; DuBois et al., 2016a). While microdialysis studies have shown that extracellular glutamate concentrations in the seizure focus are elevated interictally (During and Spencer, 1993; Meurs et al., 2008; Cavus et al., 2016), glutamate concentrations beyond the lesion are unknown. However, it is possible that [^{11}C]ABP688 affinity may be similarly affected by divergent underlying mechanisms. For example, glutamate concentration may be increased in the seizure onset zone and regions fast recruited in seizure propagation, whereas mGluR5 may be internalized elsewhere in the brain as a compensatory mechanism, both of which would lead to reduced mGluR5 availability as measured by [^{11}C]ABP688 PET. This hypothesis is supported by our previous finding that extra-lesional regions of reduced mGluR5 availability were not associated with a poorer post-surgical prognosis in operated MRI positive FCD patients (DuBois et al., 2016a).

It is also important to note that mGluR5 availability fluctuates dynamically based on the factors discussed above. This fluctuation is supported by our finding of increased modularity in the ipsilateral hemisphere following recent seizures, which may suggest that seizure occurrence is associated with network randomization. This contrasts with the more regular network that was observed overall in FCD patients as compared to healthy controls. Graph theoretical analysis of electrocorticogram data shows that ipsilateral networks in patients with focal epilepsy become more random at seizure termination, and return to a more regular network interictally, as observed here (Kramer

et al., 2010; Kramer and Cash, 2012). Unfortunately, we did not find a significant relationship with any other network metrics to support the hypothesis that the ipsilateral network is more random following recent seizures.

Although network properties were not associated with the duration of epilepsy or age at disease onset, this does not imply that no relationship exists. In separate studies, decreased local clustering and increased path length have been associated with a longer duration of temporal lobe epilepsy (van Dellen et al., 2009; Bernhardt et al., 2011).

A significant limitation of this work was the small number of patients evaluated and the variable anatomical locations of the FCD lesions. A larger sample of patients with a wider range of clinical characteristics would allow for more robust comparisons. In addition, a large patient population would provide greater control for potential confounds relevant to mGluR5 PET imaging, such as cigarette smoking, psychiatric disorders, antiepileptic drug load, and sleep deprivation (Deschwanden et al., 2011; Akkus et al., 2013; Hefti et al., 2013).

In conclusion, we provide the first evidence for widespread mGluR5 abnormalities affecting network integration in patients with FCD. Our findings of bilaterally reduced network efficiency and resilience indicate that the mGluR5 network may be more regularized in patients with FCD. However, local difference between patients with FCD and healthy controls, as well as the relationship between the mGluR5 network and clinical characteristics may require a larger sample to be further elucidated. It might be also important to evaluate focal epilepsy patients without FCDs. These findings support the concept that FCD may be better characterized as a system-wide

disorder, rather than a focal abnormality. Furthermore, the graph theoretic approach employed here allows for neuroreceptor systems, such as mGluR5, to be compared to measures of functional and structural connectivity. This multimodal approach may, indeed, provide a more comprehensive description of network alterations and lead to novel diagnostic and therapeutic applications.

Chapter 6

Conclusions

This thesis describes a series of PET imaging studies investigating mGluR5 availability in healthy individuals and in patients with FCD. This work significantly contributes to the characterization of the PET radioligand [^{11}C]ABP688 in human subjects. In addition, due to the location and structure of the lesions, we developed advanced methods from MRI morphometry and other modalities to accurately assess the distribution of [^{11}C]ABP688 PET data. Using these methods, we first described mGluR5 availability in healthy controls. Next, we assessed regional and network-wide mGluR5 abnormalities in FCD patients with varying structural and pathological features. Below, we discuss the key findings from each study, as well as their significance and possible future directions.

Study 1. Characterization of age/sex, and the regional distribution of mGluR5 availability in the healthy human brain measured by high-resolution [^{11}C]ABP688 PET

In order to investigate mGluR5 abnormalities in patients with FCD, it was first necessary to characterize mGluR5 availability in healthy individuals. Using high-resolution PET imaging, we described in precise detail the regional distribution of

mGluR5 availability in the cortex and subcortical structures. We did not find a statistically significant effect of age or sex on mGluR5 availability, suggesting that mGluR5 availability was stable across the healthy adult lifespan and does not differ between sexes. These findings allow for an unmatched control group to be utilized for case-control comparison studies, which may aid assessment of mGluR5 abnormalities in a wide range of patient populations.

The lack of an age and sex effects on mGluR5 availability was recently replicated, confirming our results in a slightly larger sample with the mGluR5 ligand [^{18}F]FPEB (Mecca et al., 2017). There is growing evidence from animal and human studies that stable mGluR5 levels may be associated with healthy aging (Menard and Quirion, 2012; Leuzy et al., 2015). mGluR5 plays a key role in learning and memory, showing high availability in the hippocampus, and therefore may provide a suitable biomarker for neurodegenerative disease or other forms of cognitive decline (Conn, 2003). If similar data acquisition and image processing steps were followed, the mGluR5 availability distribution map presented here could serve as an age invariant comparison template for diagnostic or research purposes.

Recently, Hefti and colleagues showed that mGluR5 availability increased significantly after one night without sleep in a group of healthy controls (Hefti et al., 2013). It has been suggested that as extracellular glutamate levels decline throughout the day, mGluR5 availability may increase, resulting in a diurnal variation, which may underlie test-retest variability, when done on the same day (DeLorenzo et al., 2016). In addition to sleep deprivation and known confounds such as drug or nicotine use, further research in healthy individuals is needed to understand sources of variation that could

affect group or case-control comparisons.

Furthermore, we developed a novel partial volume correction method, building on previous MRI-based analyses. This method involved calculating regional estimates of partial volume corrected radioactivity using the geometric transfer matrix method (Rousset et al., 1998). In a previous study, the geometric transfer matrix regional estimates were used as weights to calculate voxel-wise partial volume corrected values with a group-wise anatomical segmentation of the cortex (Thomas et al., 2011). As the cortical distribution of [^{11}C]ABP688 was unknown prior to our analyses, we developed a data-driven method, which uniquely segmented the cortex of each individual based on the uncorrected radioactivity. From this segmentation, region-based partial volume correction was then performed, as described by Thomas et al. (2011). Comparitive analysis of our data-driven method showed lower variability of BP_{ND} values relative to a widely used partial volume correction method that does not segment regions of the cortex.

Therefore, our data-driven partial volume correction method allowed for accurate measurement of [^{11}C]ABP688 binding in patients with FCD, and may be further utilized in complex structural abnormalities such as traumatic brain injury, neurodegenerative disorders, and other types of malformations. In addition to being used in the subsequent thesis studies, this analysis has already been utilized in studies of patients with frontotemporal dementia and mesial temporal lobe epilepsy (Leuzy et al., 2015).

Study 2. mGluR5 cortical abnormalities in focal cortical dysplasia identified in vivo with [^{11}C]ABP688 PET imaging

Using the analytical framework developed in the first study, we describe, for the first time, *in vivo* mGluR5 abnormalities in FCD previously limited to the scope of surgical samples in selected patients. In 70% of patients, reduced mGluR5 availability was found within the radiologically identified dysplastic lesion as compared to homotopic areas in healthy controls. Reduced mGluR5 availability was associated with negative to weak mGluR5 immunoreactivity in balloon cells identified in the tissue resected during surgery for 4/5 patients. In addition, the majority of patients showed reduced mGluR5 availability extra-lesionally that was not associated with a visible structural abnormality, and did not impact post-operative prognosis. Overall, these results suggest that patients with FCD may have focal glutamatergic alterations that extend beyond the seizure focus.

Reduced mGluR5 availability as measurable by [^{11}C]ABP688 PET may be due to a range of molecular mechanisms including receptor internalization, the amount of protein in the tissue, and receptor conformational changes (Chugani et al., 1988; van Wieringen et al., 2013; DeLorenzo et al., 2014; Zimmer et al., 2015a; Vidal et al., 2016). Here, we suggested that excessive extracellular glutamate, which has been shown to induce a conformational change in mGluR5 and is known to be interictally elevated in FCD (DeLorenzo et al., 2014; Zimmer et al., 2015b; Cavus et al., 2016), may play a key role in reducing mGluR5 availability within the dysplastic lesion. However, additional research, including quantitative receptor autoradiography and microdialysis techniques, are needed to support this hypothesis.

Currently [^{18}F]FDG is the primary radioligand for diagnostic PET imaging of epilepsy patients for whom clinical MRI was inconclusive. While interictal [^{18}F]FDG PET is highly sensitive in patients with temporal lobe epilepsy, it is less effective in extra-temporal regions (Juhasz et al., 2001; Rathore et al., 2014). Although [^{11}C]ABP688 and [^{18}F]FDG PET have yet to be directly compared, our analysis of FCD patients did not show systematic regional variability, suggesting that [^{11}C]ABP688 may be an effective diagnostic tool in suspected extra-temporal cases. However, such conclusions would require prospective quantitative comparisons of [^{11}C]ABP688 and [^{18}F]FDG PET, as well as studies of the diagnostic utility of [^{11}C]ABP688 PET in clinical preoperative evaluation.

One of the primary functions of mGluR5 is to trigger protein synthesis via the mTOR pathway, leading to long-term potentiation and depression. Growing evidence indicates that brain somatic mutations in mTOR and genes encoding components of the mTOR pathway are involved in the pathogenesis of FCD (Baulac, 2016). However, current mTOR therapeutic inhibitors are not specific to the central nervous system, increasing their side effects and limiting their efficacy (Citraro et al., 2016). mGluR5, which is currently being investigated for a wide range of neurological disorders, may be a more suitable target for modulation of mTOR activity in the brain (Conn, 2003). Should therapies become available, [^{11}C]ABP688 PET may serve as a diagnostic tool for identifying patients who could benefit from mGluR5 targeted therapies, monitor disease progression, predict outcomes, and distinguish different clinical subclasses. In general [^{11}C]ABP688 PET may shed light on a wide range of neurological disorders, including several forms of epilepsy, leading to diagnostic and therapeutic applications.

Study 3. Reduced efficiency of the mGluR5 network in patients with focal cortical dysplasia: a graph-theoretical analysis of [^{11}C]ABP688 PET

To investigate network-wide mGluR5 abnormalities, we performed graph-theoretical analysis based on the inter-regional similarity of [^{11}C]ABP688 PET. Patients with FCD showed both ipsilateral and contralateral reductions in network efficiency and resilience to targeted nodal attacks. In addition, reduced network modularity and small-world index were found in the contralateral hemisphere of patients with FCD. Overall, these findings suggest that patients with FCD possess a more regularized mGluR5 network, meaning that patients showed fewer similarities in mGluR5 availability between distant network nodes than the healthy control group. While these findings are supported by several studies in patients with non-lesional neocortical and temporal lobe epilepsy, they conflict with the only other graph theoretical analysis of FCD, which described increased network efficiency using neurophysiological measures (Bernhardt et al., 2011; Vaessen et al., 2012; Jeong et al., 2014).

Several lines of evidence from both human and animal models indicate that chronic seizures result in progressive and widespread network alterations (Norden and Blumenfeld, 2002; Cavazos et al., 2004). A more regularized functional network, similar to the mGluR5 network described here, has been associated with cognitive decline in patients with temporal lobe epilepsy (Vlooswijk et al., 2011). mGluR5 network abnormalities may be a symptom of chronic seizures, although the extended duration of epilepsy in our patient population made the association with network efficiency difficult to assess. However, a longitudinal study or larger patient group with a wider range of clinical characteristics may reveal progressive network alterations. In addition to

providing a potential biomarker of disease progression, network analysis of mGluR5 availability may allow for more tailored surgical planning and assessment of treatment outcomes by identifying vulnerable brain regions beyond the seizure focus or regions of structural abnormality.

To our knowledge, this is the first graph theoretical analysis of a whole-brain neuroreceptor network. As a neuromodulatory glutamate receptor, mGluR5 may provide insights into the functional role of connectional topology (Sporns, 2016). As graph theoretical analysis and mGluR5 PET imaging are both new areas of research, additional multimodal analyses are needed to more fully characterize the relationship between functional, structural, and mGluR5 networks. Moreover, studies of temporal lobe epilepsy and non-lesional neocortical epilepsy using graph theoretical analysis of mGluR5 availability would provide added context for modality differences in network structure, as these patient groups have been more fully studied with functional and structural measures.

References

Achard S, Bullmore E (2007) Efficiency and cost of economical brain functional networks. PLoS computational biology 3:e17.

Achard S, Salvador R, Whitcher B, Suckling J, Bullmore E (2006) A resilient, low-frequency, small-world human brain functional network with highly connected association cortical hubs. Journal of Neuroscience 26:63-72.

Akbar MT, Rattray M, Powell JF, Meldrum BS (1996) Altered expression of group I metabotropic glutamate receptors in the hippocampus of amygdala-kindled rats. Molecular brain research 43:105-116.

Akkus F, Ametamey SM, Treyer V, Burger C, Johayem A, Umbricht D, Gomez Mancilla B, Sovago J, Buck A, Hasler G (2013) Marked global reduction in mGluR5 receptor binding in smokers and ex-smokers determined by [11C]ABP688 positron emission tomography. Proceedings of the national academy of sciences of the United States of America 110:737-742.

Alagarsamy S, Marino MJ, Rouse ST, Gereau RWt, Heinemann SF, Conn PJ (1999) Activation of NMDA receptors reverses desensitization of mGluR5 in native and recombinant systems. Nature neuroscience 2:234-240.

Albert R, Jeong H, Barabási A-L (2000) Error and attack tolerance of complex networks. Nature 406:378-382.

Alexander GM, Godwin DW (2006) Metabotropic glutamate receptors as a strategic target for the treatment of epilepsy. Epilepsy research 71:1-22.

Alstott J, Breakspear M, Hagmann P, Cammoun L, Sporns O (2009) Modeling the impact of lesions in the human brain. PLoS computational biology 5:e1000408.

Ametamey SM (2006) Radiosynthesis and Preclinical Evaluation of 11C-ABP688 as a Probe for Imaging the Metabotropic Glutamate Receptor Subtype 5. Journal of nuclear medicine 47:698–705.

Ametamey SM, Treyer V, Streffer J, Wyss MT, Schmidt M, Blagoev M, Hintermann S, Auberson Y, Gasparini F, Fischer UC, Buck A (2007) Human PET studies of metabotropic glutamate receptor subtype 5 with 11C-ABP688. Journal of nuclear medicine 48:247-252.

Ango F, Pin JP, Tu JC, Xiao B, Worley PF, Bockaert J, Fagni L (2000) Dendritic and axonal targeting of type 5 metabotropic glutamate receptor is regulated by Homer1 proteins and neuronal excitation. Journal of Neuroscience 20:8710-8716.

Anwyl R (1999) Metabotropic glutamate receptors: electrophysiological properties and role in plasticity. Brain Res Brain Res Rev 29:83-120.

Aronica E, Gorter JA, Jansen GH, van Veelen CW, van Rijen PC, Ramkema M, Troost D (2003) Expression and cell distribution of group I and group II metabotropic glutamate receptor subtypes in taylor-type focal cortical dysplasia. Epilepsia 44:785-795.

Ashburner J, Friston KJ (2005) Unified segmentation. NeuroImage 26:839-851.

Bahi-Buisson N, Poirier K, Fourniol F, Saillour Y, Valence S, Lebrun N, Hully M, Bianco CF, Boddaert N, Elie C, Lascelles K, Souville I, Consortium LI-T, Beldjord C, Chelly J (2014) The wide spectrum of tubulinopathies: what are the key features for the diagnosis? Brain 137:1676-1700.

Barkovich AJ, Kuzniecky RI, Jackson GD, Guerrini R, Dobyns WB (2001) Classification system for malformations of cortical development: Update 2001. Neurology 57:2168-2178.
Barkovich AJ, Kuzniecky RI, Jackson GD, Guerrini R, Dobyns WB (2005) A developmental and genetic classification for malformations of cortical development. Neurology 65:1873-1887.
Barkovich AJ, Guerrini R, Kuzniecky RI, Jackson GD, Dobyns WB (2012) A developmental and genetic classification for malformations of cortical development: update 2012. Brain 135:1348-1369.
Barkovich AJK, R. I.; Jackson, G. D. (1995) A Classification Scheme for Malformations of Cortical Development. Neuropediatrics 27.
Barkovich JA, Kuzniecky RI (2000) Gray matter heterotopia. Neurology 55:1603-1608.
Bassett DS, Bullmore E, Verchinski BA, Mattay VS, Weinberger DR, Meyer-Lindenberg A (2008) Hierarchical organization of human cortical networks in health and schizophrenia. Journal of Neuroscience 28:9239-9248.
Bast T, Oezkan O, Rona S, Stippich C, Seitz A, Rupp A, Fauser S, Zentner J, Rating D, Scherg M (2004) EEG and MEG source analysis of single and averaged interictal spikes reveals intrinsic epileptogenicity in focal cortical dysplasia. Epilepsia 45:621-631.
Baulac S (2016) mTOR signaling pathway genes in focal epilepsies. Prog Brain Res 226:61-79.
Benarroch EE (2008) Metabotropic glutamate receptors: synaptic modulators and therapeutic targets for neurologic disease. Neurology 70:964-968.
Benjamini Y, Hochberg Y (1995) Controlling the False Discovery Rate: a Practical and Powerful Approach to Multiple Testing. Journal of the Royal Statistical Society 57:289-300.
Benjamini Y, Krieger AM, Yekutieli D (2006) Adaptive linear step-up procedures that control the false discovery rate. Biometrika 93:491-507.
Bernhardt BC, Chen Z, He Y, Evans AC, Bernasconi N (2011) Graph-theoretical analysis reveals disrupted small-world organization of cortical thickness correlation networks in temporal lobe epilepsy. Cerebral cortex 21:2147-2157.
Besseling RM, Jansen JF, de Louw AJ, Vlooswijk MC, Hoeberigs MC, Aldenkamp AP, Backes WH, Hofman PA (2016) Abnormal Profiles of Local Functional Connectivity Proximal to Focal Cortical Dysplasias. PloS one 11:e0166022.
Besson P, Andermann F, Dubeau F, Bernasconi A (2008) Small focal cortical dysplasia lesions are located at the bottom of a deep sulcus. Brain 131:3246-3255.
Bianchi MT, Alexander BM, Cash SS (2009a) Incorporating uncertainty into medical decision making: an approach to unexpected test results. Medical decision making : an international journal of the Society for Medical Decision Making 29:116-124.
Bianchi R, Chuang SC, Zhao W, Young SR, Wong RK (2009b) Cellular plasticity for group I mGluR-mediated epileptogenesis. Journal of Neuroscience 29:3497-3507.
Blondel VD, Guillaume J-L, Lambiotte R, Lefebvre E (2008) Fast unfolding of communities in large networks. Journal of statistical mechanics: theory and experiment 2008:P10008.

Blumcke I et al. (2011) The clinicopathologic spectrum of focal cortical dysplasias: a consensus classification proposed by an ad hoc Task Force of the ILAE Diagnostic Methods Commission. Epilepsia 52:158-174.
Brodie MJ (2013) Road to refractory epilepsy: the Glasgow story. Epilepsia 54 Suppl 2:5-8.
Budday S, Steinmann P, Kuhl E (2015) Physical biology of human brain development. Frontiers in Cellular Neuroscience 9:257.
Burger C, Deschwanden A, Ametamey S, Johayem A, Mancosu B, Wyss M, Hasler G, Buck A (2010) Evaluation of a bolus/infusion protocol for 11 C-ABP688, a PET tracer for mGluR5. Nuclear medicine and biology 37:845-851.
Butler T, Ichise M, Teich AF, Gerard E, Osborne J, French J, Devinsky O, Kuzniecky R, Gilliam F, Pervez F, Provenzano F, Goldsmith S, Vallabhajosula S, Stern E, Silbersweig D (2013) Imaging inflammation in a patient with epilepsy due to focal cortical dysplasia. Journal of neuroimaging 23:129-131.
Caciagli L, Bernhardt BC, Hong SJ, Bernasconi A, Bernasconi N (2014) Functional network alterations and their structural substrate in drug-resistant epilepsy. Frontiers in human neuroscience 8:411.
Car H, Stefaniuk R, Wiśniewska R (2006) Effect of MPEP in Morris water maze in adult and old rats. Pharmacological reports: PR 59:88-93.
Cartmell J, Schoepp DD (2000) Regulation of neurotransmitter release by metabotropic glutamate receptors. Journal of neurochemistry 75:889-907.
Catania MV, D'Antoni S, Bonaccorso CM, Aronica E, Bear MF, Nicoletti F (2007) Group I Metabotropic Glutamate Receptors: A Role in Neurodevelopmental Disorders? Molecular Neurobiology 35:298-307.
Cavazos JE, Jones SM, Cross DJ (2004) Sprouting and synaptic reorganization in the subiculum and CA1 region of the hippocampus in acute and chronic models of partial-onset epilepsy. Neuroscience 126:677-688.
Cavus I, Romanyshyn JC, Kennard JT, Farooque P, Williamson A, Eid T, Spencer SS, Duckrow R, Dziura J, Spencer DD (2016) Elevated basal glutamate and unchanged glutamine and GABA in refractory epilepsy: Microdialysis study of 79 patients at the yale epilepsy surgery program. Annals of neurology 80:35-45.
Chassoux F, Devaux B, Landré E, Turak B, Nataf F, Varlet P, Chodkiewicz J-P, Daumas-Duport C (2000) Stereoelectroencephalography in focal cortical dysplasia A 3D approach to delineating the dysplastic cortex. Brain 123:1733-1751.
Chassoux F, Rodrigo S, Semah F, Beuvon F, Landre E, Devaux B, Turak B, Mellerio C, Meder JF, Roux FX, Daumas-Duport C, Merlet P, Dulac O, Chiron C (2010) FDG-PET improves surgical outcome in negative MRI Taylor-type focal cortical dysplasias. Neurology 75:2168-2175.
Chiang S, Haneef Z (2014) Graph theory findings in the pathophysiology of temporal lobe epilepsy. Clinical neurophysiology 125:1295-1305.
Choi H, Kim YK, Oh SW, Im HJ, Hwang do W, Kang H, Lee B, Lee YS, Jeong JM, Kim EE, Chung JK, Lee DS (2014) In vivo imaging of mGluR5 changes during epileptogenesis using [11C]ABP688 PET in pilocarpine-induced epilepsy rat model. PloS one 9:e92765.

Chugani DC, Ackermann RF, Phelps ME (1988) In vivo [3H] spiperone binding: evidence for accumulation in corpus striatum by agonist-mediated receptor internalization. Journal of cerebral blood flow and metabolism 8:291-303.
Citraro R, Leo A, Constanti A, Russo E, De Sarro G (2016) mTOR pathway inhibition as a new therapeutic strategy in epilepsy and epileptogenesis. Pharmacological research 107:333-343.
Comtat C, Sureau F, Sibomana M, Hong I, Sjoholm N, Trebossen R (2008) Image based resolution modeling for the HRRT OSEM reconstructions software. In: Nuclear Science Symposium Conference Record, 2008. NSS'08. IEEE, pp 4120-4123: IEEE.
Conn PJ (2003) Physiological roles and therapeutic potential of metabotropic glutamate receptors. Annals of the New York Academy of Sciences 1003:12-21.
Conn PJ, Pin JP (1997) Pharmacology and functions of metabotropic glutamate receptors. Annual review of pharmacology and toxicology 37:205-237.
Costes N, Dagher A, Larcher K, Evans AC, Collins DL, Reilhac A (2009) Motion correction of multi-frame PET data in neuroreceptor mapping: simulation based validation. NeuroImage 47:1496-1505.
Crino PB, Duhaime AC, Baltuch G, White R (2001) Differential expression of glutamate and GABA-A receptor subunit mRNA in cortical dysplasia. Neurology 56:906-913.
Daggett L, Sacaan A, Akong M, Rao S, Hess S, Liaw C, Urrutia A, Jachec C, Ellis S, Dreessen J (1995) Molecular and functional characterization of recombinant human metabotropic glutamate receptor subtype 5. Neuropharmacology 34:871-886.
Dale AM, Fischl B, Sereno MI (1999) Cortical surface-based analysis. I. Segmentation and surface reconstruction. NeuroImage 9:179-194.
Dansereau CL, Bellec P, Lee K, Pittau F, Gotman J, Grova C (2014) Detection of abnormal resting-state networks in individual patients suffering from focal epilepsy: an initial step toward individual connectivity assessment. Frontiers in human neuroscience 8:419.
DeLorenzo C, Kumar JS, Mann JJ, Parsey RV (2011a) In vivo variation in metabotropic glutamate receptor subtype 5 binding using positron emission tomography and [11C]ABP688. Journal of cerebral blood flow and metabolism 31:2169-2180.
DeLorenzo C, Milak MS, Brennan KG, Kumar JS, Mann JJ, Parsey RV (2011b) In vivo positron emission tomography imaging with [(1)(1)C]ABP688: binding variability and specificity for the metabotropic glutamate receptor subtype 5 in baboons. European journal of nuclear medicine and molecular imaging 38:1083-1094.
DeLorenzo C, Gallezot J-D, Gardus J, Yang J, Planeta B, Nabulsi N, Ogden RT, Labaree DC, Huang YH, Mann JJ (2016) In vivo variation in same-day estimates of metabotropic glutamate receptor subtype 5 binding using [11C] ABP688 and [18F] FPEB. Journal of cerebral blood flow and metabolism:0271678X16673646.
DeLorenzo C, DellaGioia N, Bloch M, Sanacora G, Nabulsi N, Abdallah C, Yang J, Wen R, John Mann J, Krystal JH, Parsey RV, Carson RE, Esterlis I (2014) In vivo ketamine-induced changes in [11C]ABP688 binding to metabotropic glutamate receptors subtype 5. Biological Psychiatry.
Deschwanden A, Karolewicz B, Feyissa AM, Treyer V, Ametamey SM, Johayem A, Burger C, Auberson YP, Sovago J, Stockmeier CA, Buck A, Hasler G (2011)

Reduced metabotropic glutamate receptor 5 density in major depression determined by [(11)C]ABP688 PET and postmortem study. American journal of psychiatry 168:727-734.
Desikan RS, Barkovich AJ (2016) Malformations of cortical development. Annals of neurology 80:797-810.
Desikan RS, Segonne F, Fischl B, Quinn BT, Dickerson BC, Blacker D, Buckner RL, Dale AM, Maguire RP, Hyman BT, Albert MS, Killiany RJ (2006) An automated labeling system for subdividing the human Cerebral cortex on MRI scans into gyral based regions of interest. NeuroImage 31:968-980.
Destrieux C, Fischl B, Dale A, Halgren E (2010) Automatic parcellation of human cortical gyri and sulci using standard anatomical nomenclature. NeuroImage 53:1-15.
Dölen G, Bear MF (2008) Role for metabotropic glutamate receptor 5 (mGluR5) in the pathogenesis of fragile X syndrome. The Journal of physiology 586:1503-1508.
DuBois JM, Rousset OG, Guiot MC, Hall JA, Reader AJ, Soucy JP, Rosa-Neto P, Kobayashi E (2016a) Metabotropic Glutamate Receptor Type 5 (mGluR5) Cortical Abnormalities in Focal Cortical Dysplasia Identified In Vivo With [11C]ABP688 Positron-Emission Tomography (PET) Imaging. Cerebral cortex 26:4170-4179.
DuBois JM, Rousset OG, Rowley J, Porras-Betancourt M, Reader AJ, Labbe A, Massarweh G, Soucy JP, Rosa-Neto P, Kobayashi E (2016b) Characterization of age/sex and the regional distribution of mGluR5 availability in the healthy human brain measured by high-resolution [(11)C]ABP688 PET. European journal of nuclear medicine and molecular imaging 43:152-162.
Duchowny M, Jayakar P, Levin B (2000) Aberrant neural circuits in malformations of cortical development and focal epilepsy. Neurology 55:423-428.
During MJ, Spencer DD (1993) Extracellular hippocampal glutamate and spontaneous seizure in the conscious human brain. Lancet 341:1607-1610.
Eid T, Thomas MJ, Spencer DD, Rundén-Pran E, Lai JCK, Malthankar GV, Kim JH, Danbolt NC, Ottersen OP, de Lanerolle NC (2004) Loss of glutamine synthetase in the human epileptogenic hippocampus: possible mechanism for raised extracellular glutamate in mesial temporal lobe epilepsy. The Lancet 363:28-37.
Elmenhorst D, Minuzzi L, Aliaga A, Rowley J, Massarweh G, Diksic M, Bauer A, Rosa-Neto P (2010) In vivo and in vitro validation of reference tissue models for the mGluR(5) ligand [(11)C]ABP688. Journal of cerebral blood flow and metabolism 30:1538-1549.
Elmenhorst D, Mertens K, Kroll T, Oskamp A, Ermert J, Elmenhorst EM, Wedekind F, Beer S, Coenen HH, Bauer A (2016) Circadian variation of metabotropic glutamate receptor 5 availability in the rat brain. Journal of sleep research 25:754-761.
Elston GN (2002) Cortical heterogeneity: implications for visual processing and polysensory integration. Journal of neurocytology 31:317-335.
Elston GN, Rockland KS (2002) The pyramidal cell of the sensorimotor cortex of the macaque monkey: phenotypic variation. Cerebral cortex 12:1071-1078.
Engman J, Ahs F, Furmark T, Linnman C, Pissiota A, Appel L, Frans O, Langstrom B, Fredrikson M (2012) Age, sex and NK1 receptors in the human brain -- a positron emission tomography study with [(1)(1)C]GR205171. European neuropsychopharmacology 22:562-568.

Erlandsson K, Buvat I, Pretorius PH, Thomas BA, Hutton BF (2012) A review of partial volume correction techniques for emission tomography and their applications in neurology, cardiology and oncology. Physics in medicine and biology 57:R119-159.
Field JR, Walker AG, Conn PJ (2011) Targeting glutamate synapses in schizophrenia. Trends in molecular medicine 17:689-698.
Fischl B, Dale AM (2000) Measuring the thickness of the human Cerebral cortex from magnetic resonance images. Proceedings of the national academy of sciences of the United States of America 97:11050-11055.
Fischl B, Sereno MI, Dale AM (1999a) Cortical surface-based analysis. II: Inflation, flattening, and a surface-based coordinate system. NeuroImage 9:195-207.
Fischl B, Liu A, Dale AM (2001) Automated manifold surgery: constructing geometrically accurate and topologically correct models of the human Cerebral cortex. IEEE Trans Med Imaging 20:70-80.
Fischl B, Sereno MI, Tootell RBH, Dale AM (1999b) High-resolution intersubject averaging and a coordinate system for the cortical surface. Human brain mapping 8:272--284.
Fischl B, Salat DH, Busa E, Albert M, Dieterich M, Haselgrove C, van der Kouwe A, Killiany R, Kennedy D, Klaveness S, Montillo A, Makris N, Rosen B, Dale AM (2002) Whole brain segmentation: automated labeling of neuroanatomical structures in the human brain. Neuron 33:341-355.
Flint AC, Dammerman RS, Kriegstein AR (1999) Endogenous activation of metabotropic glutamate receptors in neocortical development causes neuronal calcium oscillations. Proceedings of the national academy of sciences of the United States of America 96:12144-12149.
Fowler J, Volkow N, Wang G-J, Logan J, Pappas N, Shea C, MacGregor R (1997) Age-related increases in brain monoamine oxidase B in living healthy human subjects. Neurobiology of aging 18:431-435.
Frater JL, Prayson RA, Morris III HH, Bingaman WE (2000) Surgical pathologic findings of extratemporal-based intractable epilepsy: a study of 133 consecutive resections. Archives of pathology and laboratory medicine 124:545-549.
Gomeza J, Joly C, Kuhn R, Knopfel T, Bockaert J, Pin JP (1996) The second intracellular loop of metabotropic glutamate receptor 1 cooperates with the other intracellular domains to control coupling to G-proteins. Journal of biological chemistry 271:2199-2205.
Gratton C, Nomura EM, Perez F, D'Esposito M (2012) Focal brain lesions to critical locations cause widespread disruption of the modular organization of the brain. Journal of cognitive neuroscience 24:1275-1285.
Greve DN, Fischl B (2009) Accurate and robust brain image alignment using boundary-based registration. NeuroImage 48:63-72.
Greve DN, Van der Haegen L, Cai Q, Stufflebeam S, Sabuncu MR, Fischl B, Brysbaert M (2013) A surface-based analysis of language lateralization and cortical asymmetry. Journal of cognitive neuroscience 25:1477-1492.
Greve DN, Svarer C, Fisher PM, Feng L, Hansen AE, Baare W, Rosen B, Fischl B, Knudsen GM (2014) Cortical surface-based analysis reduces bias and variance in kinetic modeling of brain PET data. NeuroImage 92:225-236.

Grove-Strawser D, Boulware MI, Mermelstein PG (2010) Membrane estrogen receptors activate the metabotropic glutamate receptors mGluR5 and mGluR3 to bidirectionally regulate CREB phosphorylation in female rat striatal neurons. Neuroscience 170:1045-1055.

Guerrini R, Dobyns WB (2014) Malformations of cortical development: clinical features and genetic causes. The lancet neurology 13:710-726.
Figures 2.2 was reprinted from Lancet neurology, 13/7, Guerrini R, Dobyns WB, Malformations of cortical development: clinical features and genetic causes, 710-726, Copyright (2015), with permission from Elsevier.

Guerrini R, Dobyns WB, Barkovich AJ (2008) Abnormal development of the human Cerebral cortex: genetics, functional consequences and treatment options. Trends in neurosciences 31:154-162.

Gunn RN, Lammertsma AA, Hume SP, Cunningham VJ (1997) Parametric imaging of ligand-receptor binding in PET using a simplified reference region model. NeuroImage 6:279-287.

Hadel S, Wirth C, Rapp M, Gallinat J, Schubert F (2013) Effects of age and sex on the concentrations of glutamate and glutamine in the human brain. Journal of magnetic resonance imaging 38:1480-1487.

Hagler DJ, Jr., Saygin AP, Sereno MI (2006) Smoothing and cluster thresholding for cortical surface-based group analysis of fMRI data. NeuroImage 33:1093-1103.

Hammers A, Koepp MJ, Richardson MP, Hurlemann R, Brooks DJ, Duncan JS (2003) Grey and white matter flumazenil binding in neocortical epilepsy with normal MRI. A PET study of 44 patients. Brain 126:1300-1318.

Hammers A, Koepp MJ, Richardson MP, Labbe C, Brooks DJ, Cunningham VJ, Duncan JS (2001) Central benzodiazepine receptors in malformations of cortical development: A quantitative study. Brain 124:1555-1565.

Harvey AS, Cross JH, Shinnar S, Mathern GW, Taskforce IPESS (2008) Defining the spectrum of international practice in pediatric epilepsy surgery patients. Epilepsia 49:146-155.

He Y, Chen Z, Evans A (2008) Structural insights into aberrant topological patterns of large-scale cortical networks in Alzheimer's disease. Journal of neuroscience 28:4756-4766.

Hefti K, Holst SC, Sovago J, Bachmann V, Buck A, Ametamey SM, Scheidegger M, Berthold T, Gomez-Mancilla B, Seifritz E, Landolt HP (2013) Increased metabotropic glutamate receptor subtype 5 availability in human brain after one night without sleep. Biological psychiatry 73:161-168.

Hermann BP, Lin JJ, Jones JE, Seidenberg M (2009) The emerging architecture of neuropsychological impairment in epilepsy. Neurology Clinics 27:881-907.

Hermans E, Challiss RA (2001) Structural, signalling and regulatory properties of the group I metabotropic glutamate receptors: prototypic family C G-protein-coupled receptors. Biochemical journal 359:465-484.

Hintermann S, Vranesic I, Allgeier H, Brulisauer A, Hoyer D, Lemaire M, Moenius T, Urwyler S, Whitebread S, Gasparini F, Auberson YP (2007) ABP688, a novel selective and high affinity ligand for the labeling of mGlu5 receptors: identification, in vitro pharmacology, pharmacokinetic and biodistribution studies. Bioorganic and medicinal chemistry 15:903-914.

Hong I, Chung S, Kim H, Kim Y, Son Y, Cho Z (2007) Ultra fast symmetry and SIMD-based projection-backprojection (SSP) algorithm for 3-D PET image reconstruction. IEEE transactions on medical imaging 26:789-803.
Hong SJ, Kim H, Schrader D, Bernasconi N, Bernhardt BC, Bernasconi A (2014) Automated detection of cortical dysplasia type II in MRI-negative epilepsy. Neurology 83:48-55.
Horstmann MT, Bialonski S, Noennig N, Mai H, Prusseit J, Wellmer J, Hinrichs H, Lehnertz K (2010) State dependent properties of epileptic brain networks: comparative graph-theoretical analyses of simultaneously recorded EEG and MEG. Clinical neurophysiology 121:172-185.
Hothorn T, Hornik K, Van De Wiel MA, Zeileis A (2006) A Lego system for conditional inference. The American Statistician 60:257-263.
Hu Y, Xu Q, Li K, Zhu H, Qi R, Zhang Z, Lu G (2013) Gender differences of brain glucose metabolic networks revealed by FDG-PET: evidence from a large cohort of 400 young adults. PloS one 8:e83821.
Hubbard JA, Szu JI, Yonan JM, Binder DK (2016) Regulation of astrocyte glutamate transporter-1 (GLT1) and aquaporin-4 (AQP4) expression in a model of epilepsy. Experimental neurology 283:85-96.
Hulka LM, Treyer V, Scheidegger M, Preller KH, Vonmoos M, Baumgartner MR, Johayem A, Ametamey SM, Buck A, Seifritz E, Quednow BB (2014) Smoking but not cocaine use is associated with lower cerebral metabotropic glutamate receptor 5 density in humans. Molecular psychiatry 19:625-632.
Innis RB et al. (2007) Consensus nomenclature for in vivo imaging of reversibly binding radioligands. Journal of cerebral blood flow and metabolism 27:1533-1539.
Jansen AC, Robitaille Y, Honavar M, Mullatti N, Leventer RJ, Andermann E, Andermann F, Squier W (2016) The histopathology of polymicrogyria: a series of 71 brain autopsy studies. Developmental medicine and child neurology 58:39-48.
Jansen LA, Mirzaa GM, Ishak GE, O'Roak BJ, Hiatt JB, Roden WH, Gunter SA, Christian SL, Collins S, Adams C, Riviere JB, St-Onge J, Ojemann JG, Shendure J, Hevner RF, Dobyns WB (2015) PI3K/AKT pathway mutations cause a spectrum of brain malformations from megalencephaly to focal cortical dysplasia. Brain 138:1613-1628.
Jeong W, Jin SH, Kim M, Kim JS, Chung CK (2014) Abnormal functional brain network in epilepsy patients with focal cortical dysplasia. Epilepsy research 108:1618-1626.
Jones JE, Austin JK, Caplan R, Dunn D, Plioplys S, Salpekar JA (2008) Psychiatric disorders in children and adolescents who have epilepsy. Pediatrics in review / American academy of pediatrics 29:e9-14.
Juhasz C, Chugani D, Muzik O, Shah A, Shah J, Watson C, Canady A, Chugani HT (2001) Relationship of flumazenil and glucose PET abnormalities to neocortical epilepsy surgery outcome. Neurology 56:1650-1658.
Juhasz C, Asano E, Shah A, Chugani DC, Batista CE, Muzik O, Sood S, Chugani HT (2009) Focal decreases of cortical GABAA receptor binding remote from the primary seizure focus: what do they indicate? Epilepsia 50:240-250.
Kagedal M, Cselenyi Z, Nyberg S, Raboisson P, Stahle L, Stenkrona P, Varnas K, Halldin C, Hooker AC, Karlsson MO (2013) A positron emission tomography study in healthy volunteers to estimate mGluR5 receptor occupancy of AZD2066 -

estimating occupancy in the absence of a reference region. NeuroImage 82:160-169.
Kakita A, Hayashi S, Moro F, Guerrini R, Ozawa T, Ono K, Kameyama S, Walsh CA, Takahashi H (2002) Bilateral periventricular nodular heterotopia due to filamin 1 gene mutation: widespread glomeruloid microvascular anomaly and dysplastic cytoarchitecture in the Cerebral cortex. Acta neuropathologica 104:649-657.
Kandel E (2012) Principles of neural science, Fifth Editition, Kandel, ER; Schwartz, JH; Jessell TM and two more. In: McGraw Hill Medical.
Kandratavicius L, Rosa-Neto P, Monteiro MR, Guiot MC, Assirati JA, Jr., Carlotti CG, Jr., Kobayashi E, Leite JP (2013) Distinct increased metabotropic glutamate receptor type 5 (mGluR5) in temporal lobe epilepsy with and without hippocampal sclerosis. Hippocampus 23:1212-1230.
Kim SH, Markham JA, Weiler IJ, Greenough WT (2008) Aberrant early-phase ERK inactivation impedes neuronal function in fragile X syndrome. Proceedings of the national academy of sciences of the United States of America 105:4429-4434.
Kirschstein T, Bauer M, Müller L, Rüschenschmidt C, Reitze M, Becker AJ, Schoch S, Beck H (2007) Loss of metabotropic glutamate receptor-dependent long-term depression via downregulation of mGluR5 after status epilepticus. Journal of neuroscience 27:7696-7704.
Kniazeff J, Bessis AS, Maurel D, Ansanay H, Prezeau L, Pin JP (2004) Closed state of both binding domains of homodimeric mGlu receptors is required for full activity. Nature structural and molecular biology 11:706-713.
Kobayashi E, J. R, P. SJ, P. R-N (2010) Glutamatergic dysfunction underlying hypometabolism in temporal lobe epilepsy (TLE): a positron emission tomography (PET) multiparametric study. In: 64th Annual Meeting of the American Epilepsy Society. San Antonio, TX.
Kong XZ, Wang X, Huang L, Pu Y, Yang Z, Dang X, Zhen Z, Liu J (2014) Measuring individual morphological relationship of cortical regions. Journal of neuroscience methods 237:103-107.
Kong XZ, Liu Z, Huang L, Wang X, Yang Z, Zhou G, Zhen Z, Liu J (2015) Mapping Individual Brain Networks Using Statistical Similarity in Regional Morphology from MRI. PloS one 10:e0141840.
Kramer MA, Cash SS (2012) Epilepsy as a disorder of cortical network organization. The Neuroscientist : a review journal bringing neurobiology, neurology and psychiatry 18:360-372.
Kramer MA, Eden UT, Kolaczyk ED, Zepeda R, Eskandar EN, Cash SS (2010) Coalescence and fragmentation of cortical networks during focal seizures. Journal of neuroscience 30:10076-10085.
Kullback S, Leibler RA (1951) On information and sufficiency. The annals of mathematical statistics 22:79-86.
Lammertsma AA, Hume SP (1996) Simplified reference tissue model for PET receptor studies. NeuroImage 4:153-158.
Lammertsma AA, Bench CJ, Hume SP, Osman S, Gunn K, Brooks DJ, Frackowiak RS (1996) Comparison of methods for analysis of clinical [11C]raclopride studies. Journal of cerebral blood flow and metabolism 16:42-52.

Lamparello P, Baybis M, Pollard J, Hol EM, Eisenstat DD, Aronica E, Crino PB (2007) Developmental lineage of cell types in cortical dysplasia with balloon cells. Brain 130:2267-2276.
Laplante M, Sabatini DM (2012) mTOR signaling in growth control and disease. Cell 149:274-293.
Latora V, Marchiori M (2001) Efficient behavior of small-world networks. Physical review letters 87:198701.
Lee SK, Kim DI, Mori S, Kim J, Kim HD, Heo K, Lee BI (2004) Diffusion tensor MRI visualizes decreased subcortical fiber connectivity in focal cortical dysplasia. NeuroImage 22:1826-1829.
Lerner JT, Salamon N, Hauptman JS, Velasco TR, Hemb M, Wu JY, Sankar R, Donald Shields W, Engel J, Jr., Fried I, Cepeda C, Andre VM, Levine MS, Miyata H, Yong WH, Vinters HV, Mathern GW (2009) Assessment and surgical outcomes for mild type I and severe type II cortical dysplasia: a critical review and the UCLA experience. Epilepsia 50:1310-1335.
Leuzy A, Zimmer ER, Dubois J, Pruessner J, Cooperman C, Soucy JP, Kostikov A, Schirmaccher E, Desautels R, Gauthier S, Rosa-Neto P (2015) In vivo characterization of metabotropic glutamate receptor type 5 abnormalities in behavioral variant FTD. Brain structure and function 221:1387-1402.
Leventer R, Phelan E, Coleman L, Kean M, Jackson G, Harvey A (1999) Clinical and imaging features of cortical malformations in childhood. Neurology 53:715-715.
Lo CY, Su TW, Huang CC, Hung CC, Chen WL, Lan TH, Lin CP, Bullmore ET (2015) Randomization and resilience of brain functional networks as systems-level endophenotypes of schizophrenia. Proceedings of the national academy of sciences of the United States of America 112:9123-9128.
Madsen K, Haahr MT, Marner L, Keller SH, Baare WF, Svarer C, Hasselbalch SG, Knudsen GM (2011) Age and sex effects on 5-HT(4) receptors in the human brain: a [(11)C]SB207145 PET study. Journal of cerebral blood flow and metabolism 31:1475-1481.
Martinez D, Slifstein M, Nabulsi N, Grassetti A, Urban NB, Perez A, Liu F, Lin SF, Ropchan J, Mao X, Kegeles LS, Shungu DC, Carson RE, Huang Y (2014) Imaging glutamate homeostasis in cocaine addiction with the metabotropic glutamate receptor 5 positron emission tomography radiotracer [(11)C]ABP688 and magnetic resonance spectroscopy. Biological psychiatry 75:165-171.
Maslov S, Sneppen K (2002) Specificity and stability in topology of protein networks. Science 296:910-913.
Massobrio P, Pasquale V, Martinoia S (2015) Self-organized criticality in cortical assemblies occurs in concurrent scale-free and small-world networks. Scientific reports 5:10578.
Mathews WB, Kuwabara H, Stansfield K, Valentine H, Alexander M, Kumar A, Hilton J, Dannals RF, Wong DF, Gasparini F (2014) Dose-dependent, saturable occupancy of the metabotropic glutamate subtype 5 receptor by fenobam as measured with [C]ABP688 PET imaging. Synapse 68:565-573.
Matuskey D, Pittman B, Planeta-Wilson B, Walderhaug E, Henry S, Gallezot JD, Nabulsi N, Ding YS, Bhagwagar Z, Malison R, Carson RE, Neumeister A (2012)

Age effects on serotonin receptor 1B as assessed by PET. Journal of nuclear medicine 53:1411-1414.
McGinnity CJ, Koepp MJ, Hammers A, Riano Barros DA, Pressler RM, Luthra S, Jones PA, Trigg W, Micallef C, Symms MR, Brooks DJ, Duncan JS (2015) NMDA receptor binding in focal epilepsies. Journal of neurology, neurosurgery, and psychiatry 86:1150-1157.
Mecca AP, Rogers K, Jacobs Z, McDonald JW, Michalak HR, DellaGioia N, Nabulsi N, Matuskey D, Esterlis I, Carson RE (2017) Investigating Age Related Associations of Metabotropic Glutamate Receptor 5 Density Using [18F] FPEB and PET. The american journal of geriatric psychiatry 25:S96-S97.
Mehta A, Prabhakar M, Kumar P, Deshmukh R, Sharma P (2013) Excitotoxicity: bridge to various triggers in neurodegenerative disorders. European journal of pharmacology 698:6-18.
Menard C, Quirion R (2012) Successful cognitive aging in rats: a role for mGluR5 glutamate receptors, homer 1 proteins and downstream signaling pathways. PloS one 7:e28666.
Merlin LR (2002) Differential roles for mGluR1 and mGluR5 in the persistent prolongation of epileptiform bursts. Journal of neurophysiology 87:621-625.
Merlin LR, Wong RK (1997) Role of group I metabotropic glutamate receptors in the patterning of epileptiform activities in vitro. Journal of neurophysiology 78:539-544.
Meurs A, Clinckers R, Ebinger G, Michotte Y, Smolders I (2008) Seizure activity and changes in hippocampal extracellular glutamate, GABA, dopamine and serotonin. Epilepsy research 78:50-59.
Milella M, Reader A, Albrechtsons D, Minuzi L, Soucy J, Benkelfat C (2011) Human PET validation study of reference tissue models for the mGluR5 ligand [11C] ABP688. In: Society for Neuroscience Annual Meeting. Washington, DC.
Mohanraj R, Brodie MJ (2006) Diagnosing refractory epilepsy: response to sequential treatment schedules. European journal of neurology 13:277-282.
Moller RS et al. (2016) Germline and somatic mutations in the MTOR gene in focal cortical dysplasia and epilepsy. Neurology genetics 2:e118.
Morey RA, Petty CM, Xu Y, Hayes JP, Wagner HR, 2nd, Lewis DV, LaBar KS, Styner M, McCarthy G (2009) A comparison of automated segmentation and manual tracing for quantifying hippocampal and amygdala volumes. NeuroImage 45:855-866.
Moses-Kolko EL, Price JC, Shah N, Berga S, Sereika SM, Fisher PM, Coleman R, Becker C, Mason NS, Loucks T, Meltzer CC (2011) Age, sex, and reproductive hormone effects on brain serotonin-1A and serotonin-2A receptor binding in a healthy population. Neuropsychopharmacology 36:2729-2740.
Moutin E, Raynaud F, Roger J, Pellegrino E, Homburger V, Bertaso F, Ollendorff V, Bockaert J, Fagni L, Perroy J (2012) Dynamic remodeling of scaffold interactions in dendritic spines controls synaptic excitability. The Journal of cell biology 198:251-263.
Muller-Gartner HW, Links JM, Prince JL, Bryan RN, McVeigh E, Leal JP, Davatzikos C, Frost JJ (1992) Measurement of radiotracer concentration in brain gray matter using positron emission tomography: MRI-based correction for partial volume effects. Journal of cerebral blood flow and metabolism 12:571-583.

Nakahara K, Okada M, Nakanishi S (1997) The metabotropic glutamate receptor mGluR5 induces calcium oscillations in cultured astrocytes via protein kinase C phosphorylation. Journal of neurochemistry 69:1467-1475.
Nicoletti F, Bockaert J, Collingridge GL, Conn PJ, Ferraguti F, Schoepp DD, Wroblewski JT, Pin JP (2011) Metabotropic glutamate receptors: from the workbench to the bedside. Neuropharmacology 60:1017-1041.
Nicoletti FB, V. (1999) Group-I metabotropic glutamate receptors: hypotheses to explain their dual role in neurotoxicity and neuroprotection. Neuropharmacology 38.
Niswender CM, Conn PJ (2010) Metabotropic glutamate receptors: physiology, pharmacology, and disease. Annual review of pharmacology and toxicology 50:295-322.
Norden AD, Blumenfeld H (2002) The role of subcortical structures in human epilepsy. Epilepsy and behavior 3:219-231.
Notenboom RG, Hampson DR, Jansen GH, van Rijen PC, van Veelen CW, van Nieuwenhuizen O, de Graan PN (2006) Up-regulation of hippocampal metabotropic glutamate receptor 5 in temporal lobe epilepsy patients. Brain 129:96-107.
Palmini A, Andermann F, Olivier A, Tampieri D, Robitaille Y, Andermann E, Wright G (1991) Focal neuronal migration disorders and intractable partial epilepsy: a study of 30 patients. Annals of neurology 30:741-749.
Palmini A, Gambardella A, Andermann F, Dubeau F, da Costa JC, Olivier A, Tampieri D, Gloor P, Quesney F, Andermann E (1995) Intrinsic epileptogenicity of human dysplastic cortex as suggested by corticography and surgical results. Annals of neurology 37:476-487.
Palmini A, Najm I, Avanzini G, Babb T, Guerrini R, Foldvary-Schaefer N, Jackson G, Lüders H, Prayson R, Spreafico R (2004) Terminology and classification of the cortical dysplasias. Neurology 62:S2-S8.
Patel S, Hamill TG, Connolly B, Jagoda E, Li W, Gibson RE (2007) Species differences in mGluR5 binding sites in mammalian central nervous system determined using in vitro binding with [18F]F-PEB. Nuclear medicine and biology 34:1009-1017.
Pin JP, Kniazeff J, Liu J, Binet V, Goudet C, Rondard P, Prezeau L (2005) Allosteric functioning of dimeric class C G-protein-coupled receptors. The FEBS journal 272:2947-2955.
Prayson RA, Spreafico R, Vinters HV (2002) Pathologic characteristics of the cortical dysplasias. Neurosurgery clinics of north america 13:17-25.
Price DL, Rockenstein E, Ubhi K, Phung V, MacLean-Lewis N, Askay D, Cartier A, Spencer B, Patrick C, Desplats P (2010) Alterations in mGluR5 expression and signaling in Lewy body disease and in transgenic models of alpha-synucleinopathy–implications for excitotoxicity. PloS one 5:e14020.
R Core Team (2013) R: A Language and Environment for Statistical Computing. In. Vienna, Austria: R foundation for statistical computing.
Rathore C, Dickson JC, Teotonio R, Ell P, Duncan JS (2014) The utility of 18F-fluorodeoxyglucose PET (FDG PET) in epilepsy surgery. Epilepsy research 108:1306-1314.

Richardson M, Koepp M, Duncan J, Brooks D, Fish D (1996) Benzodiazepine receptors in focal epilepsy with cortical dysgenesis: An 11C-flumazenil PET study. Annals of neurology 40:188-198.
Rogawski MA, Löscher W (2004) The neurobiology of antiepileptic drugs. Nature reviews neuroscience 5:553-564.
Romano C, Sesma MA, McDonald CT, O'Malley K, Van den Pol AN, Olney JW (1995) Distribution of metabotropic glutamate receptor mGluR5 immunoreactivity in rat brain. Journal of comparative neurology 355:455-469.
Rong R, Ahn J-Y, Huang H, Nagata E, Kalman D, Kapp JA, Tu J, Worley PF, Snyder SH, Ye K (2003) PI3 kinase enhancer–Homer complex couples mGluRI to PI3 kinase, preventing neuronal apoptosis. Nature neuroscience 6:1153-1161.
Rosenblatt M (1956) Remarks on some nonparametric estimates of a density function. Annals of mathematical statistics 27:832-837.
Rousset O, Rahmim A, Alavi A, Zaidi H (2007) Partial Volume Correction Strategies in PET. PET Clinics 2:235-249.
Rousset OG, Ma Y, Evans AC (1998) Correction for partial volume effects in PET: principle and validation. Journal of nuclear medicine 39:904-911.
Rousset OG, Collins DL, Rahmim A, Wong DF (2008) Design and implementation of an automated partial volume correction in PET: application to dopamine receptor quantification in the normal human striatum. Journal of nuclear medicine 49:1097-1106.
Rowley HL, Marsden CA, Martin KF (1997) Generalised seizure-induced changes in rat hippocampal glutamate but not GABA release are potentiated by repeated seizures. Neuroscience letters 234:143-146.
Rubinov M, Sporns O (2010) Complex network measures of brain connectivity: uses and interpretations. NeuroImage 52:1059-1069.
Sailasuta N, Ernst T, Chang L (2008) Regional variations and the effects of age and gender on glutamate concentrations in the human brain. Magnetic resonance imaging 26:667-675.
Salamon N, Kung J, Shaw SJ, Koo J, Koh S, Wu JY, Lerner JT, Sankar R, Shields WD, Engel J, Jr., Fried I, Miyata H, Yong WH, Vinters HV, Mathern GW (2008) FDG-PET/MRI coregistration improves detection of cortical dysplasia in patients with epilepsy. Neurology 71:1594-1601.
Segonne F, Dale AM, Busa E, Glessner M, Salat D, Hahn HK, Fischl B (2004) A hybrid approach to the skull stripping problem in MRI. NeuroImage 22:1060-1075.
Segonne FP, J.; Fischl, B. (2007) Geometrically Accurate Topology-Correction of Cortical Surfaces Using Nonseparating Loops. IEEE transactions on medical imaging 26:518-529.
Sisodiya SM (2000) Surgery for malformations of cortical development causing epilepsy. Brain 123 (Pt 6):1075-1091.
Sisodiya SM, Fauser S, Cross JH, Thom M (2009) Focal cortical dysplasia type II: biological features and clinical perspectives. Lancet neurology 8:830-843.

Sporns O (2016) Connectome Networks: From Cells to Systems. In: Micro-, Meso-and Macro-Connectomics of the Brain, pp 107-127: Springer.
Sporns O, Zwi JD (2004) The small world of the Cerebral cortex. Neuroinformatics 2:145-162.
Stutterd CA, Leventer RJ (2014) Polymicrogyria: a common and heterogeneous malformation of cortical development. In: American Journal of Medical Genetics Part C: Seminars in Medical Genetics, pp 227-239: Wiley Online Library.
Sureau FC, Reader AJ, Comtat C, Leroy C, Ribeiro MJ, Buvat I, Trebossen R (2008) Impact of image-space resolution modeling for studies with the high-resolution research tomograph. Journal of nuclear medicine 49:1000-1008.
Tassi L, Colombo N, Garbelli R, Francione S, Lo Russo G, Mai R, Cardinale F, Cossu M, Ferrario A, Galli C, Bramerio M, Citterio A, Spreafico R (2002) Focal cortical dysplasia: neuropathological subtypes, EEG, neuroimaging and surgical outcome. Brain 125:1719-1732.
Taylor DC, Falconer MA, Bruton CJ, Corsellis JA (1971) Focal dysplasia of the Cerebral cortex in epilepsy. Journal of neurology, neurosurgery, and psychiatry 34:369-387.
Thesen T, Quinn BT, Carlson C, Devinsky O, DuBois J, McDonald CR, French J, Leventer R, Felsovalyi O, Wang X, Halgren E, Kuzniecky R (2011) Detection of epileptogenic cortical malformations with surface-based MRI morphometry. PloS one 6:e16430.
Thomas BA, Erlandsson K, Modat M, Thurfjell L, Vandenberghe R, Ourselin S, Hutton BF (2011) The importance of appropriate partial volume correction for PET quantification in Alzheimer's disease. European journal of nuclear medicine and molecular imaging 38:1104-1119.
Thornton R, Vulliemoz S, Rodionov R, Carmichael DW, Chaudhary UJ, Diehl B, Laufs H, Vollmar C, McEvoy AW, Walker MC, Bartolomei F, Guye M, Chauvel P, Duncan JS, Lemieux L (2011) Epileptic networks in focal cortical dysplasia revealed using electroencephalography-functional magnetic resonance imaging. Annals of neurology 70:822-837.
Treyer V, Streffer J, Wyss MT, Bettio A, Ametamey SM, Fischer U, Schmidt M, Gasparini F, Hock C, Buck A (2007) Evaluation of the metabotropic glutamate receptor subtype 5 using PET and 11C-ABP688: assessment of methods. Journal of nuclear medicine 48:1207-1215.
Tsamis KI, Mytilinaios DG, Njau SN, Baloyannis SJ (2013) Glutamate Receptors in Human Caudate Nucleus in Normal Aging and Alzheimer’s Disease. Current alzheimer research 10:469-475.
Tyvaert L, Hawco C, Kobayashi E, LeVan P, Dubeau F, Gotman J (2008) Different structures involved during ictal and interictal epileptic activity in malformations of cortical development: an EEG-fMRI study. Brain 131:2042-2060.
Uchida H, Chow TW, Mamo DC, Kapur S, Mulsant BH, Houle S, Pollock BG, Graff-Guerrero A (2011) Effects of aging on 5-HT(2A) R binding: a HRRT PET study with and without partial volume corrections. International journal of geriatric psychiatry 26:1300-1308.
Vaessen MJ, Jansen JF, Vlooswijk MC, Hofman PA, Majoie HJ, Aldenkamp AP, Backes WH (2012) White matter network abnormalities are associated with cognitive decline in chronic epilepsy. Cerebral cortex 22:2139-2147.

Valiente M, Marin O (2010) Neuronal migration mechanisms in development and disease. Current opinion in neurobiology 20:68-78.
van Dellen E, Douw L, Baayen JC, Heimans JJ, Ponten SC, Vandertop WP, Velis DN, Stam CJ, Reijneveld JC (2009) Long-term effects of temporal lobe epilepsy on local neural networks: a graph theoretical analysis of corticography recordings. PloS one 4:e8081.
van Wieringen J-P, Booij J, Shalgunov V, Elsinga P, Michel MC (2013) Agonist high-and low-affinity states of dopamine D2 receptors: methods of detection and clinical implications. Naunyn-Schmiedeberg's archives of pharmacology 386:135-154.
Vidal B, Sebti J, Verdurand M, Fieux S, Billard T, Streichenberger N, Troakes C, Newman-Tancredi A, Zimmer L (2016) Agonist and antagonist bind differently to 5-HT 1A receptors during Alzheimer's disease: A post-mortem study with PET radiopharmaceuticals. Neuropharmacology 109:88-95.
Vlooswijk MC, Vaessen MJ, Jansen JF, de Krom MC, Majoie HJ, Hofman PA, Aldenkamp AP, Backes WH (2011) Loss of network efficiency associated with cognitive decline in chronic epilepsy. Neurology 77:938-944.
Wang DD, Deans AE, Barkovich AJ, Tihan T, Barbaro NM, Garcia PA, Chang EF (2013) Transmantle sign in focal cortical dysplasia: a unique radiological entity with excellent prognosis for seizure control. Journal of neurosurgery 118:337-344.
Wang H, Jin X, Zhang Y, Wang J (2016) Single-subject morphological brain networks: connectivity mapping, topological characterization and test-retest reliability. Brain and behavior 6:e00448.
Watrin F, Manent JB, Cardoso C, Represa A (2015) Causes and consequences of gray matter heterotopia. CNS neuroscience and therapeutics 21:112-122.
Watts DJ, Strogatz SH (1998) Collective dynamics of 'small-world' networks. Nature 393:440-442.
Waung MW, Huber KM (2009) Protein translation in synaptic plasticity: mGluR-LTD, Fragile X. Current opinion in neurobiology 19:319-326.
White R, Hua Y, Scheithauer B, Lynch DR, Henske EP, Crino PB (2001) Selective alterations in glutamate and GABA receptor subunit mRNA expression in dysplastic neurons and giant cells of cortical tubers. Annals of neurology 49:67-78.
Widjaja E, Blaser S, Miller E, Kassner A, Shannon P, Chuang SH, Snead OC, 3rd, Raybaud CR (2007) Evaluation of subcortical white matter and deep white matter tracts in malformations of cortical development. Epilepsia 48:1460-1469.
Wyss MT, Ametamey SM, Treyer V, Bettio A, Blagoev M, Kessler LJ, Burger C, Weber B, Schmidt M, Gasparini F, Buck A (2007) Quantitative evaluation of 11C-ABP688 as PET ligand for the measurement of the metabotropic glutamate receptor subtype 5 using autoradiographic studies and a beta-scintillator. NeuroImage 35:1086-1092.
Ying Z, Gonzalez-Martinez J, Tilelli C, Bingaman W, Najm I (2005) Expression of neural stem cell surface marker CD133 in balloon cells of human focal cortical dysplasia. Epilepsia 46:1716-1723.
Zhang K, Sejnowski TJ (2000) A universal scaling law between gray matter and white matter of Cerebral cortex. Proceedings of the national academy of sciences of the United States of America 97:5621-5626.

Zimmer ER, Parent MJ, Cuello AC, Gauthier S, Rosa-Neto P (2014) MicroPET imaging and transgenic models: a blueprint for Alzheimer's disease clinical research. Trends in neurosciences.
Zimmer ER, Parent MJ, Leuzy A, Aliaga A, Aliaga A, Moquin L, Schirrmacher ES, Soucy J-P, Skelin I, Gratton A (2015a) Imaging in vivo glutamate fluctuations with [11C] ABP688: a GLT-1 challenge with ceftriaxone. Journal of cerebral blood flow and metabolism 35:1169-1174.
Zimmer ER, Parent MJ, Leuzy A, Aliaga A, Aliaga A, Moquin L, Schirrmacher ES, Soucy JP, Skelin I, Gratton A, Gauthier S, Rosa-Neto P (2015b) Imaging in vivo glutamate fluctuations with [(11)C]ABP688: a GLT-1 challenge with ceftriaxone. Journal of cerebral blood flow and metabolism 35:1169-1174.